UNIVERSITI TEKNOLOGI MARA

COMPACT ON-METAL UHF RFID TAG ANTENNAS USING EMBEDDED INDUCTANCE AND HUYGENS' META-ELEMENT TECHNIQUES

NURFARAHIN BINTI MISWADI

PhD

August 2026

UNIVERSITI TEKNOLOGI MARA

COMPACT ON-METAL UHF RFID TAG ANTENNAS USING EMBEDDED INDUCTANCE AND HUYGENS' META-ELEMENT TECHNIQUES

NURFARAHINN BINTI MISWADI

Thesis submitted in fulfilment
of the requirements for the degree of
Doctor of Philosophy
(Electrical Engineering)

Faculty of Electrical Engineering

August 2026

CONFIRMATION BY PANEL OF EXAMINERS

I certify that a Panel of Examiners has met on 27th February 2026 to conduct the final examination of Nurfarahin Binti Miswadi on her Doctor of Philosophy thesis entitled "Compact On-Metal UHF RFID Tag Antennas Using Embedded Inductance and Huygens' Meta-Element Techniques" in accordance with Universiti Teknologi MARA Act 1976 (Akta 173). The Panel of Examiners recommends that the student be awarded the relevant degree. The Panel of Examiners was as follows:

Zuhaina Zakaria, PhD
Professor
Faculty of Electrical Engineering
Universiti Teknologi MARA
(Chairman)

Aziati Husna Awang, PhD
Senior Lecturer
Faculty of Electrical Engineering
Universiti Teknologi MARA
(Internal Examiner)

Muzammil Jusoh, PhD
Professor
Faculty of Electronic Engineering
Technology
Universiti Malaysia Perlis
(External Examiner)

PROF DR HJH ZURAEDA IBRAHIM
Dean
Institute of Postgraduate Studies
Universiti Teknologi MARA

Date: 17 August 2026

AUTHOR'S DECLARATION

I declare that the work in this thesis was carried out in accordance with the regulations of Universiti Teknologi MARA. It is original and is the results of my own work, unless otherwise indicated or acknowledged as referenced work. This thesis has not been submitted to any other academic institution or non-academic institution for any degree or qualification.

I, hereby, acknowledge that I have been supplied with the Academic Rules and Regulations for Postgraduate, Universiti Teknologi MARA, regulating the conduct of my study and research.

Name of Student	:	Nurfarahin binti Miswadi
Student ID. No.	:	2021321075
Programme	:	Doctor of Philosophy (Electrical Engineering) – EE950
Faculty	:	Electrical Engineering
Thesis Title	:	Compact On-Metal UHF RFID Tag Antennas Using Embedded Inductance and Huygens' Meta-Element Techniques
Signature of Student	:	……..
Date	:	August 2026

ABSTRACT

This thesis presents the design, development, and experimental validation of two high-performance ultra-high-frequency (UHF) passive radio-frequency identification (RFID) tag antennas specifically engineered for reliable operation in metallic environments. In such environments, conventional RFID tags typically suffer from severe impedance detuning, degraded radiation efficiency, unstable resonance, and limited read range due to strong electromagnetic coupling with conductive surfaces. To address these challenges, two complementary antenna architectures are proposed to achieve enhanced frequency stability, controllable impedance characteristics, and improved radiation performance within compact form factors suitable for industrial deployment. The first contribution presents a compact folded stacked-patch UHF RFID tag antenna incorporating embedded inclined inductive slots for on-metal applications. The folded configuration effectively minimizes the physical footprint while extending the surface current path to achieve resonance across the 860–960 MHz UHF band. The inclined slots act as embedded inductive elements, providing precise reactance control and enabling direct conjugate matching to complex RFID microchip impedances without the need for external lumped components. A comprehensive electromagnetic analysis of the embedded inductive mechanism was conducted through full-wave simulations and surface current distribution investigations. Fabricated prototype measurements show excellent agreement with the simulated results, validating the accuracy of the design methodology and electromagnetic modelling. The proposed tag achieves a measured read range of 16 m at its 918 MHz resonant frequency under 4 W EIRP, thereby confirming the effectiveness of the embedded inclined inductive tuning mechanism in enhancing impedance matching and overall tag performance in metallic environments. The second contribution introduces a folding-free dipolar patch RFID tag antenna integrated with a Huygens' Meta-Element (HME) for gain enhancement under metallic mounting conditions. The HME is strategically positioned above the dipolar radiator to promote constructive coupling between electric and magnetic dipole responses, thereby enhancing forward radiation. Surface current analysis confirms the excitation of antiparallel current loops, validating the presence of Huygens' resonance behaviour. Experimental validation demonstrates improved realized gain, extended read range, and enhanced resistance to metallic detuning compared to conventional dipolar RFID tag configurations. A realized gain enhancement of approximately 3 dBi was achieved with the HME-integrated dipolar configuration compared to the standalone dipolar tag, along with a measured read range of 8.23 m. These results confirm the effectiveness and feasibility of HME integration for passive UHF RFID tag performance enhancement. Collectively, the proposed antenna designs establish a comprehensive and fabrication-friendly for compact, high-efficiency on-metal UHF RFID tag antennas. The integration of embedded inductive slot and Huygens'-based metasurface enhancement provides practical and scalable solutions for robust asset tracking in logistics, manufacturing, and industrial environments. The findings of this research contribute new theoretical and experimental insights into the electromagnetic mechanisms governing platform-tolerant RFID performance and advance the development of next-generation passive RFID systems with improved robustness, efficiency, and deployment flexibility

ACKNOWLEDGEMENT

In the name of Allah, the Most Gracious and the Most Merciful.

First and foremost, I would like to express my deepest gratitude to my main supervisor, Prof. Madya Ir. Dr. Nurul Huda binti Abd Rahman, for her invaluable guidance, continuous encouragement, constructive criticism, and unwavering support throughout the completion of this research. Her expertise, patience, and dedication have greatly shaped the direction and quality of this work. I am truly grateful for her mentorship, which has strengthened both my technical knowledge and research maturity.

My sincere appreciation is also extended to my co-supervisors, Ir. Dr. Suhaila binti Subahir, Ts. Dr. Mohd Aziz bin Aris, and Prof. Ts. Dr. Lim Eng Hock, for their insightful comments, technical advice, and continuous support. Their valuable suggestions and professional guidance have significantly contributed to the successful completion of this study.

I would also like to acknowledge my colleagues and the technical staff at the Antenna Research Centre (ARC), Universiti Teknologi MARA, for their assistance, discussions, and support, particularly during the simulation, fabrication, and measurement phases of this research. Their cooperation and technical expertise were instrumental in ensuring the smooth execution of experimental validations.

My heartfelt gratitude goes to my beloved husband, Muhammad Shamil bin Azni, for his endless patience, understanding, prayers, and unwavering emotional support throughout this challenging journey. His encouragement has been my constant source of strength and motivation.

Finally, this thesis is lovingly dedicated to my parents, Miswadi bin Nadimon and whose sacrifices, prayers, and unconditional love have shaped who I am today. I am forever indebted to them for their continuous support and belief in my dreams. I also extend my appreciation to my parents-in-law and all my siblings for their encouragement and prayers throughout my doctoral journey.

May Allah reward all of you for your kindness and support.

TABLE OF CONTENTS

		Page
CONFIRMATION BY PANEL OF EXAMINERS		**ii**
AUTHOR'S DECLARATION		**iii**
ABSTRACT		**iv**
ACKNOWLEDGEMENT		**v**
TABLE OF CONTENTS		**vi**
LIST OF TABLES		**ix**
LIST OF FIGURES		**x**
LIST OF SYMBOLS		**xvii**
LIST OF ABBREVIATIONS		**xix**
CHAPTER 1 INTRODUCTION		**1**
1.1	Research Background	1
1.2	Problem Statement	2
1.3	Research Objectives	5
1.4	Scope of Research	5
1.5	Thesis Outline	6
CHAPTER 2 LITERATURE REVIEW		**8**
2.1	Introduction	8
2.2	RFID Technology and Applications	9
	2.2.1 RFID System Components	9
	2.2.2 RFID Operating Frequency	10
	2.2.3 RFID Applications	12
2.3	Previous Work on RFID Tag Antennas	14
	2.3.1 Review of UHF RFID Tag Antenna Designs	14
	2.3.2 UHF RFID Tag Antenna Designs for Metallic Environment	25
	2.3.3 Metasurface-Based Concepts in UHF RFID Tag Antenna Designs	32
2.4	Summary	38

CHAPTER 3 RESEARCH METHODOLOGY **46**

3.1 Introduction 46
3.2 Research Methodology 47
3.3 RFID Antenna Design Requirements and Key Technical Parameters 50
3.3.1 RFID Design Specification 50
3.3.2 Read range 52
3.3.3 Power Transfer Coefficient (τ) 53
3.4 RFID Tag Antenna Design 54
3.4.1 Dipolar Patch Antenna 54
3.4.2 RFID Microchip 57
3.4.3 Huygens' Metasurface 58
3.5 Simulation of RFID Tag Antenna with Integrated Microchip 62
3.6 Fabrication of RFID Tag Antenna 65
3.7 Measurement of RFID Tag Antenna Technical Parameters using Voyantic Tagformance Pro System 67
3.8 Summary 69

CHAPTER 4 EMBEDDED - INDUCTANCE FOLDED STACKED PATCH TAG ANTENNA WITH INCLINED SLOTS **71**

4.1 Introduction 71
4.2 Preliminary Design of Folded Stacked Patch On-Metal Tag Antenna 71
4.3 Folded Stacked Patch Antenna with Inclined Slot 75
4.3.1 Simulation Model of a Double-Layered Folded-Patch Tag Antenna with Slots 75
4.3.2 Parametric Analysis and Design Evolution of Double-Layer Folded Patch Tag Antenna with Embedded Inductance 77
4.3.3 Slot and Stub Parameter Optimization 80
4.3.4 Embedded Inductance: Working Principles of the Inclined Slot Structure 85
4.4 Experimental Validation and Performance Analysis 88
4.5 Summary 98

CHAPTER 5 DEVELOPMENT OF AN ANTI-METAL DIPOLAR TAG ANTENNA INCORPORATING A HUYGENS' META ELEMENT FOR GAIN ENHANCEMENT 100

5.1 Introduction 100

5.2 Design and Analysis of Broadband Huygens' Meta Element 101

5.2.1 Configuration of the unit cell 101

5.2.2 Reflection (Magnitude) and Transmission (Magnitude and Phase) Characteristics of the Huygens' Meta Element (HME) 103

5.2.3 Electric Admittance and Magnetic Impedance Analysis of the Huygens' Meta Element (HME) 105

5.2.4 Surface Current Distribution and Behaviour Analysis of the Huygens' Meta Element (HME) 106

5.3 Simulation and Analysis Integration of Huygens' Meta-Element (HME) with the Dipolar Patch 108

5.3.1 Antenna configuration of the HME-Integrated Dipolar Patch 109

5.3.2 HME-Integrated Dipolar Patch RFID: Working Principles and Result Analysis 110

5.4 Experimental Validation and Performance Measurement 115

5.5 Summary 122

CHAPTER 6 CONCLUSION 124

6.1 Conclusion 124

6.1.1 Folded Stacked-Patch Tag with Embedded Inductive Slots 124

6.1.2 Integration of Huygens Meta-Elements for Gain Enhancement 125

6.2 Overall Research Contributions 126

6.3 Recommendations for Future Work 127

6.4 Summary 129

REFERENCES 130

APPENDICES 139

AUTHOR'S PROFILE 142

LIST OF TABLES

Tables	Title	Page
Table 2.1	Summary Of Reported On-Metal UHF RFID Tag Antenna Designs Highlighting the Research Gaps.	40
Table 3.1	Design Specifications for Folded RFID Tag Antenna with Embedded Inductance.	51
Table 3.2	Design Specifications for Dipolar Patch Tag with Huygens' Meta Element.	51
Table 3.3	Calculated Dimension of the Dipolar Patch Antenna.	56
Table 3.4	Comparison of NXP UCODE 8 and UCODE 9 RFID Microchips.	58
Table 4.1	Comparison of Single and Double-Layered Tag Antenna.	73
Table 4.2	Optimum Design Parameters of The Tag Antenna.	77
Table 4.3	Comparison Of the Key Performance Parameters of the RFID Tag Antenna Across the Three Stages of Structural Evolution.	78
Table 4.4	Comparative Analysis of On-Metal Patch-Type Tag Antennas and the Tag Presented in this Study.	98
Table 5.1	Optimized Design Parameters of the HME-Integrated Dipolar Patch RFID Tag.	110

LIST OF FIGURES

Figures	Title	Page
Figure 1.1	Automatic Identification Technologies (Auto-ID). (Wyld, 2010)	1
Figure 2.1	Basic Components of an RFID System.(Hussain et al., 2020)	10
Figure 2.2	UHF-RFID Frequency Allocation Throughout the World(Toaha et al., 2011)	12
Figure 2.3	RFID Technology Applications Across Various Sectors. (N. F. Miswadi et al., 2022)	12
Figure 2.4	Integration of IoT ecosystem in RFID.(Lubna et al., 2022)	14
Figure 2.5	Top View of the Tag Antenna Configuration With (a) Single T-Matching And (b) Double T-Matching.(Choudhary et al., 2018)	16
Figure 2.6	T-Match Equivalent Circuit.(A. A. Sharatol Ahmad Shah et al., 2018)	16
Figure 2.7	Proposed Modified T-Matched RFID Tag Antenna Design Incorporating a Parallel Bridge and Folded Dipole Arms.(Wickramasinghe et al., 2021)	17
Figure 2.8	Configuration of Inductively Coupled Feed and Its Equivalent Circuit. (Turitsyna & Webb, 2005)	18
Figure 2.9	Proposed Dual-Band RFID Tag Antenna Configuration and Its Inductively Coupled Spiral Loop Feed Network(Bansal et al., 2022)	19
Figure 2.10	Proposed Geometry of Inverted-F Antenna (IFA) With Shorting Stub. (Tan et al., 2020)	20
Figure 2.11	(a)Configuration (b) Realized gain and Read Range of Compact UHF RFID Tag Antenna. (Bhaskar & Singh, 2021)	21

Figure 2.12 A Meander-Line UHF RFID Tag Antenna Incorporating a Semi-Circular Loop. (P. Wongsiritorn et al., 2009) 22

Figure 2.13 A Flexible UHF RFID Zigzag Dipole Tag Antenna.(Farnana et al., 2024) 23

Figure 2.14 (a) Capacitive Tip-Loaded Dipole Antenna with A T-Match Network. (b) Maximum Read Range of the Tag Antenna (Shreya U. Naik et al., 2020) 24

Figure 2.15 Geometry of the Short-Ended Patch Tag Antenna Mounted on an FR4 Substrate.(López-Soriano & Parrón, 2015) 26

Figure 2.16 (a)Tag Prototype Mounting on the Copper Plate (b) Maximum Read Range in US band.(Mo & Li, 2019) 27

Figure 2.17 Fabricated Offset-Fed Folded Dipole Antenna with an Open End.(Sun et al., 2017) 28

Figure 2.18 (a) Proposed Folded RFID Tag Antenna with Chip (b) Maximum Tag Sensitivity at 924 MHz. (F.-L. Bong et al., 2018) 29

Figure 2.19 (a)Tag Antenna Configuration with Narrow Meandered Slot (b) Realized Gain and Frequency Response.(F. L. Bong et al., 2017) 31

Figure 2.20 Three-Dimensional (3D) Configuration of the Proposed Tag Antenna and its Corresponding Structural View. (Thirappa et al., 2019) 32

Figure 2.21 (a) Top and Side View of the Unit Cell (b) Electric Field Distribution with and without the Huygens' Lens.(Akram et al., 2020) 33

Figure 2.22 Design of the Proposed Square Unit Cell with its Geometric Parameters.(Peng et al., 2020) 34

Figure 2.23 Top View, Bottom View, And Three-Dimensional (3D) Configuration of the Proposed Unit Cell.(Xue et al., 2020) 35

Figure 2.24	(a) Configuration of The AMC Substrate Layer. (b) Fabricated RFID Tag Antenna Integrated with The AMC Layer at The Bottom.(Kim et al., 2009)	36
Figure 2.25	Fabricated Nested Slot Tag Antenna Mounted on Jigsaw-Shaped Metasurface.(Q. Liu et al., 2022)	37
Figure 3.1	Flowchart of the Research Methodology.	49
Figure 3.2	Basic Dipole Antenna.	55
Figure 3.3	Configuration of The Dipolar Patch.	55
Figure 3.4	(a) Illustration of Huygens' Principle And (b) Its Interpretation in The Antenna Aperture Analogy.	59
Figure 3.5	Side-View Configuration of The Proposed Huygens' Surface.	60
Figure 3.6	Simulation Setup Of The RFID Tag Antenna With Microchip In CST: (a) 3D Antenna Model With Chip Placement, (b) Discrete Port Across The Feed Gap, (c) Schematic Port Connection, (d) Chip Impedance Setting, And (e) Final Solver Execution.	65
Figure 3.7	RFID Antenna Prototype Fabrication Using Chemical Etching Technique.	67
Figure 3.8	Experimental Validation Setup: (A) Actual Measurement Configuration for The RFID Tag Antenna, and (B) Schematic Diagram of The Voyantic Tagformance Pro Measurement System Used for Tag Performance Characterization.	69
Figure 4.1	The Single-Layered Tag Antenna Configuration.	72
Figure 4.2	(a)Tag Prototype Mounting on the Copper Plate (b) Maximum Read Range in US band.(Mo & Li, 2019)	73
Figure 4.3	(a) Power Transmission Coefficient, τ (b) Antenna Impedance of The Single-Layered and Double-Layered Tag Antenna	74

Figure 4.4 The Double-Layered Tag Antenna Configuration: (a) Top and Corresponding Views of Patch A, (b) Top View of Patch B, And (c) Ground Plane. 77

Figure 4.5 Design Evolution Of The Double-Layer Folded Patch Tag Antenna, Showing (a) The Single-Layered Patch Configuration, (b) The Formation Of The Double-Layer Patch Structure, And (c) The Final Configuration Incorporating Inclined Slots. 78

Figure 4.6 (a) Antenna Input Impedance and (b) Power Transmission Coefficient (T) for The Three Design Stages: The Single-Layered Patch Configuration, The Double-Layer Patch Configuration, And The Final Structure With Inclined Slots On Both Patches. 80

Figure 4.7 Simulated (a) Power Transmission Coefficient, (b) Antenna Impedance and Its (c) Realized Gain And 3dB Beamwidth by Varying the Stub Width, a. 82

Figure 4.8 Simulated (a) Power Transmission Coefficient And (b) Antenna Impedance by Varying Slot Length ,b_1. 83

Figure 4.9 Simulated (a) Power Transmission Coefficient And (b) Antenna Impedance by Varying Slot Width, c 84

Figure 4.10 Simulated Antenna Reactance and Operating Frequency by Varying (a) b_1, (b) b_2, (c) b_3. 86

Figure 4.11 Simulated Field And Current Characteristics Of The Tag Antenna: (a) Surface Current Distribution On Patch A; (b) Surface Current Distribution On Patch B; (c) Magnetic Field (H-Field) Magnitude Along The x-axis At $y = 2$ mm And $y = 30$ mm; (d) Positions Corresponding To The Peak H-Field Magnitudes. 88

Figure 4.12 (a) Naked Inlay (b) Step 1 (c) Step 2 (d) Step 3 of the Tag Prototype Folding Process (e) Top and Perspective View of The Fabricated Tag. 90

Figure 4.13	(a) Tag Prototype Mounted on A Centre 200 mm × 200 mm Metal Plate (b) Measurement Setup in The Voyantic Anechoic Chamber.	92
Figure 4.14	Comparison Simulated and Measured Realised Gain of The Fabricated Tag Along with The Measured Tag Sensitivity.	93
Figure 4.15	Measured Read Distances in the (a) *xy*-plane (b) *xz*- and *yz*-planes At the Frequency Of 918 MHz	93
Figure 4.16	Simulated and Measured Realized Gain in the (a) *yz*-plane and (b) *xz*-planes At the Frequency Of 918 Mhz.	94
Figure 4.17	Measurement of Read Distances at Various (a) L_p and (b) W_p.	95
Figure 4.18	Placement of The Tag on Various Household Items: (a) Base And (b) Body.	96
Figure 4.19	Measurement of Read Distances on Various Metallic Household Products.	97
Figure 5.1	Huygens' Unit Cell Configuration Showing (a) The Top View And (b) The Bottom View, and (c) The Simulated Model Used for Electromagnetic Analysis.	103
Figure 5.2	Simulated $S_{11}$and S_{21} Magnitude Responses of The Unit Cell with Only the Top and Only the Bottom HME Layers.	104
Figure 5.3	Magnitude Curve of S_{11} for the HME with Both Top and Bottom Layers.	104
Figure 5.4	Magnitude and Phase Curves of S_{21} for the HME With Both Top and Bottom Layers.	105
Figure 5.5	Normalized Electric Admittance, $Yes\eta$ And Magnetic Impedance, Zms /η of the HME unit Cell: (a) Real Components And (b) Imaginary Components.	106

Figure 5.6 Surface Current Distribution Of The Huygens' Unit Cell On The Top And The Bottom Layers in One Period T at 868 MHz (a) t = 0 (b) t = T/4 (c) t = T/2 (d) t = 3T/4. 108

Figure 5.7 (a) Triangular Dipolar Patch Radiator with Top and Side Views; (b) Ground Plane of Dipolar Patch. 110

Figure 5.8 Comparison of Power Transmission Coefficients Between the Dipolar Tag and the Dipolar Tag Integrated With HME. 111

Figure 5.9 Comparison of Antenna Impedances Between the Dipolar Tag and The Dipolar Tag Integrated With HME. 112

Figure 5.10 Simulated Realized Gain Patterns in the (a) *yz*-plane and (b) *xz*-plane 113

Figure 5.11 Simulated H-Field Distribution at 868 MHz: (a) Conventional Dipolar Tag and (b) HME-Integrated Dipolar Tag. 114

Figure 5.12 H-Field Analysis of the HME-Integrated Dipolar Tag Showing(a) Side-View Distribution And (b) H-Field Magnitude Along the *x*-axis At z = 2.4 mm. 115

Figure 5.13 Fabricated Antenna Components and Assembly: (a) Dipolar Patch Layer with Shorting Stubs; (b) Huygens' Meta Element (HME); And (c) Fabricated Layers Prior To Stacking (Left) And the Fully Assembled Tag with PP4 Foam (Right). 116

Figure 5.14 (a) Measurement Setup Within the Anechoic Chamber. (b) Proposed HME RFID Tag Positioned at The Centre of A 200 mm × 200 mm Metal Plate. 118

Figure 5.15 Simulated and Measured Realized Gain Alongside Tag Sensitivity Measurements. 118

Figure 5.16 Read Pattern Measurements Conducted At 868 MHz in The (a) *xy*-plane, and (b) *xz*- and *yz*-planes. 119

Figure 5.17 Measured Read Range at Different Values of (a) L_p and (b) W_p across the 840–890 MHz Frequency Range. 120

Figure 5.18 Tag Positioning on Various Household Items: (a) Base And (b) Side Body Surfaces. 122

Figure 5.19 Measured Read Range on The Base and Side Surfaces of Various Household Items. 122

LIST OF SYMBOLS

Symbols

η	Intrinsic Impedance of Free Space
Ω	Ohm
τ	Power Transfer Coefficient
λ	Wavelength Of the Operating Frequency
ε_r	Dielectric Constant
Z_{in}	Input Impedance
W	Watt
tan δ	Tangent Loss
S_{11}	Reflection Coefficient
Q	Quality Factor
mm	Millimetre
MHz	Megahertz
M	Mutual Inductance
m	Meter
H	Magnetic Field
E	Electric Field
dBm	Decibel Milliwatts
dB	Decibel
dBi	Decibel Isotropic
ΔL	Length Extension

μ_o	Permeability In Free Space
ε_o	Permittivity In Free Space
ε_{reff}	Effective Dielectric Constant
Z_c	Chip Impedance
Z_a	Antenna Impedance
X_c	Reactance Part of The Chip
X_a	Reactance Part of The Antenna
S_{21}	Transmission Coefficient
R_{max}	Read Range
R_c	Resistive Part of The Chip
R_a	Resistive Part of The Antenna
P_{tag}	Tag's Sensitivity
P_t	Transmit Power of The Reader
P_r	Threshold Power
P_i	Chip's Sensitivity
P_{EIRP}	Equivalent Isotropically Radiated Power
L_{cable}	Cable Loss
L_{fwd}	Forward Path Loss
G_{tag}	Gain Of the Tag Antenna
G_t	Gain Of the Reader Antenna
Z_{ms}	Magnetic Surface Impedance
Y_{es}	Electric Surface Admittance

LIST OF ABBREVIATIONS

Abbreviations

Auto-ID	Auto Identification
AMC	Artificial Magnetic Surface
CST	Computer Simulation Technology
EBG	Electronic Band Gap
EIRP	Equivalent Isotropically Radiated Power
FCC	Federal Communications Commission
FEM	Finite Element Method
FSPL	Free Space Path Loss
HF	High Frequency
HME	Huygens' Meta Element
IEEE	Institute Of Electrical and Electronics Engineers
IFA	Inverted F Antenna
IoT	Internet Over Thing
LEU	Lower EUROPE
LF	Low Frequency
LP	Linearly Polarized
MCMC	Malaysian Communications and Multimedia Commission
PCB	Printed Circuit Board
PIFA	Planar Inverted F Antenna

RFID	Radio Frequency Identification
SRR	Split Ring Resonator
TUT	Tag Under Test
UHF	Ultra-High Frequency

CHAPTER 1
INTRODUCTION

1.1 Research Background

The rapid advancement of wireless communication technologies has significantly transformed modern industrial and commercial systems, particularly through the development of Automatic Identification (Auto-ID) technologies. As illustrated in Figure 1.1, Auto-ID covers a broad spectrum of identification techniques, including barcode systems, biometric systems, smart cards, optical character recognition (OCR), and radio frequency identification (RFID), which can be further classified into active and passive systems(Wyld, 2010) . These technologies enable automated data capture and are extensively implemented in logistics, inventory management, healthcare monitoring, transportation networks, and smart manufacturing to enhance operational efficiency, accuracy, and traceability.

Among these technologies, RFID has emerged as a highly efficient solution due to its capability for non-line-of-sight communication, simultaneous multi-tag detection, and real-time data acquisition. Unlike conventional barcode systems that require direct line-of-sight scanning and single-item reading, RFID systems operate through electromagnetic coupling between a reader and a tag, enabling wireless object identification without physical contact. These advantages position RFID as a key enabling technology for large-scale, automated tracking and identification systems.

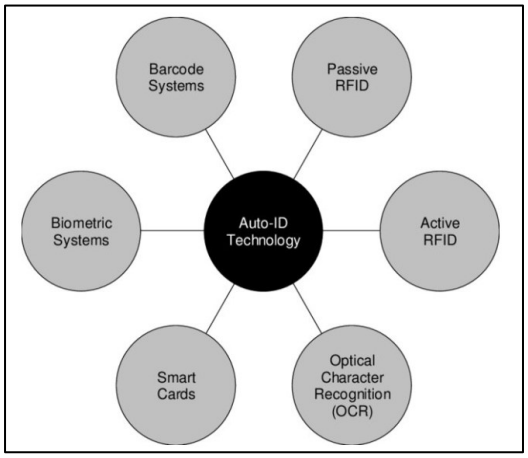


Figure 1.1 Automatic Identification Technologies (Auto-ID). (Wyld, 2010)

Within RFID technology, Ultra-High Frequency (UHF) passive systems are widely adopted because of their extended reading range, higher data transmission rates, and cost-effective implementation. Passive RFID tags operate without an internal power source and instead harvest energy from the electromagnetic field transmitted by the reader. This feature allows compact and low-cost tag structures suitable for large-scale deployment. However, the performance of passive RFID systems is fundamentally governed by the design of the tag antenna, which directly influences impedance matching, radiation characteristics, and overall power transfer efficiency.

To achieve higher gain and extended read distance, increasing the physical size of the antenna is often necessary. Nevertheless, bulky tag structures are impractical in many real-world applications where space is constrained or where tags must conform to compact or irregular surfaces. This trade-off between antenna performance and size limitation has motivated continuous research in compact and high-efficiency RFID antenna design.

In addition to size constraints, further considerations arise when RFID tags are employed on metallic surfaces. In numerous industrial applications, tags are attached to metallic assets such as containers, machinery components, and structural equipment. These mounting conditions require antenna configurations capable of maintaining stable electromagnetic performance in close proximity to conductive surfaces. Consequently, recent research has focused on developing antenna structures that integrate compact geometry with reliable operation for metal-mounted environments.

Within this context, this research investigates the development of a compact UHF passive RFID tag antenna specifically designed for on-metal applications. A folded patch configuration incorporating embedded inductive slots is proposed to achieve structural miniaturization while providing controlled impedance characteristics. In addition, a Huygens Meta-Element (HME) is integrated to enhance radiation directivity and gain performance. The proposed designs are systematically evaluated through parametric analysis, full-wave electromagnetic simulations, and experimental measurements to assess their suitability for deployment in metallic environments.

1.2 Problem Statement

The deployment of passive UHF RFID systems in industrial asset tracking, warehouse automation, and smart manufacturing environments frequently involves metallic platforms such as containers, machinery, pipelines, and structural components.

However, reliable operation of RFID tag antennas in metallic environments remains a significant technical challenge. The main problems addressed in this study are outlined as follows.

a) Conventional RFID tag antennas are not suitable for operation in metallic environments due to severe electromagnetic coupling effects.

When placed in close proximity to metallic surfaces, conventional RFID tag antennas experience strong electromagnetic coupling caused by image current formation. This interaction alters the surface current distribution, resulting in resonant frequency shifts and deviations in input impedance. Consequently, the antenna fails to maintain proper conjugate matching with the RFID chip, leading to reduced radiation efficiency and degraded read range. These performance deteriorations limit the reliability and practical deployment of passive UHF RFID tags directly mounted on metal objects.

b) Miniaturization of on-metal RFID tag antennas introduces efficiency and impedance-matching trade-offs.

Industrial applications demand compact, low-profile, and cost-effective RFID tags that can be readily mounted on small, curved, or irregular metallic surfaces. However, antenna miniaturization inherently introduces performance trade-offs. As the antenna's physical dimensions are reduced, radiation efficiency typically decreases and causes impedance mismatch between the antenna and the RFID chip. This mismatch restricts effective power transfer between the tag and microchip and consequently degrades the achievable read range. Therefore, there is a critical need to develop a miniaturized on-metal RFID tag antenna that preserves stable impedance matching and acceptable radiation characteristics without increasing structural complexity or profile thickness.

c) Existing on-metal RFID tag designs lack flexible tuning mechanisms for impedance stabilization.

Passive RFID tag operation relies on maximum power transfer between the antenna and the microchip, which requires precise conjugate impedance matching. In metallic environments, even slight variations in mounting conditions can significantly alter the antenna's reactance and resonant frequency. However, many reported on-metal RFID tag antenna designs do not incorporate effective tuning mechanisms to compensate for these variations. The absence of controllable resonance adjustment limits design adaptability and reduces operational consistency across different metallic platforms. Therefore, a tunable antenna configuration capable of regulating the resonant frequency and input reactance is essential to ensure stable and reliable operation.

d) Radiation performance enhancement techniques for compact on-metal RFID tags remain insufficiently explored.

While accurate impedance matching is essential to ensure chip activation, radiation performance and read range enhancement are equally critical for reliable tag operation. Compact on-metal RFID tags often exhibit low gain due to backward radiation and electromagnetic energy absorption by the underlying metallic surface. Although metasurface- and metamaterial-based structures have demonstrated their capability to manipulate electromagnetic wave propagation, their systematic integration into passive UHF RFID tag antennas for metallic applications remains limited. In particular, the potential of Huygens' Meta Elements (HME), which simultaneously tailor electric and magnetic responses to enhance forward radiation and suppress backward scattering, has not been comprehensively investigated in the context of on-metal RFID tags.

Furthermore, rigorous experimental validation under controlled laboratory conditions is necessary to verify theoretical analysis and full-wave simulation results. Addressing these gaps forms the foundation of this research, which aims to develop a compact, tunable, and gain-enhanced passive UHF RFID tag antenna suitable for reliable operation in metallic environments. The first design focuses on achieving a compact and tunable folded stacked-patch antenna through embedded inductive slot loading to improve impedance matching and frequency stability. Building upon the findings of the first design, the second design integrates a Huygens' Meta Element (HME) with a dipolar patch antenna to enhance gain and radiation performance while maintaining a compact profile. Both antenna designs are experimentally validated to

demonstrate their effectiveness in providing reliable long-range RFID performance in metallic environments.

1.3 Research Objectives

This research is conducted to address the challenges identified in the problem statement (Section 1.2). The thesis presents a comprehensive theoretical and experimental investigation of passive Ultra-High-Frequency (UHF) Radio-Frequency Identification (RFID) tag antennas designed for operation in metallic environments. The specific objectives of this research are as follows:

a) To develop a miniaturized UHF RFID tag antenna incorporating a folded configuration with an optimum read range performance.

b) To integrate and propose a tuning element that enables controlled adjustment of the RFID tag antenna resonant frequency and input reactance when mounted on metallic surfaces.

c) To systematically analyze the impact of Huygens' Meta Element (HME) on the radiation characteristics of the on-metal RFID tag antenna.

d) To experimentally validate the performance UHF RFID tag prototype design through laboratory measurements.

1.4 Scope of Research

The increasing adoption of Radio Frequency Identification (RFID) systems in logistics, asset tracking, industrial automation, and smart manufacturing has intensified the demand for reliable and high-performance tag antenna designs. Among the available RFID frequency allocations, the Ultra-High Frequency (UHF) band is widely preferred due to its longer read range and higher data transmission capability, making it suitable for medium-to-long distance identification applications. Accordingly, the primary scope of this research is the design and optimization of a passive UHF RFID tag antenna operating within the regulated UHF frequency spectrum of 860 – 960 MHz.

The operating frequency of the proposed antenna design complies with regulations established by the International Telecommunication Union (ITU) and relevant national spectrum authorities(Radiocommunication Sector of ITU, 2012). To ensure compatibility with international RFID applications, the antennas are designed to

operate within the internationally recognized UHF RFID bands, namely 902–928 MHz (US band) and 865–868 MHz (European band).

The antenna design and performance evaluation are conducted using Computer Simulation Technology (CST) Microwave Studio. The key performance parameters investigate in this research include input impedance, power transmission coefficient (τ), realized gain, radiation pattern, radiation efficiency, and achievable read range. In addition, the effects of antenna miniaturization, impedance matching, frequency stability, and gain enhancement are systematically evaluated to assess the effectiveness of the proposed antenna designs. The RFID microchip employed in this research are the NXP UCODE 8 and NXP UCODE 9. These chips are selected due to their high sensitivity, which directly influences the achievable read range. Read-range evaluation assumes a maximum Effective Isotropic Radiated Power (EIRP) of 4 W, in accordance with regulatory limits specified by the Malaysian Communications and Multimedia Commission (MCMC) (MCMC, 2020).

This research specifically addresses on-metal RFID applications, where conductive surfaces significantly affect antenna impedance, causing frequency detuning and degradation of radiation performance. Accordingly, the proposed tag antennas are designed and optimized for reliable operation on metallic objects. During the simulation stage, the proposed tag antenna is mounted on a metallic plate with dimensions of 200 mm × 200 mm to emulate a metallic deployment scenario. Similarly, during experimental measurements, the fabricated tag antenna is positioned at the centre of an identically sized metallic plate to ensure consistency with the simulation setup and to validate the accuracy of the simulated results.

The scope of this research is limited to passive UHF RFID tag antenna design and does not include RFID reader antenna development or large-scale field deployment. The antenna performance is evaluated under controlled laboratory conditions using standardized measurement procedures.

1.5 Thesis Outline

Chapter 1 introduces the research topic and presents the research background, problem statement, objectives, scope of study, and thesis organization. This chapter establishes the motivation for developing compact and high-performance UHF passive RFID tag antennas suitable for metallic environments.

Chapter 2 provides an overview of RFID technology and its applications, followed by a comprehensive review of related literature on RFID systems and UHF RFID tag antenna design. Conventional impedance matching techniques and miniaturization methods adopted by previous researchers are critically examined. A detailed review of on-metal RFID tag antennas is also presented, highlighting the technical challenges associated with metallic deployment. Furthermore, metasurface integration with RFID tag antennas is discussed, and the associated limitations and technical issues are analyzed. Existing miniaturization strategies, impedance tuning approaches, and metasurface-based enhancement techniques are systematically evaluated to identify research gaps that form the foundation of this study.

Chapter 3 describes the research methodology, outlining the essential procedures involved in designing and analyzing the UHF passive RFID tag antenna for on-metal applications. A general flowchart illustrates the overall modelling and development process of the two antenna configurations investigated. This chapter details the design specifications, key technical parameters, and relevant theoretical formulations related to dipolar patch antenna behaviour, read range estimation, and Huygens' electromagnetic principles. The simulation procedures, fabrication techniques, and experimental measurement setups are also comprehensively described to ensure systematic performance evaluation.

Chapter 4 presents the design and development of the miniaturized folded-patch UHF RFID tag antenna incorporating a stub configuration and tuning slot mechanism. The influence of geometrical parameters on resonant frequency, input impedance, and radiation characteristics is systematically analyzed. The simulation results are subsequently validated through fabrication and experimental measurements under metallic mounting conditions.

Chapter 5 extends the antenna design through the integration of a Huygens' Meta-Element (HME) structure to enhance radiation directivity and gain performance. The electromagnetic behaviour of the combined antenna–HME system is investigated using full-wave simulations and experimental validation. Performance improvements in terms of gain, power transmission coefficient, and read range are evaluated and compared with the baseline antenna design.

Chapter 6 concludes the thesis by summarizing the major findings and contributions of the research. Suggestions for future work are also presented in this chapter.

CHAPTER 2
LITERATURE REVIEW

2.1 Introduction

The chapter begins with a review of RFID technology fundamentals, including system architecture, operating frequency bands, and major application domains. The proposed antenna is intended for compact, non-wearable passive UHF RFID applications involving metallic assets in industrial environments, such as logistics, asset tracking, warehouse management, and manufacturing. Unlike wearable RFID antennas, which prioritize flexibility and conformity to the human body, the proposed antenna is optimized for mounting directly on metallic surfaces. Accordingly, the design emphasizes compact dimensions, stable impedance matching, high radiation efficiency, gain enhancement, and reliable read-range performance while minimizing the frequency detuning effects caused by conductive objects.

Subsequently, existing UHF RFID tag antenna structures are critically examined. Conventional dipole-based tags, patch-type configurations, and metal-mountable designs are reviewed, with emphasis on their radiation characteristics, impedance behavior, and sensitivity to surrounding materials. The limitations of traditional tag antennas in metallic environments, such as impedance detuning and radiation degradation, are analyzed in detail. In addition, various miniaturization and impedance-matching techniques reported in the literature are evaluated, highlighting the trade-offs among compactness, bandwidth, efficiency, and fabrication complexity.

The integration of metasurface and metamaterial concepts, including Artificial Magnetic Conductors (AMC) and other high-impedance structures, is then explored as a means of enhancing metal tolerance and radiation stability. Finally, recent advancements in Huygens metasurface concepts are introduced, providing the theoretical basis for achieving balanced electric–magnetic responses and improved wavefront control.

2.2 RFID Technology and Applications

This section discusses the fundamental components of an RFID system, the operating frequency bands, and the implementation of RFID technology in various applications.

2.2.1 RFID System Components

Radio Frequency Identification (RFID) is an automatic identification technology that utilizes electromagnetic fields and radio waves to enable wireless detection, identification and tracking of objects (Murugesh et al., 2020) . Figure 2.1 illustrates the basic components of a typical RFID system. The system typically consists of four key elements which are the RFID tag, RFID reader, a host computer, and communication network (Hussain et al., 2020a).

The RFID reader serves as the central unit of the system, facilitating communication between the RFID tag and the host system. It comprises two main modules: the RF module and the control module. The RF module is responsible for transmitting and receiving radio frequency signals between the reader and the tag, while the control module interfaces with a controller or computer system that runs the application software for data processing and storage. RFID readers may operate in read-only mode, in which the data is read and transmitted unidirectionally from the tag to the reader, or in read–write mode, which enables bidirectional communication, allowing data to be both read from and written to the tag.

The RFID tag is a critical component of an RFID system. It consists of an antenna for receiving and transmitting RF signals, and a microchip for storing and processing data. The impedance of the RFID chip is typically complex, and conjugate impedance matching between the chip and the tag antenna is essential to achieve efficient power transfer. When the tag is located within the electromagnetic field generated by the reader, the antenna captures a portion of the transmitted energy to activate the chip circuitry. The tag then transmits the stored data back to the reader using the backscattering technique(N. Miswadi et al., 2024).

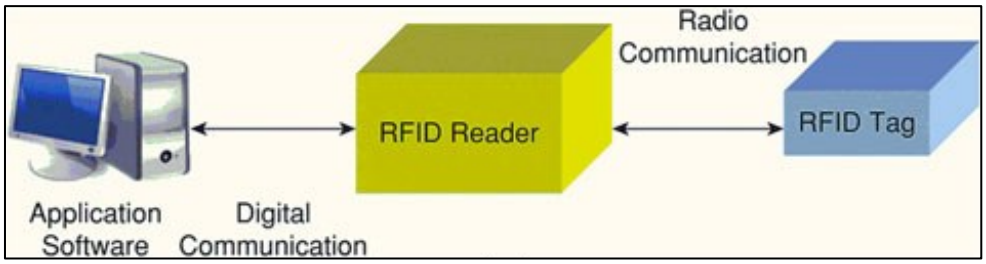


Figure 2.1 Basic Components of an RFID System.(Hussain et al., 2020)

RFID tags are generally classified into two categories based on their power source: active and passive (Hussain et al., 2020a). Active RFID tags contain an internal battery that powers the circuitry and enables communication without relying on energy from the reader. These tags offer a longer read range and are commonly used in asset tracking applications. However, they are larger in size and more expensive due to the additional circuitry required. In contrast, passive RFID tags do not contain an internal power source and rely entirely on the energy emitted by the RFID reader. They operate by receiving and reflecting the reader's signal through backscatter modulation. Although passive tags are less suitable for real-time tracking, they are ideal for simple identification and data retrieval tasks, offering advantages of smaller size, lower cost, and easier fabrication compared to active tags.

2.2.2 RFID Operating Frequency

RFID systems operate across a wide range of electromagnetic spectrum, typically between 124 kHz and 5.8 GHz, and are generally classified into four main categories based on their operating frequency: low frequency (LF), high frequency (HF), ultra-high frequency (UHF), and microwave bands (Costa et al., 2021; Radiocommunication Sector of ITU, 2012; Ripin et al., 2020).

The low-frequency (LF) band, typically operating between 125 kHz and 134 kHz, is primarily used in access control systems and product authentication applications. LF RFID systems rely on a magnetic coupling mechanism, where magnetic fields transfer energy between the reader and the tag. This coupling method enables LF systems to operate reliably in harsh environments. However, the LF band is limited by its short reading distance, usually restricted to only a few centimeters, and its low data transfer rate, which confines its use to short-range, low-speed applications. (Ripin et al., 2020).

The high frequency (HF) band operates at 13.56 MHz and represents a balanced trade-off between performance and cost(Cui et al., 2019). Like LF, HF RFID uses near-field inductive coupling, but the higher frequency allows for greater data rates and extended read ranges, typically up to 1–1.5 m depending on system configuration. Due to its low production cost and moderate range, HF RFID has become a dominant choice for applications such as contactless smart cards, library management systems, ticketing, airline baggage tracking, and near-field communication (NFC) (Rizkalla et al., 2018).

The ultra-high frequency (UHF) band, which spans 860 MHz to 960 MHz, has become the most widely adopted range for industrial, commercial, and logistics applications. Unlike LF and HF systems, UHF RFID operates based on electromagnetic coupling, which enables longer read ranges typically exceeding 3m for passive tags and extending to 10m for active systems as well as higher data transfer rates and faster tag recognition. These characteristics make UHF RFID particularly suitable for supply chain automation, asset tracking, inventory management, and electronic toll collection(Nguyen et al., 2023). However, UHF RFID frequencies are not globally harmonized, as different regions allocate distinct sub-bands: 865–868 MHz in Europe, 902–928 MHz in the United States, and 920–925 MHz in most Asia–Pacific countries, including Malaysia, as illustrated in Figure 2.2(Toaha et al., 2011). Despite its numerous advantages, the performance of UHF RFID systems can be adversely affected by environmental conditions, such as multipath reflections, high dielectric surroundings, and metallic interference, which must be mitigated through careful antenna design and impedance matching to ensure optimal system performance(Erman & Koziel, 2022; Paramasivam et al., 2024).

At the higher end of the spectrum, microwave RFID systems operate at 2.45 GHz and 5.8 GHz, offering very high data transmission rates, reaching up to 64 kbps, and supporting passive, semi-passive, or active tag configurations(Jialong, 2023). The microwave band is increasingly favored due to the growing demand for multi-frequency devices used in applications such as Wi-Fi, Bluetooth, and smart home technologies(Korfiati et al., 2024). However, microwave signals are more vulnerable to attenuation when propagating through materials containing water or metal, which reduces their reliability in certain environments.

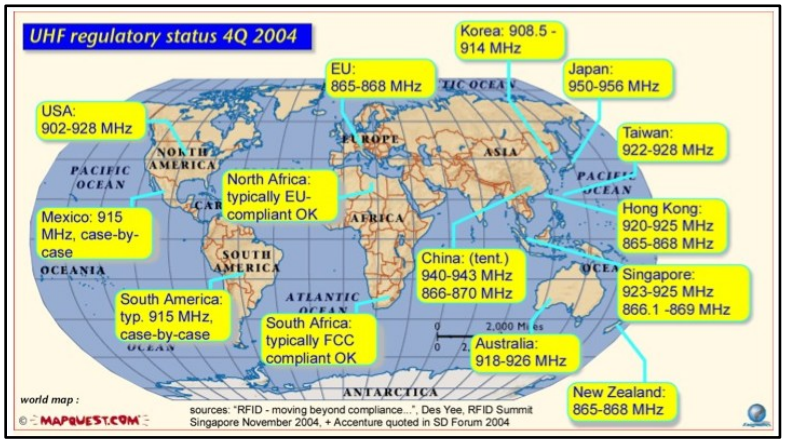


Figure 2.2 UHF-RFID Frequency Allocation Throughout the World(Toaha et al., 2011)

2.2.3 RFID Applications

Radio Frequency Identification (RFID) technology has been widely adopted across numerous sectors due to its capability for non-contact, automatic identification and real-time data acquisition (Y. H. Lee et al., 2020; N. Miswadi et al., 2024; NF. Miswadi et al., 2022). By utilizing electromagnetic coupling between a tag and reader, RFID systems enable efficient monitoring, tracking, and management of physical assets without requiring line-of-sight communication. The applications of RFID, as illustrated in Figure 2.3 include logistics, asset tracking, supply-chain management, vehicle identification, healthcare, and the Internet of Things (IoT).

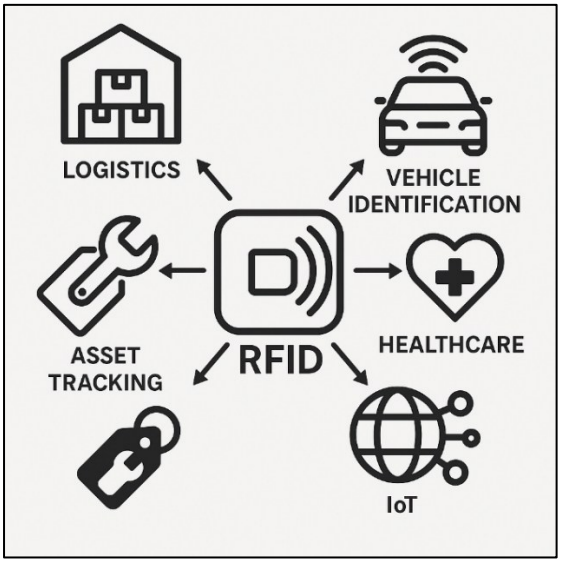


Figure 2.3 RFID Technology Applications Across Various Sectors. (N. F. Miswadi et al., 2022)

In logistics and supply-chain management, RFID enhances operational visibility by allowing automated tracking of goods throughout the distribution process. Tags embedded on pallets, containers, or individual products enable continuous data collection on location and movement(Khan et al., 2016). This automation reduces human error and improves inventory accuracy, while also facilitating faster receiving, sorting, and dispatching processes, which ultimately enhance overall productivity in warehouse management.

Asset tracking and vehicle identification are also major application areas of RFID (Islam et al., 2018; S. Lee et al., 2020; S. R. Lee et al., 2022a; Räsänen et al., 2024) .Asset tracking employs RFID to monitor valuable or mobile assets such as tools, equipment, and machinery. By assigning unique tag identifiers, organizations can record the real-time status and location of assets, thereby minimize loss and theft while ensure optimal utilization. For vehicle identification, RFID tags embedded on license plates or windshields are used in toll collection, access control, and parking management systems. These systems provide seamless and contactless vehicle authentication, improving traffic flow and operational efficiency.

In the growing field of the Internet of Things (IoT), RFID serves as a foundational technology for connecting physical objects to digital systems(Lubna et al., 2022). RFID tags function as data nodes within IoT ecosystems, enabling real-time monitoring in applications such as smart identification, smart homes, smart shopping, smart agriculture, and health monitoring, as illustrated in Figure 2.4. Within the healthcare sector, RFID plays a vital role in patient identification, medication administration, and inventory control of medical equipment. The ability to accurately track patient records and medication doses enhances safety and minimizes the risk of medical errors.

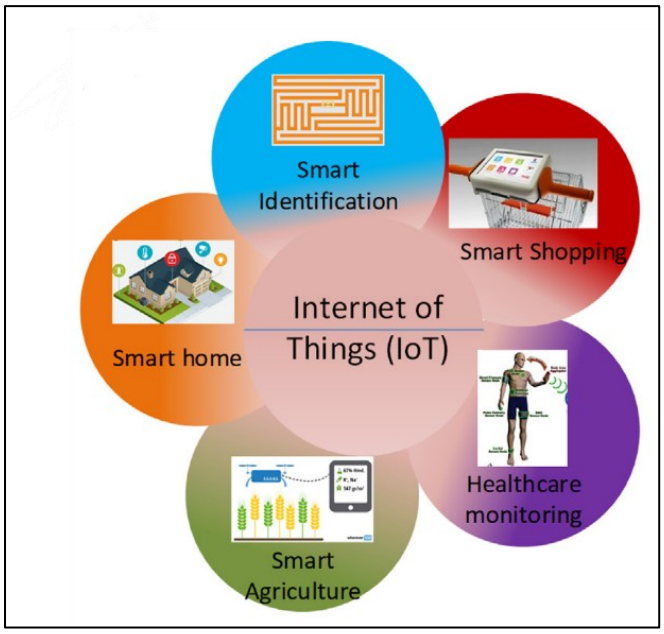


Figure 2.4 Integration of IoT ecosystem in RFID.(Lubna et al., 2022)

2.3 Previous Work on RFID Tag Antennas

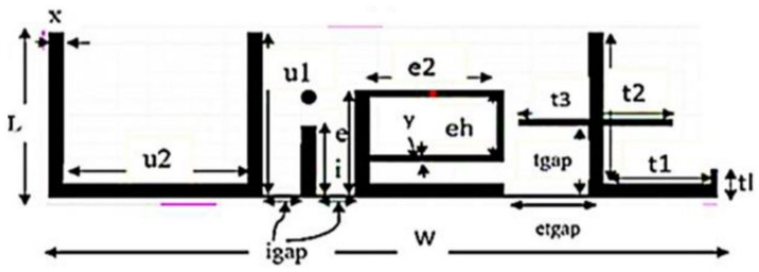
This subsection reviews the existing research and development of RFID tag antennas, with emphasis on UHF passive designs. Various antenna configurations reported in the literature are examined, including conventional dipole-based structures, patch-type antennas, and metal-mountable solutions. The design methodologies, impedance-matching techniques, miniaturization approaches, and performance characteristics of these antennas are discussed to highlight their advantages and limitations. This review provides a critical foundation for identifying current challenges and research gaps in RFID tag antenna development.

2.3.1 Review of UHF RFID Tag Antenna Designs

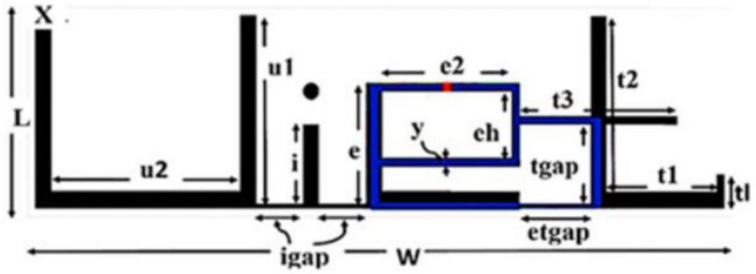
The design of passive UHF RFID tag antennas is a critical factor in achieving reliable identification and long read range in practical RFID systems. One of the key design challenges is ensuring efficient impedance matching between the antenna and the RFID microchip. To achieve optimal power transfer, the antenna impedance must be the complex conjugate of the chip impedance. Deviations in the antenna reactance can significantly reduce the power transfer coefficient (τ) and consequently shorten the read range. Since passive RFID tags rely solely on energy harvested from the reader, a lower power transmission coefficient (τ) reduces the power delivered to the microchip, resulting in a shorter read range. Therefore, maintaining a high τ through effective

impedance matching is essential for maximizing read-range performance, particularly in on-metal environments where impedance detuning is significant. Several feeding and matching techniques have been utilized to address this challenge such as through direct feeding, capacitive coupling, or T-match configurations.

T-matching network has been widely adopted for impedance matching in RFID tag antenna due to its simplicity and effectiveness in achieving conjugate matching between the antenna and RFID microchip (A. A. Sharatol Ahmad Shah et al., 2018; Choudhary et al., 2018; N.M.Faudzi, 2014; Wickramasinghe et al., 2021) . A compact UHF RFID tag design employing a double T-matching network combined with an alphabetical loop-pattern geometry was proposed in (Choudhary et al., 2018). Both single and double T-matching configurations were investigated, as illustrated in Figure 2.5. The double T-matching configuration demonstrated stable gain and radiation efficiency across the 800–1000 MHz frequency band. The tag was implemented on both hard (FR-4) and flexible (polycarbonate) substrates and validated using Higgs-4 and Impinj Monza R6 chips. Simulation and measurement results showed improved impedance matching, high radiation efficiency of up to 81.5%, and a gain of approximately 1.7 dBi, achieving a maximum read range of 18 m. Nevertheless, although the design exhibits wideband operation and long read range, it was characterized only in free-space, and its performance when mounted on metallic or other non-metallic materials was not evaluated. Since metallic surfaces introduce severe impedance detuning and radiation degradation, the applicability of the proposed T-matching structure for on-metal RFID applications remains uncertain. This limitation highlights the need for compact RFID tag antenna designs that can maintain effective impedance matching and stable performance under metallic mounting conditions, which is one of the objectives of the research.



(a)



(b)

Figure 2.5 Top View of the Tag Antenna Configuration With (a) Single T-Matching And (b) Double T-Matching.(Choudhary et al., 2018)

The work reported in (A. A. Sharatol Ahmad Shah et al., 2018) presents the development of wearable UHF RFID tag antennas utilizing copper-core electro-textile fabric as the radiating element and polyester as the substrate. Two antenna configurations were designed and analyzed based on the T-match network to achieve conjugate impedance matching, with the equivalent T-match circuit illustrated in Figure 2.6 . The tag employed an NXP G2XM chip with an impedance of 22 + j6 Ω. Parametric and optimization studies conducted using CST Studio demonstrated that the T-match configuration has a significant influence on impedance matching and the reflection coefficient. The optimized tag antenna achieved a resonant frequency of approximately 921 MHz with an impedance of 33 + j0.95 Ω and a gain of 1.4 dB.

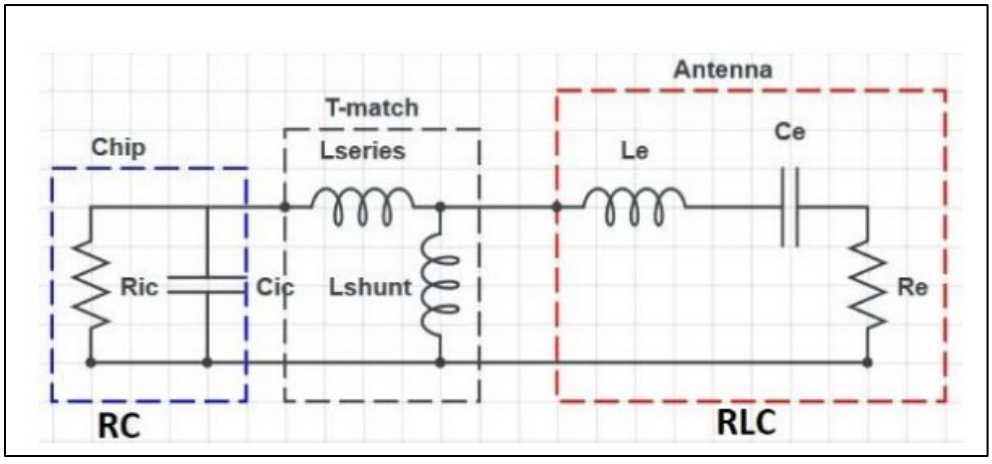


Figure 2.6 T-Match Equivalent Circuit.(A. A. Sharatol Ahmad Shah et al., 2018)

Subsequently, a passive UHF RFID tag antenna with a modified T-match structure for sensor applications was reported in (Wickramasinghe et al., 2021). Using the Farsens Rocky100 RFID IC with impedance of 64 – j469 Ω at 868 MHz, the antenna was fabricated on an FR4 substrate and optimized through parametric simulations in

Ansys HFSS. A modified T-match configuration incorporating a parallel bridge and folded dipole arms was proposed to enhance impedance matching and achieve a more compact design, as illustrated in Figure 2.7. The optimized antenna achieved near-conjugate matching of 62.5 + j471.6 Ω, corresponding to a power transmission coefficient of 0.998. The antenna achieved an impedance bandwidth of 280 MHz, and a realized gain of 1.66 dB, resulting in a theoretical read range of approximately 2.36 m. Despite the excellent impedance matching performance, the antenna demonstrated a limited read range and relatively bulky physical dimensions, which reduces its practicality for compact RFID applications.

Overall, the T-match feeding network has proven to be an effective method to achieve impedance matching without the need for external components (A. A. Sharatol Ahmad Shah et al., 2018; Wickramasinghe et al., 2021). However, these studies have focused mainly on free-space performance and have not addressed the impedance detuning and radiation degradation caused by metallic surfaces. This research gap motivates the development of compact on-metal UHF RFID tag antennas with improved impedance matching and stable read-range performance.

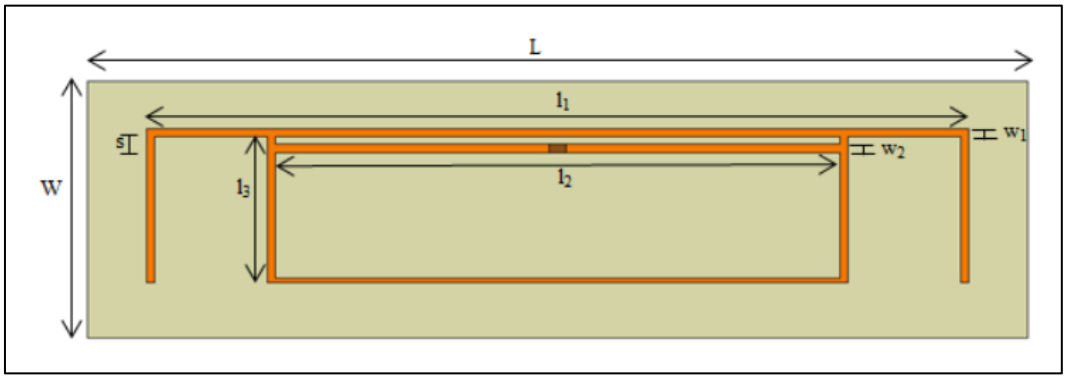


Figure 2.7 Proposed Modified T-Matched RFID Tag Antenna Design Incorporating a Parallel Bridge and Folded Dipole Arms.(Wickramasinghe et al., 2021)

Another technique to achieve perfectly good matching between tag antenna RFID chips is inductively coupled feed (Bansal et al., 2019, 2022; Ma et al., 2020). In this approach, as illustrated in Figure 2.8, the inductively coupled feed configuration comprises a feeding loop placed adjacent to the resonant body, establishing magnetic coupling between the two structures(Turitsyna & Webb, 2005). The RFID chip is directly connected to the terminals of the loop, while the loop itself is inductively linked to the main radiating element. This interaction generates a mutual inductance (M) that governs the energy transfer between the loop and the radiator, as represented in the

equivalent circuit in Figure 2.8 . By adjusting the separation distance between the loop and the radiating body or fine-tuning the loop geometry, the antenna's input impedance can be precisely optimized to achieve effective conjugate matching with the RFID chip.

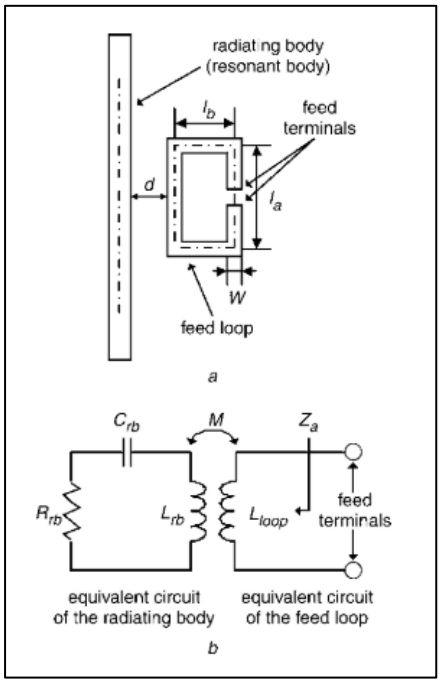


Figure 2.8 Configuration of Inductively Coupled Feed and Its Equivalent Circuit. (Turitsyna & Webb, 2005)

Bansal et al. (Bansal et al., 2022)presented a compact dual-band UHF RFID tag antenna designed to operate in both the European (866 MHz) and U.S. (915 MHz) bands. The proposed structure employs a 9-shaped folded dipole inductively coupled to a spiral loop feed network as depicted in Figure 2.9, providing the necessary inductive reactance to achieve conjugate matching with the capacitive impedance of the Alien Higgs-3 chip. Fabricated on an RO4350 substrate, the tag achieved excellent impedance matching (≈ 27 + j202 Ω) and realized gains of 1.85–1.92 dB. The measured read ranges reached 9.2 m at 866 MHz and 9.5 m at 915 MHz with 4 W EIRP, exhibiting stable bidirectional radiation in the E-plane and omnidirectional patterns in the H-plane. While the paper demonstrates an effective dual-band UHF RFID tag design with strong impedance matching and impressive read-range performance, its evaluation was limited to non-metallic and dielectric platforms. The tag's performance was tested only in free space and on materials such as wood, glass, fiber, and foam, no assessment was conducted on metallic or high-conductivity surfaces, which are known to induce

detuning and radiation degradation. Consequently, the design's reliability for on-metal environments remains unverified.

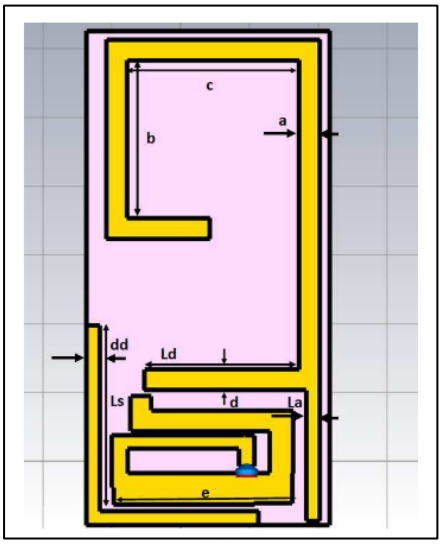


Figure 2.9 Proposed Dual-Band RFID Tag Antenna Configuration and Its Inductively Coupled Spiral Loop Feed Network(Bansal et al., 2022)

Stub-matching techniques have also been implemented using short sections of transmission line(J. Ali et al., 2022; Chen et al., 2013; Tan et al., 2020) . In UHF RFID tag antenna designs, an open- or short-circuited stub is typically incorporated into the radiating element or feed network to tune the overall reactance. By appropriately adjusting the stub length and position, the reactive component of the antenna impedance can be precisely controlled to compensate for the typically capacitive impedance of the RFID chip.

Nguyen et al. (Tan et al., 2020) presented a compact inverted-F antenna (IFA) specifically designed for UHF RFID tags operating on high-permittivity materials such as liquid-filled containers. The proposed antenna structure consists of a rectangular radiating plate, a ground plane, and a vertical rectangular loop integrated with a shorting stub used for impedance matching as shown in Figure 2.10. The stub position is a crucial design parameter for tuning the antenna impedance to achieve conjugate matching with the Alien Higgs-4 chip with input impedance of 8.5 – j151 Ω at 915 MHz. Fabricated on an FR4 substrate, the optimized antenna exhibited an omnidirectional radiation pattern and achieved a maximum measured read range of 5.7 m when it was mounted on a full water container under a transmitted power of 4 W EIRP. However, the study did not include read range evaluation on metallic surfaces, leaving its performance on conductive platforms unverified.

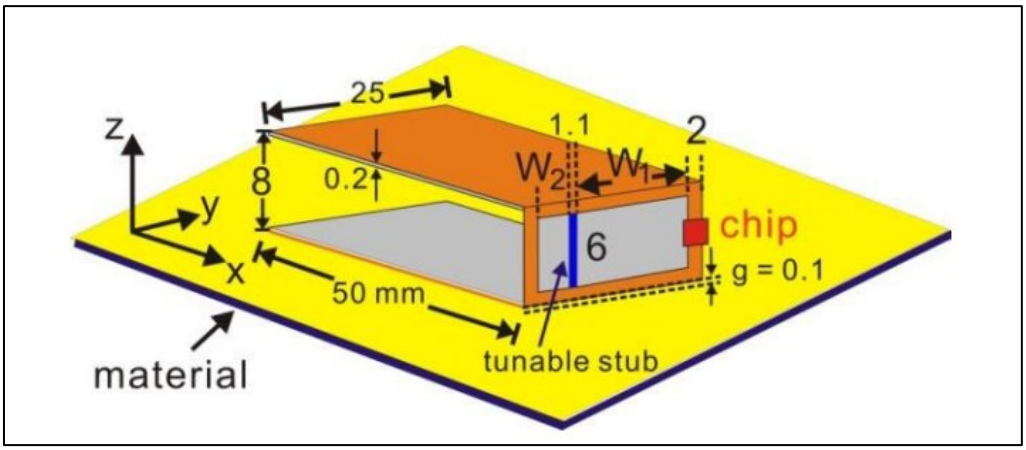


Figure 2.10 Proposed Geometry of Inverted-F Antenna (IFA) With Shorting Stub. (Tan et al., 2020)

Another critical design consideration in UHF RFID tag antenna development is the miniaturization of the antenna while maintaining adequate radiation performance. Compact tag antennas are highly desirable due to their cost efficiency, mechanical robustness, and ease of integration into various products or packaging. However, electrically small antennas inherently exhibit a high-quality factor (Q), which leads to reduced radiation efficiency and limited read ranges (N. Miswadi et al., 2024; Salman et al., 2017). Furthermore, common miniaturization techniques such as meandering, folding, or capacitive loading extend the effective surface current path but simultaneously confine the current distribution to a smaller radiating area, thereby lowering radiation efficiency. Consequently, achieving an optimal balance between antenna compactness, read range, and gain remains a fundamental design trade-off in developing high-performance UHF RFID tag antennas.

To address these challenges, several studies have employed meandering techniques to effectively increase the electrical path length without enlarging the antenna footprint (Bhaskar & Singh, 2021; Lin et al., 2019; P. Wongsiritorn et al., 2009) . Bhaskar and Singh (Bhaskar & Singh, 2021) presented a compact UHF RFID tag antenna that utilized a meander-line structure integrated with spiral inductors, a T-match network, and an inductively coupled parasitic element to achieve both miniaturization and impedance matching at 915 MHz, as shown in Figure 2.11. The structure successfully reduced the resonant frequency from 4 GHz to 915 MHz by applying a meandered dipole with end spiral loading, while maintaining good conjugate matching with the Alien Higgs IC chip (13.5 − j111 Ω) through the T-match network and inductive coupling. The fabricated antenna achieved a compact size of 50 mm × 12 mm

and exhibited an omnidirectional radiation pattern, demonstrating efficient operation despite its reduced dimensions. Although the proposed matching technique achieved satisfactory impedance matching, the realized gain remained relatively low, restricting the maximum read range to 3.5 m, as illustrated in Figure 2.11(b).

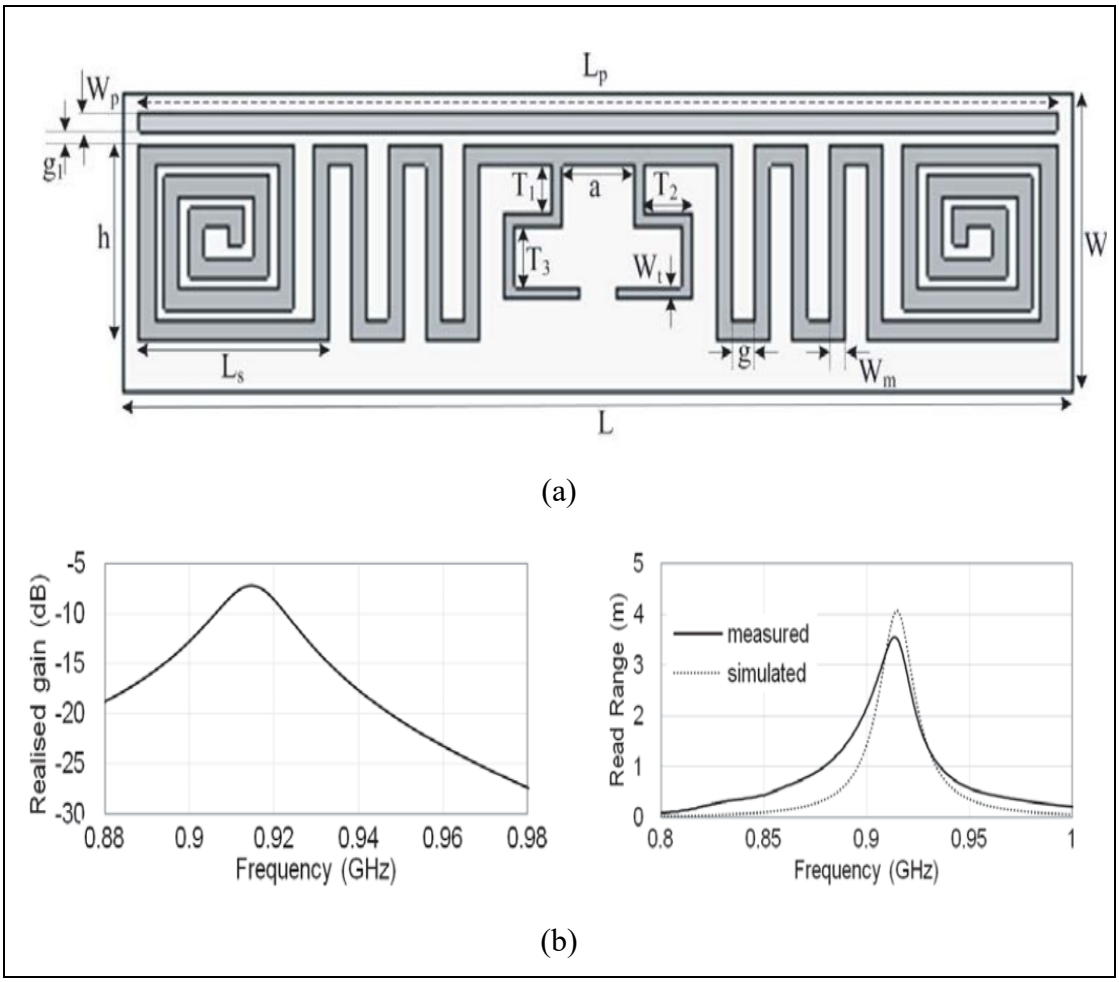


Figure 2.11 (a)Configuration (b) Realized gain and Read Range of Compact UHF RFID Tag Antenna. (Bhaskar & Singh, 2021)

Similarly, Wongsiritorn et al.(P. Wongsiritorn et al., 2009) proposed a meander-line UHF RFID tag antenna incorporating a semi-circular loop to achieve conjugate impedance matching with the NXP G2XL chip at 922.5 MHz, as illustrated in Figure 2.12. The compact design, with an electrical size of $0.10\lambda_0 \times 0.25\lambda_0$, demonstrated an omnidirectional radiation pattern and achieved power transmission efficiency of approximately 97.9%, validating the effectiveness of the meandering approach in realizing miniaturized tag antennas with satisfactory radiation performance.

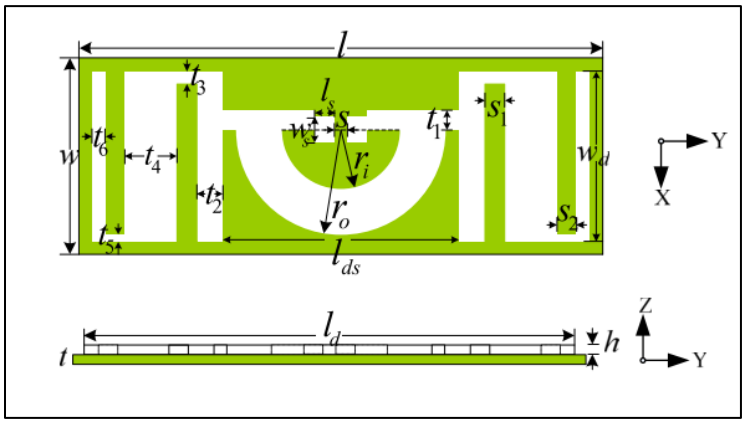


Figure 2.12 A Meander-Line UHF RFID Tag Antenna Incorporating a Semi-Circular Loop. (P. Wongsiritorn et al., 2009)

However, both designs exhibited limited read ranges of 3.5 m and 2.3 m, respectively, which may restrict their suitability for certain long-range RFID applications. This trade-off indicates that achieving effective impedance matching alone is insufficient to ensure long-range RFID performance. Furthermore, their performance on metallic or high-permittivity surfaces was not investigated, leaving the reliability of miniaturized UHF RFID tag antennas under practical deployment environments uncertain.

To further enhance antenna compactness without severely degrading radiation performance, several researchers have explored capacitive tip-loading techniques as an alternative or complementary approach to conventional meander-line miniaturization. Capacitive loading effectively lowers the resonant frequency by introducing additional capacitance at the antenna terminals, thereby increasing the effective electrical length while maintaining a smaller physical size(Bhaskar et al., 2019; Bhaskar & Singh, 2017; Farnana et al., 2024; Faudzi et al., 2016; N. F. Miswadi et al., 2022b; Shreya U. Naik et al., 2020).

Farhana et al.(Farnana et al., 2024) proposed a flexible UHF RFID tag antenna that evolved from a conventional meander-line configuration to zigzag geometries with bending angles of 90° and 45°, as illustrated in Figure 2.13. The zigzag structure effectively reduces the overall antenna length while mitigating the current cancellation problem inherent in conventional meander-line geometries. The orthogonal current paths in the zigzag configuration enhance radiation efficiency. To further miniaturize the antenna without compromising performance, capacitive tip loading was incorporated at the ends of the zigzag elements to lower the resonant frequency. The antennas were impedance-matched to the NXP UCODE G2iL chip using an inductively

coupled loop and operated at 920 MHz, achieving gains of 2.21 dBi for the 90° zigzag antenna and 1.89 dBi for the 45° design, respectively. This study demonstrates that evolving from meander-line to zigzag geometries, combined with capacitive tip loading, effectively enables antenna miniaturization while maintaining good radiation gain and efficiency. However, the study did not report the read range performance.

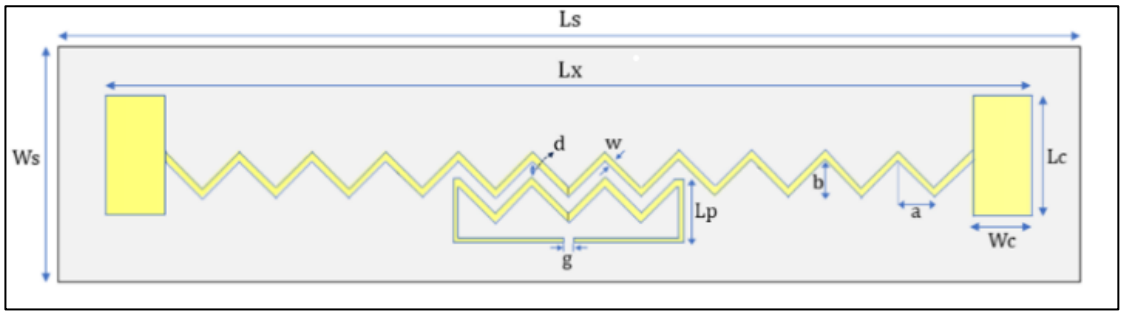


Figure 2.13 A Flexible UHF RFID Zigzag Dipole Tag Antenna.(Farnana et al., 2024)

Similarly, Naik et al. (Shreya U. Naik et al., 2020) designed a capacitive tip-loaded dipole antenna incorporating a T-match network on a Plexiglass substrate with a dielectric constant of 3.4 for the Impinj Monza R6-P chip with an impedance of 12.04 − j119.6 Ω. The capacitive tip loading, implemented by adding rectangular plates at both ends of the dipole arms as shown in Figure 2.14 (a), effectively minimized the antenna footprint. The proposed design achieved a return loss of −30.55 dB, a gain of 2.26 dB, and a measured read range of 15.5 m, demonstrating excellent impedance matching and radiation performance. Overall, both studies highlight the effectiveness of capacitive tip loading in achieving compact, high-efficiency UHF RFID tag antennas; however, despite the reported high gain and extended read range as shown in Figure 2.14(b), the performance of these antennas on metallic surfaces was not investigated, leaving their practical applicability in such environments unverified.

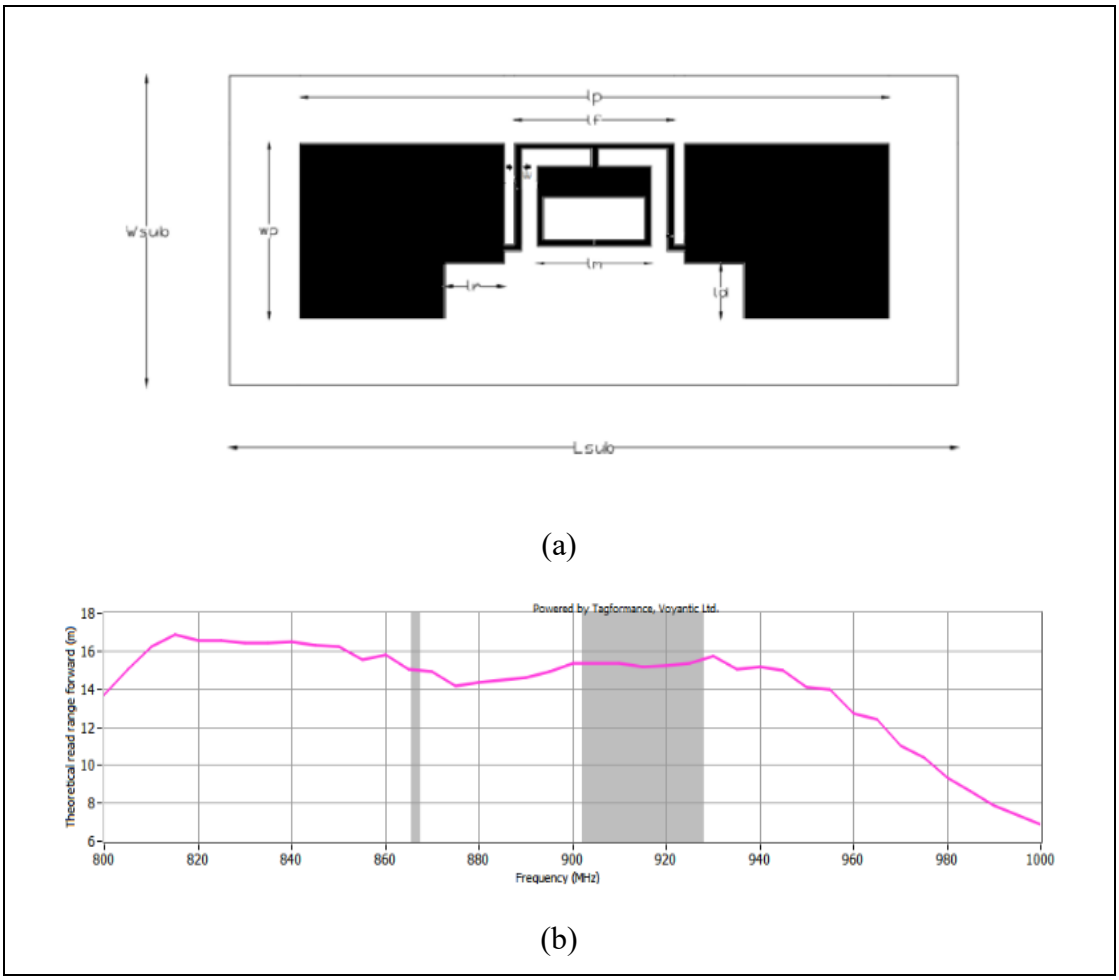


Figure 2.14 (a) Capacitive Tip-Loaded Dipole Antenna with A T-Match Network. (b) Maximum Read Range of the Tag Antenna (Shreya U. Naik et al., 2020)

Overall, previous studies have demonstrated that impedance matching techniques effectively enhance the performance of passive UHF RFID tag antennas. The T-matching network provides a simple and compact solution for achieving conjugate impedance matching, whereas stub matching offers greater flexibility in impedance tuning. Capacitive tip loading, on the other hand, enables antenna miniaturization while maintaining satisfactory impedance matching, achieving read ranges of up to 15 m under free-space conditions. Although these techniques improve impedance matching, gain, and read-range performance, most studies focus on optimizing individual performance parameters rather than achieving a balanced improvement in both radiation performance and compactness.

Furthermore, the reported designs were evaluated primarily under free-space conditions, without considering the impedance detuning and radiation degradation introduced by metallic surfaces. Consequently, their suitability for on-metal RFID applications remains uncertain. Therefore, further research is required to develop

compact impedance matching techniques that maintain stable conjugate matching and reliable read-range performance in metallic environments. The influence of metal proximity on RFID tag antenna performance is discussed further in Section 2.3.2.

2.3.2 UHF RFID Tag Antenna Designs for Metallic Environment

In practical deployment scenarios, UHF RFID tag antennas are typically mounted on or attached to a specific object's surface. The electromagnetic properties of the mounting platform can significantly influence antenna performance, particularly when the tag is placed in close proximity to metallic surfaces(Inserra et al., 2026; Lo & Chen, 2025; Murugesh & Akbar, 2025). In such cases, the presence of the conductive surface induces image currents of equal magnitude but opposite phase relative to the antenna current. These out-of-phase image currents effectively cancel the radiating currents on the tag antenna, resulting in suppressed radiation. Consequently, the radiation efficiency is substantially reduced, leading to a decrease in the achievable read range. In addition, the electromagnetic coupling between the antenna and the metal surface alters the input impedance characteristics of the tag, resulting in impedance detuning and potential mismatch with the RFID microchip. This impedance fluctuation further degrades power transfer efficiency and overall system performance(S. R. Lee et al., 2022a; Murugesh et al., 2022; Ripin et al., 2020).

Several studies have investigated the utilization of microstrip patch antenna structures for the development of RFID tag antennas capable of reliable operation on metallic surfaces (Alagiasundaram et al., 2023; López-Soriano & Parrón, 2015; Mo & Li, 2019; Muthukannan Murugesh et al., 2023). In these designs, a ground plane is incorporated as an integral part of the antenna configuration to mitigate the detrimental effects of the underlying metal. The inclusion of a ground plane provides electromagnetic isolation between the radiating element and the backing metallic surface. By acting as a shielding layer, the ground plane suppresses unwanted coupling and prevents the formation of destructive image currents that would otherwise detune the antenna. Consequently, the radiator can maintain more stable impedance characteristics and radiation performance, even when mounted directly on metal objects.

López-Soriano and Parrón (López-Soriano & Parrón, 2015) proposed a compact metal-mountable UHF RFID tag based on a short-ended microstrip patch backed by a

ground plane, as illustrated in Figure 2.15 , implemented using an FR4 substrate configuration By introducing a shorting mechanism and etching a slot on the patch, the electrical length was increased while maintaining a reduced physical size, resulting in a compact tag with overall dimensions of only 33.5 × 30 × 3.1 mm³. Furthermore, the integration of a ground plane beneath the radiating element, together with proximity coupling for impedance tuning, effectively mitigates destructive image currents and stabilizes the antenna impedance when mounted on metallic objects. As a result, the design achieves an approximate read range of 5 m despite its relatively small footprint, demonstrating the effectiveness of the ground-backed patch configuration for on-metal applications.

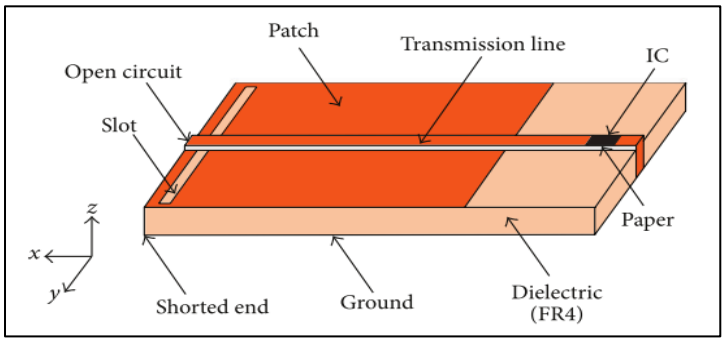


Figure 2.15 Geometry of the Short-Ended Patch Tag Antenna Mounted on an FR4 Substrate.(López-Soriano & Parrón, 2015)

A completely planar UHF RFID tag antenna employing a double-loop inductive-feed patch structure as shown in Figure 2.16(a)for metallic surface applications has been proposed in (Mo & Li, 2019). Unlike conventional microstrip or PIFA-based metal tags that require shorting vias or walls, the proposed design eliminates vertical interconnections while preserving a ground-backed configuration to ensure effective metal isolation. The double-loop inductive feed enhances current coherence on the radiating patch, such that the induced currents on both sides of the patch flow in the same direction, thereby improving radiation efficiency. Experimental results in Figure 2.16(b) demonstrate a measured read range of approximately **8**.4–8.8 m at 915 MHz when mounted on metal plates. The antenna exhibited a 3 dB bandwidth of approximately 133 MHz and a 10 dB impedance bandwidth exceeding 40 MHz, satisfying the UHF RFID frequency bands in both the USA and Europe. In addition, the measured read range remained above 8 m when the metallic plate size varied from 160 × 160 mm² to 400 × 400 mm², demonstrating stable performance across different metallic platform sizes. Nevertheless, although the design simplifies fabrication and

provides stable on-metal performance, its footprint of approximately 80 × 32 mm² remains relatively large.

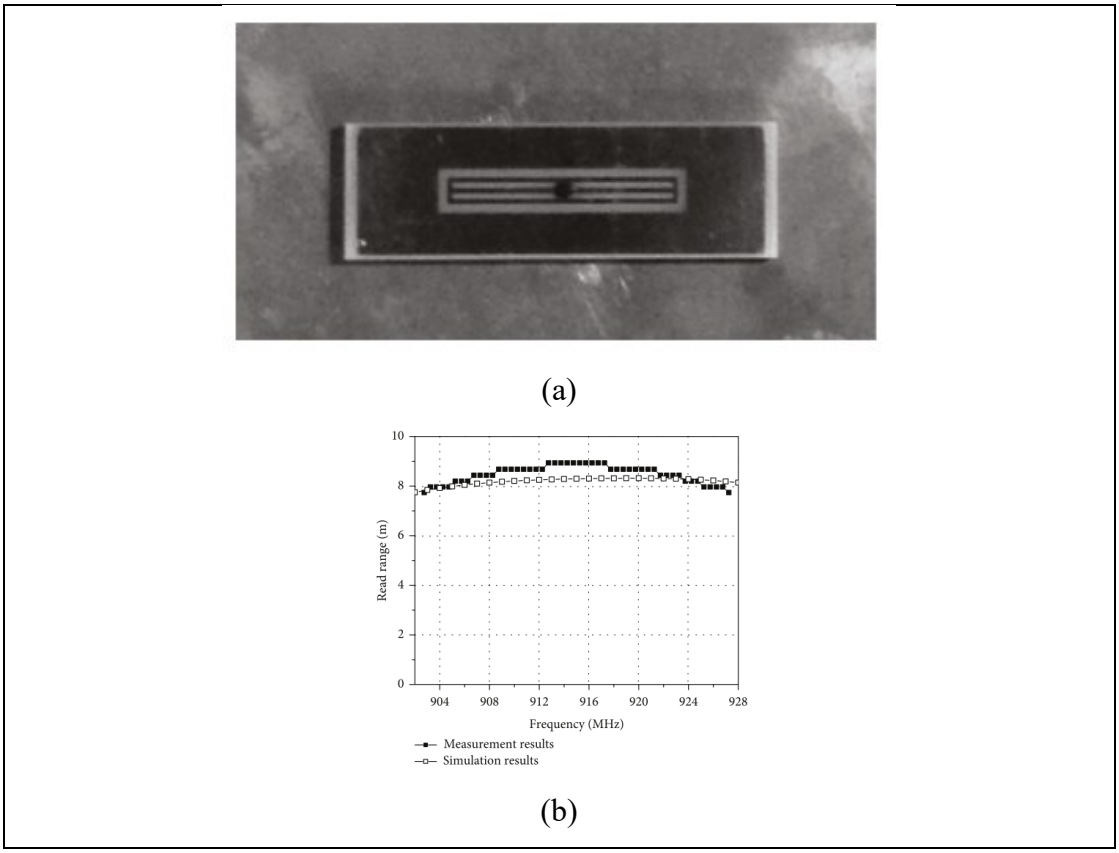


Figure 2.16 (a)Tag Prototype Mounting on the Copper Plate (b) Maximum Read Range in US band.(Mo & Li, 2019)

These two studies highlight the persistent trade-off between radiation performance, particularly in terms of read range, and physical compactness in on-metal RFID tag antenna design. The first design achieves a relatively compact footprint but exhibits a read range of only approximately 5 m, indicating that antenna miniaturization can compromise radiation performance. In contrast, the second design demonstrates an extended read range of up to 8 m; however, this improvement is attained at the expense of a significantly larger antenna footprint. Although both designs exhibit satisfactory on-metal operation, neither simultaneously achieves compact dimensions and long read-range performance. This limitation highlights the need for antenna designs that can balance miniaturization with enhanced radiation performance, thereby enabling compact on-metal RFID tag antennas without sacrificing read-range capability.

Furthermore, owing to the increasing demand for compact RFID tags in practical applications involving metallic environments, numerous antenna miniaturization techniques have been extensively investigated to ensure stable

performance while maintaining reduced physical dimensions. Among these approaches, different configurations of folded tag antennas have been widely reported in recent years due to their reduced physical dimensions and relatively simple fabrication process (F.-L. Bong et al., 2018; S. Lee et al., 2020; Ooi et al., 2022; Sun et al., 2017). The folded structure effectively increases the electrical length within a limited physical area, enabling size reduction while maintaining acceptable impedance characteristics and radiation performance.

Sun et al. (Sun et al., 2017) proposed an offset-fed folded dipole antenna with an open end, as illustrated in Figure 2.17 for UHF RFID tag applications capable of operating in both free-space and metallic environments. Unlike conventional center-fed folded dipoles, the antenna is excited near the shorting end, allowing the transmission-mode current to dominate and enabling the input impedance to be accurately predicted using a transmission-line model. This offset-feeding configuration provides relatively stable impedance characteristics even when the antenna is positioned vertically against a metallic surface, where it functions similarly to an inverted-F antenna. Experimental results demonstrate a read range of approximately 4 - 8 m at 915 MHz under both free-space and on-metal conditions. However, despite its impedance stability and dual-environment capability, the antenna dimensions (99 mm × 4.5 mm × 1.5 mm) result in a relatively elongated profile, which may limit its practicality for highly compact, low-profile on-metal RFID tag applications.

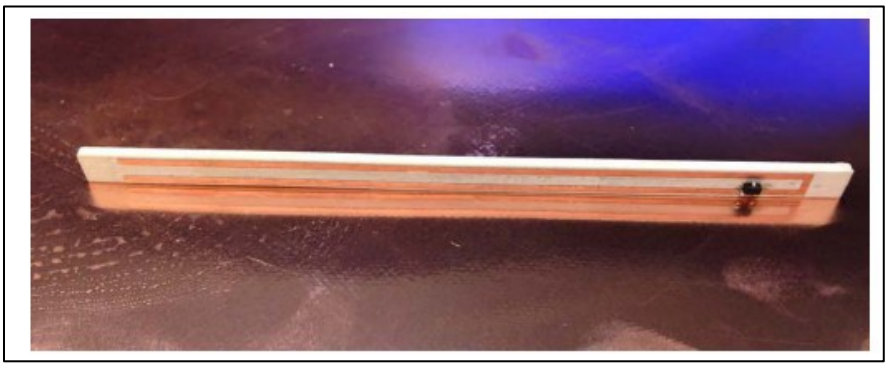


Figure 2.17 Fabricated Offset-Fed Folded Dipole Antenna with an Open End.(Sun et al., 2017)

A folded-dipolar patch RFID tag antenna for on-metal applications was presented in (F.-L. Bong et al., 2018), achieving a compact size of 30 mm × 30 mm and operating at approximately 924 MHz. The antenna demonstrated a maximum measured read range of approximately 3.5 m at 4 W EIRP when mounted on a metal plate, while

omnidirectional detection on dielectric surfaces was limited to distances beyond 2 m. As illustrated in Figure 2.18 (a) Patch A and Patch B form the first pair of dipoles whereas Patch C and Patch D form the second pair, with both dipoles arranged orthogonally and integrated with inductive tuning stubs. whereas Patch C and Patch D form the second pair, with both dipoles arranged orthogonally and integrated with inductive tuning stubs. This configuration eliminates the blind spots associated with a single dipole, thereby improving orientation-insensitive detection while maintaining a simple structure without lumped components, as confirmed by the tag sensitivity plot in Figure 2.18(b). Nevertheless, despite its compact configuration and polarization diversity, the antenna achieves only a limited read range of 3.5 m, indicating that the improved orientation coverage is attained at the expense of radiation performance, thereby restricting its suitability for long-range on-metal RFID applications.

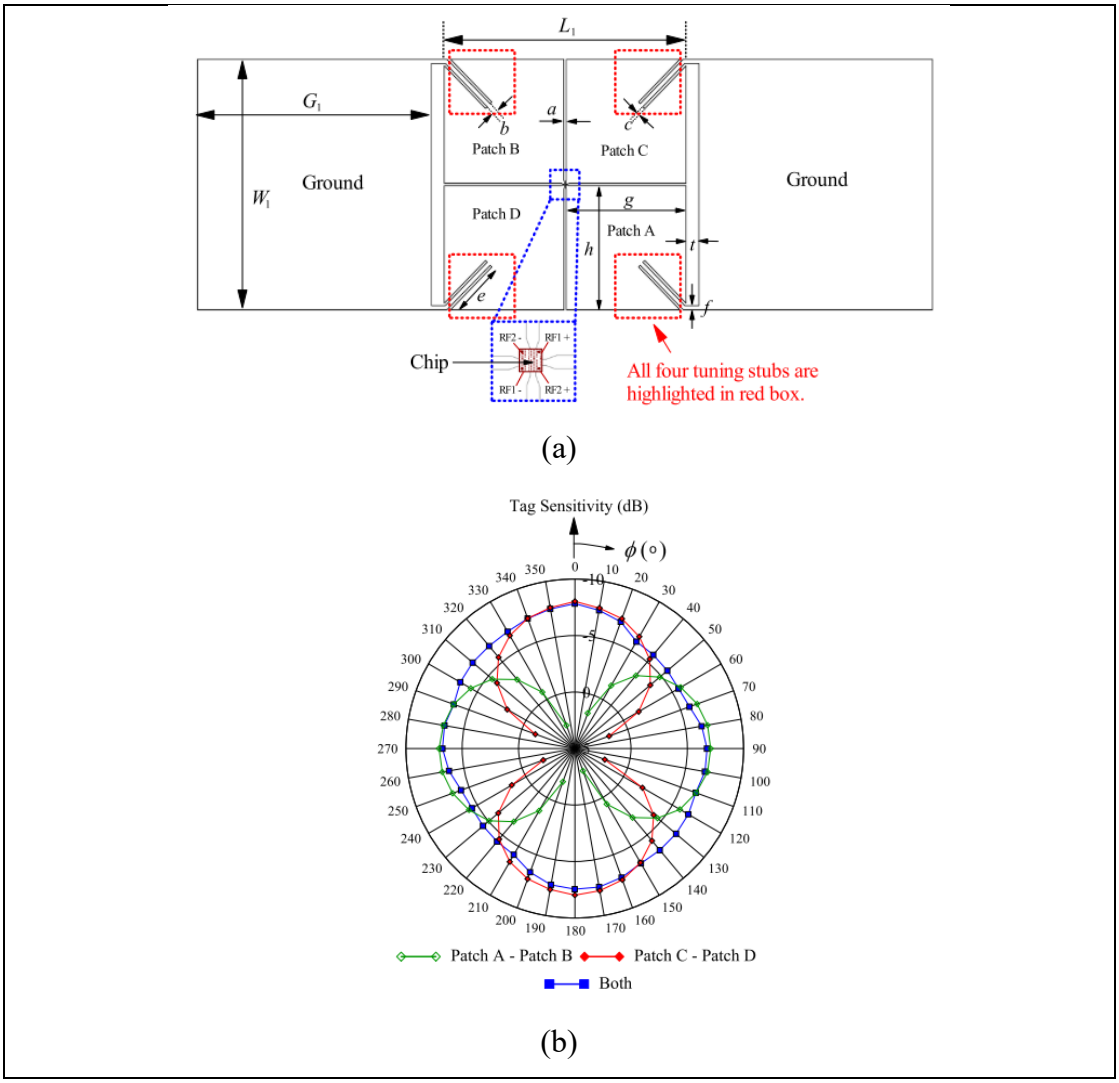
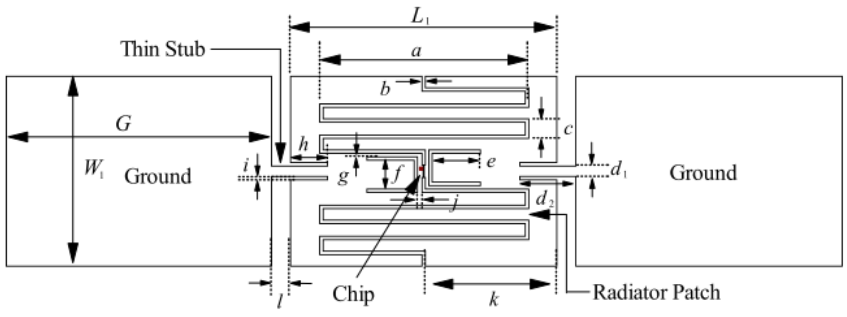


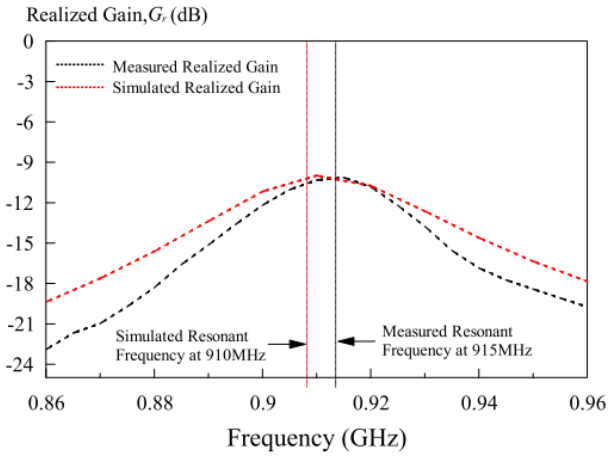
Figure 2.18 (a) Proposed Folded RFID Tag Antenna with Chip (b) Maximum Tag Sensitivity at 924 MHz. (F.-L. Bong et al., 2018)

It has been reported that the incorporation of multiple slots into folded-patch antenna structures is an effective miniaturization technique, as the introduced slots elongate the surface current path without increasing the overall physical dimensions. By perturbing the current distribution, the slots increase the effective electrical length of the radiator, thereby enabling resonance at lower frequencies within a compact footprint(Erman et al., 2020). Further studies have demonstrated that different slot geometries such as U-slots, meandered slots, L-shaped slots, and interdigitated slots can be strategically introduced to enhance impedance control and bandwidth characteristics while maintaining structural simplicity(F. L. Bong et al., 2017; Calabrese & Marrocco, 2008; Ooi et al., 2023).

A compact metal-mountable dipolar patch tag antenna with overall dimensions of 23 mm × 16 mm × 1.6 mm (approximately 0.0702λ × 0.0488λ × 0.0049λ) has been reported for UHF RFID applications (F. L. Bong et al., 2017). The antenna consists of a dipolar patch that is divided into two symmetrical dipolar arms by a centrally introduced narrow meandered slot as depicted in Figure 2.19(a). This highly reactive slot effectively increases the electrical current path, thereby lowering the resonant frequency without enlarging the physical size of the tag. Figure 2.19(b) shown the simulated and measured realized tag and show 5 MHz frequency deviation. Next, the eexperimental results demonstrated that the proposed design achieves a read range exceeding 4.5 m at 4 W EIRP when mounted on a metallic surface, and maintains a minimum read distance of approximately 2 m when deployed on dielectric materials with relative permittivity ranging from 1 to 12. Nevertheless, despite its compact footprint, the overall read range performance remains relatively limited.



(a)



(b)

Figure 2.19 (a)Tag Antenna Configuration with Narrow Meandered Slot (b) Realized Gain and Frequency Response.(F. L. Bong et al., 2017)

An H-shaped slot in conjunction with four adjustable stubs has been incorporated as the primary tuning mechanism to enable the tag antenna to operate across the global UHF RFID frequency bands(Zhang et al., 2017) . Through the reconfiguration of these tuning elements, frequency agility and impedance matching can be achieved. However, despite its multiband capability, the reported maximum read range is limited to approximately 1.8 m when mounted on metallic surfaces and 2.7 m in free-space conditions, indicating constrained radiation performance.

An electrically small folded-patch tag antenna incorporating multiple slots was reported in (Thirappa et al., 2019) to achieve substantial miniaturization, with overall dimensions of 23mm × 7.5 mm × 3.2 mm (approximately 552 mm³ in volume), as shown in Figure 2.20 . When tested on a metallic plate, the tag achieved a maximum read range of approximately 5.0 m. Although the slot-loading technique as shown in effectively increases the electrical path length and enables significant size reduction, the inclusion of multiple slots increases the stored reactive energy, leading to a higher Q-factor and reduced radiation efficiency. Consequently, despite its extremely compact footprint, the achievable read range remains relatively limited, indicating a trade-off between miniaturization and radiation performance.

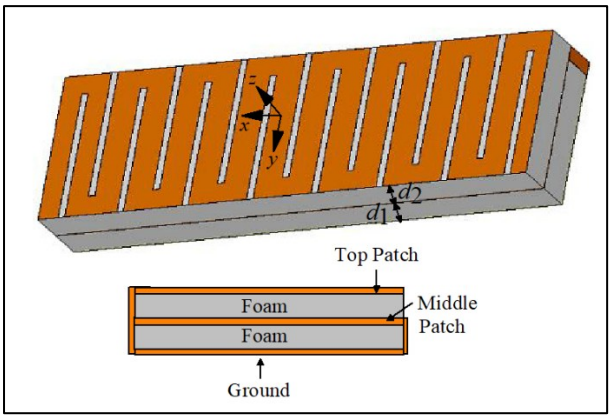


Figure 2.20 Three-Dimensional (3D) Configuration of the Proposed Tag Antenna and its Corresponding Structural View. (Thirappa et al., 2019)

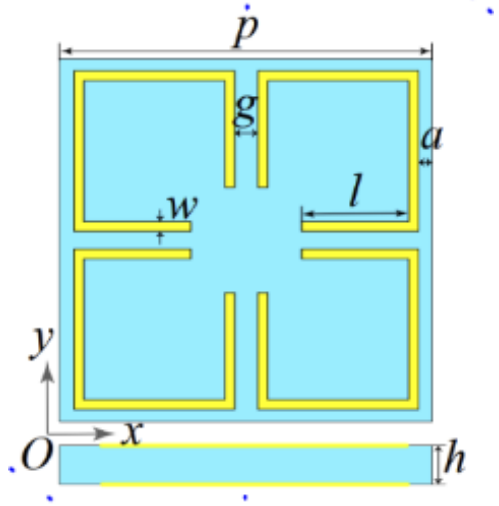
Overall, previous on-metal UHF RFID tag antenna designs have employed ground planes, folded configurations, and slot techniques to achieve compact dimensions and effective metal isolation. Nevertheless, these approaches generally compromise realized gain and read-range performance as antenna size is reduced. This inherent trade-off highlights the need for an efficient impedance tuning mechanism capable of balancing antenna miniaturization with enhanced radiation performance, thereby enabling compact on-metal RFID tag antennas with extended read-range capability.

2.3.3 Metasurface-Based Concepts in UHF RFID Tag Antenna Designs

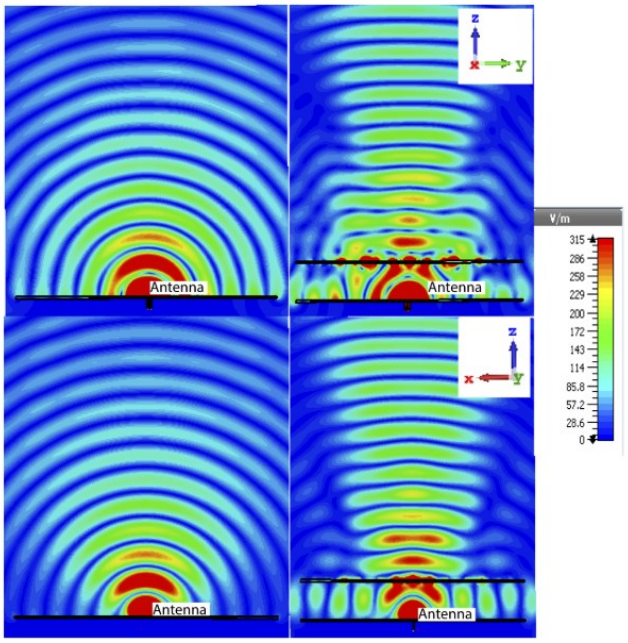
Over the past decades, metasurface and metamaterial concepts have been extensively incorporated into various antenna configurations to enhance electromagnetic performance. In general antenna engineering, metasurfaces have been employed to increase antenna gain, suppress sidelobes, shape radiation beams, and enable beam steering functionalities(S. Ali & Ghaffar, 2026; Y. Liu et al., 2026; Solanki et al., 2026).

For instance, a metasurface lens antenna based on a planar isotropic unit cell as illustrated in Figure 2.21(a) derived from Huygens' principle was reported in(Akram et al., 2020), where overlapping electric and magnetic resonances were engineered within the unit-cell geometry to achieve full 0 – 2π transmission phase control with high transmittance. The unit cells were arranged to form a metasurface lens operating at 9.3 GHz, and a square patch antenna was positioned at the focal point to convert the spherical wavefront of the source into a planar wavefront, thereby enhancing directivity as shown in Figure 2.21(b). The proposed lens antenna achieved a pencil-beam radiation

pattern with a simulated gain of 19.6 dB and experimental measurements of the fabricated prototype showed good agreement with simulation results, thus validating the enhanced gain and radiation performance of the design.



(a)



(b)

Figure 2.21 (a) Top and Side View of the Unit Cell (b) Electric Field Distribution with and without the Huygens' Lens.(Akram et al., 2020)

In addition, the Huygens' metasurface (HMS), which can be physically realized by co-locating orthogonal electric and magnetic surface currents, has been widely investigated for beam shaping and beam steering applications(Peng et al., 2020; Sakurai et al., 2021; Su et al., 2023; Vellucci et al., 2026). The double plus-shaped resonators are etched on the top and bottom surfaces of an F4B255 dielectric substrate (ε_r = 2.55,

tan δ = 0.001), as illustrated in Figure 2.22(Peng et al., 2020). The unit cell is analyzed using CST Microwave Studio with Floquet boundary conditions applied to emulate infinite periodicity. The simulated surface current distributions demonstrate the excitation of mutually orthogonal electric and magnetic resonances. By employing a simple bilayer unit-cell configuration and appropriately tuning the geometric parameters, these resonances at 9 GHz is satisfy the Huygens resonance condition, thereby achieving nearly 2π transmission phase coverage while maintaining transmission efficiency above 80%. This unit cell is subsequently employed in the design of a metasurface focusing lens.

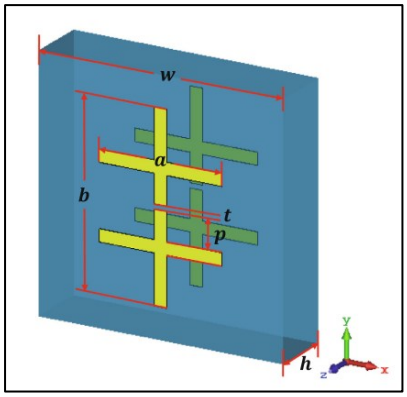
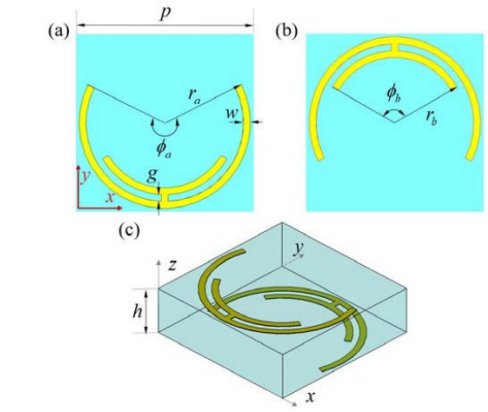
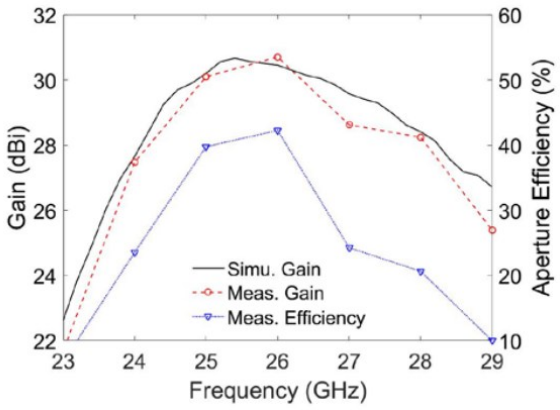


Figure 2.22 Design of the Proposed Square Unit Cell with its Geometric Parameters.(Peng et al., 2020)

Furthermore, broad-angle beam scanning with high gain has also been demonstrated using HMS-based configurations (Eleftheriades et al., 2022; Pourgholamhossein et al., 2022; Xue et al., 2020). A compact double-layered Huygens' metasurface lens antenna was proposed in(Xue et al., 2020) , where antisymmetric semicircular arc elements were printed on both sides of a single dielectric substrate to induce balanced electric and magnetic currents without employing separate magnetic dipole structures or vias as depicted in Figure 2.23. Huygens' unit cell achieved over 400° transmission phase coverage with transmission amplitudes better than −2.3 dB. he metasurface lens designed using the proposed Huygens' unit cell achieved a measured peak gain of 30.7 dBi at 26 GHz with 42% radiation efficiency, as shown in Figure 2.23(b). In addition, its 3 dB gain bandwidth fully covers the targeted 26 GHz 5G band, indicating broadband.



(a)



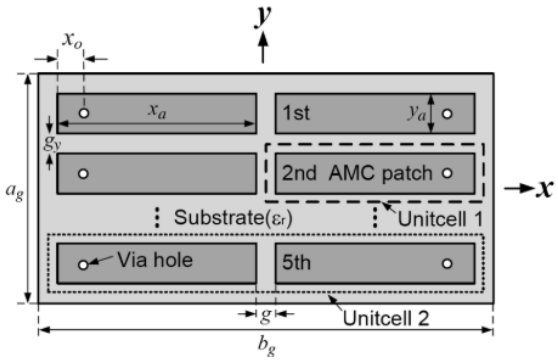
(b)

Figure 2.23 Top View, Bottom View, And Three-Dimensional (3D) Configuration of the Proposed Unit Cell.(Xue et al., 2020)

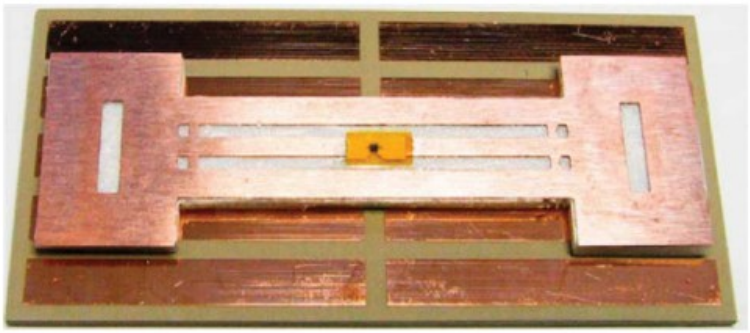
More recently, meta concepts have been extended to the design of anti-metal UHF RFID tag antennas(Casula et al., 2024; Luo & Wang, 2023; Sarkar & Gupta, 2025), where performance degradation due to metallic mounting surfaces remains a critical challenge. Among these approaches, the Artificial Magnetic Conductor (AMC), a type of metasurfaces, has been utilized to isolate the radiating element from the conductive backing in UHF RFID applications(Kim et al., 2009; Ripin et al., 2020) . By providing an in-phase reflection response around the operating frequency, the AMC layer effectively mitigates destructive image currents induced by the metal surface.

In (Kim et al., 2009), a low-profile UHF passive RFID tag antenna integrated with a compact artificial magnetic conductor (AMC) substrate depicted in Figure 2.24 was proposed for operation on metallic and lossy platforms. A modified rectangular patch-type AMC with offset vias was utilized to shift the high-impedance frequency band downward while reducing the overall planar dimensions of the tag. Experimental

results showed that the proposed design achieved platform-tolerant performance, with measured reading distances ranging from 2.6 m to 4.8 m when mounted on conductive plates and lossy dielectric. The incorporation of the AMC substrate effectively mitigated impedance detuning caused by metallic objects and liquids, enabling a low-profile and stable configuration. Nevertheless, despite the improved on-metal performance, the use of multiple vias increased structural complexity, making the design procedure more tedious and fabrication more challenging, particularly for cost-sensitive passive RFID applications.



(a)



(b)

Figure 2.24 (a) Configuration of The AMC Substrate Layer. (b) Fabricated RFID Tag Antenna Integrated with The AMC Layer at The Bottom.(Kim et al., 2009)

To address these limitations, an alternative approach was presented in (Ripin et al., 2020), where the AMC functionality was embedded directly into a dipolar patch structure. This integration reduced structural complexity while maintaining effective isolation from the metal surface. In (Q. Liu et al., 2022), a platform-tolerant nested-slot RFID tag antenna integrated with a low-profile jigsaw-shaped metasurface was proposed to enhance frequency and radiation stability under different mounting conditions. The metasurface consists of a 4 × 4 array of rippled-edge patch units with

central grounded vias as depicted in Figure 2.25, designed to suppress surface waves within the 902–928 MHz ISM band. Experimental results show that the operating frequency deviation is less than 1 MHz and the measured reading range variation is below 8.7% when mounted on different materials, confirming strong platform tolerance. Nevertheless, despite its excellent frequency and radiation stability, the overall tag dimension of 180 mm × 180 mm remains relatively large, which may restrict its applicability for compact object tagging or size-constrained RFID implementations.

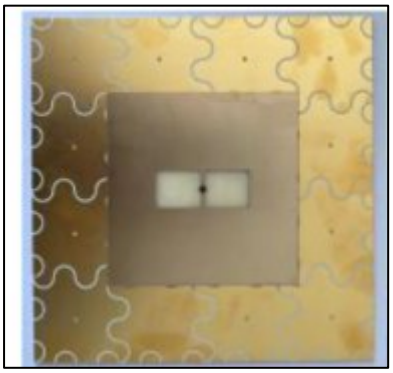


Figure 2.25 Fabricated Nested Slot Tag Antenna Mounted on Jigsaw-Shaped Metasurface.(Q. Liu et al., 2022)

Similarly, a dual-band UHF RFID tag integrating a dipole radiator with a metasurface was reported in(Hien Doan et al., 2019), designed to operate within both the North American (902–928 MHz) and Indian (840–845 MHz) frequency bands. The incorporation of the metasurface enabled unidirectional radiation characteristics and enhanced read-range performance. Experimental results demonstrated maximum readable distances of 6 m in the FCC band (902–928 MHz) and 4.4 m in the Indian band (840–845 MHz). However, despite its improved radiation performance, the proposed structure possesses a relatively large footprint and high profile (190 mm × 190 mm × 15.8 mm), which limits its practicality for compact and low-profile RFID tagging applications, particularly for small or size-constrained objects.

Overall, metasurface-assisted RFID tag antennas have demonstrated significant potential for improving metal tolerance, stabilizing radiation characteristics, and enhancing realized gain. Existing studies employ Artificial Magnetic Conductor (AMC) and Electromagnetic Band Gap (EBG) structures to suppress surface waves and mitigate impedance detuning caused by metallic environments. In contrast, Huygens' metasurfaces have been investigated primarily for microwave and millimeter-wave

applications, such as 5G communications, where the shorter wavelength enables compact meta-element implementation and high-gain beam manipulation.

Their application to UHF RFID systems operating below 1 GHz has received little attention because the considerably longer wavelength results in much larger meta-elements, making compact antenna integration significantly more challenging. Consequently, a clear research gap exists in developing compact Huygens-based meta-elements that can be effectively integrated with UHF on-metal RFID tag antennas to simultaneously enhance radiation performance, maintain stable impedance matching, and preserve a compact antenna profile. Therefore, this research investigates the integration of a Huygens' Meta Element (HME) with a compact UHF RFID tag antenna to overcome these challenges and improve antenna performance in metallic deployment environments.

2.4 Summary

This chapter has presented a comprehensive overview of RFID technology, with particular emphasis on UHF passive RFID systems and tag antenna design considerations for metallic environments. The fundamental operating principles of RFID technology were first discussed, including system components, operating frequency bands, and typical application scenarios. These discussions established the theoretical foundation necessary for understanding the challenges associated with practical RFID deployment.

A detailed review of existing UHF RFID tag antenna designs was subsequently conducted, covering both conventional tag antennas and metal-mountable configurations. Various miniaturization techniques and impedance-matching strategies reported in the literature were critically analyzed, highlighting the inherent trade-offs among size reduction, bandwidth, radiation efficiency, structural complexity, and fabrication cost.

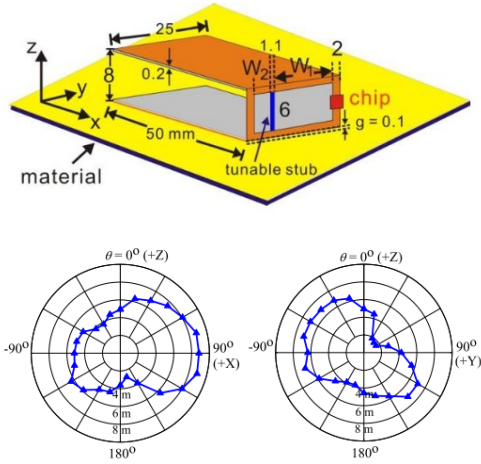
The chapter then examined the integration of metasurface and metamaterial concepts into RFID tag antenna design. Approaches based on Artificial Magnetic Conductors (AMC) and other metasurface structures were evaluated in terms of their effectiveness in suppressing surface waves, mitigating impedance detuning, improving metal tolerance, and enhancing radiation performance. Although these techniques have demonstrated measurable performance improvements, many reported designs remain

constrained by bulky dimensions, increased profile thickness, narrow operational bandwidth, and higher fabrication complexity.

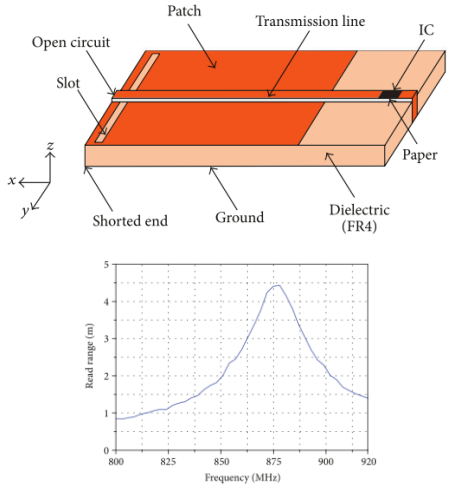
In addition, recent developments in Huygens metasurface concepts were reviewed. Unlike conventional AMC structures that primarily rely on reflection-phase control, Huygens metasurface utilize balanced electric and magnetic responses to enable improved radiation shaping and wavefront control. However, the application of Huygens metasurface principles to compact UHF on-metal RFID tag antennas has not been comprehensively explored.

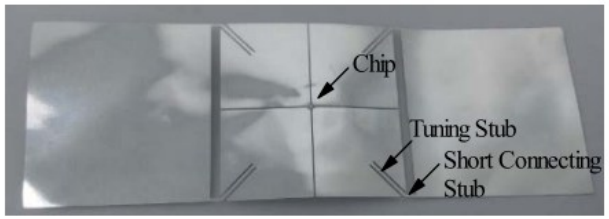
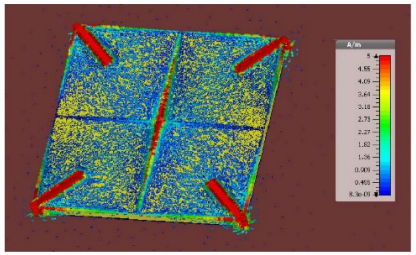
Based on the critical analysis presented in this chapter, a clear research gap has been identified. Therefore, there remains a need to develop a compact, low-profile, and structurally efficient on-metal UHF RFID tag antenna that incorporates Huygens' metasurface principles to achieve stable impedance matching, enhanced realized gain, improved radiation efficiency, and extended read range without compromising antenna compactness. This identified gap provides the primary motivation for the design methodology and proposed antenna configurations presented in the subsequent chapters. A summary of the identified research gaps in on-metal UHF RFID tag antenna design is presented in Table 2.1.

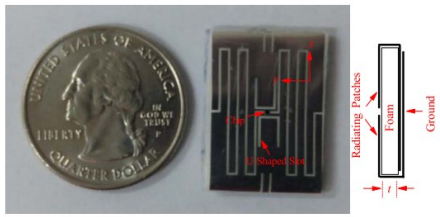
Table 2.1
Summary Of Reported On-Metal UHF RFID Tag Antenna Designs Highlighting the Research Gaps.

Categories	Technique/ Description	References	Comments
UHF RFID Tag Antenna Designs	Stub-matching techniques 	An Inverted-F Antenna for RFID Tag Mounted on a Full Container of Liquid (Tan et al., 2020)	Dimension: 50 × 25 × 8 mm^3 Read range: 5.7 m The antenna achieved conjugate impedance matching at the desired operating frequency through stub tuning. However, the reported read range of 5.7 m was evaluated only when the tag was mounted on a water container, and no measurement was conducted on a metallic plate. Therefore, the on-metal performance stability and impedance robustness of the design remain unverified.

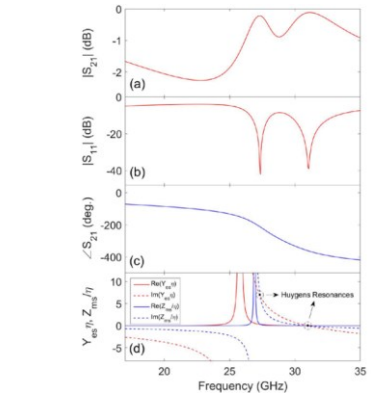
On-metal UHF RFID Tag Antenna Designs	Ground plane inclusion	Small Size and Low-Cost UHF RFID Tag Antenna Mountable on Metallic Objects (López-Soriano & Parrón, 2015)	Dimension: 33.5 × 30 × 3.1 mm³ Read range: 5 m The adverse effect of the metallic surface was mitigated by incorporating a ground plane, enabling a measured read range of approximately 5 m. The antenna exhibits a compact overall footprint of 33.5 × 30 × 3.1 mm³. Nevertheless, this work further illustrates the trade-off between miniaturization and radiation efficiency in on-metal RFID tag antennas, miniaturization inherently limits radiation efficiency and detection range.
			Dimension: 30 × 30 × 1.6 mm³

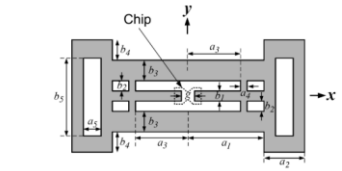
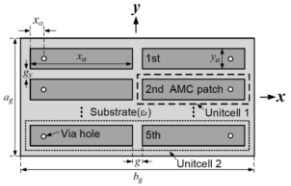
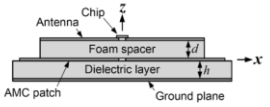
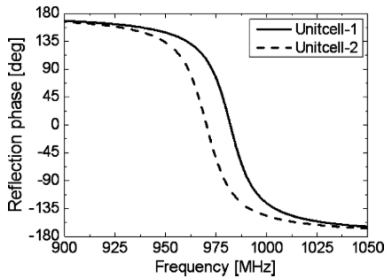


Folded dipolar patch  	Compact Orientation Insensitive Dipolar Patch for Metal-Mountable UHF RFID Tag Design (F.-L. Bong et al., 2018)	Read range: 2 - 3.5 m The folded dipolar patch achieved a highly compact footprint of 30 mm × 30 mm × 1.6 mm and demonstrated omnidirectional detection in the boresight direction. However, despite its reduced size, the measured detection range remains limited to approximately 2.9–3.5 m when mounted on metal and 2–2.7 m when placed on dielectric surfaces. Furthermore, the incorporation of four tuning stubs as the impedance matching mechanism complicates the tuning process.	

Etching slot 	Miniaturized dipolar patch antenna with narrow meandered slot line for UHF tag (F. L. Bong et al., 2017)	Dimension: 23 × 16 × 1.6 mm³ Read range: 4 m The tag, with an electrical footprint of 0.0702λ × 0.0488λ × 0.0049λ, is specifically designed for on-metal applications. A narrow-meandered slot is etched into the radiating patch to reduce the resonant frequency and achieve size miniaturization. However, under a transmitted power of 4 W EIRP, the measured read range remains limited to approximately 4 m. This indicates that although the meandered slot effectively reduces the antenna size, the radiation characteristics are consequently degraded.

Metasurface-Based Concepts in UHF RFID Tag Antenna Designs	Huygens' metasurface	Broadband Double-Layered Huygens' Metasurface Lens Antenna for 5G Millimeter-Wave Systems (Xue et al., 2020)	The Huygens' unit cell demonstrates an excellent transmission-mode response, providing a phase coverage exceeding 400° with a transmission amplitude better than –2.3 dB. Based on this unit cell, a metasurface lens was designed and achieved a high gain performance of 30.7 dBi. These results indicate the strong potential of Huygens-based structures for gain enhancement. However, the integration of Huygens' meta-elements with passive UHF RFID tag antennas has not yet been explored.



Integration metasurface with tag antenna	 (a) Top view of the antenna  (b) Top view of the AMC substrate  (c) Cut view of the RFID tag antenna 	Low-Profile RFID Tag Antenna Using Compact AMC Substrate for Metallic Objects (Kim et al., 2009)	Dimension: 34 × 67 × 3.5 mm³ Read range: 4.8 m The integration of an Artificial Magnetic Conductor (AMC) into the tag antenna successfully mitigates the adverse effects of the backing metal. The incorporation of the AMC substrate effectively reduces impedance detuning caused by metallic objects and nearby liquids. However, the inclusion of vias increases structural complexity, complicates the fabrication process, and consequently raises production costs.

CHAPTER 3
RESEARCH METHODOLOGY

3.1 Introduction

Chapter 3 presents the research methodology adopted for the design, fabrication, and experimental validation of the two proposed UHF RFID tag antennas for on-metal applications. The methodology begins with the development of the first antenna, namely the folded RFID tag antenna with embedded inductance, in which an embedded inductive tuning mechanism is introduced to achieve a compact antenna structure while ensuring effective impedance matching with the RFID microchip. The study subsequently progresses to the second antenna; a dipolar patch RFID tag antenna integrated with a Huygens' Meta-Element (HME). This design investigates the feasibility of integrating HME into RFID tag antennas to enhance radiation performance, in terms of realized gain and read range, while maintaining stable impedance matching for reliable on-metal operation. Throughout the study, the methodology integrates electromagnetic modelling, design optimization, fabrication, and experimental validation, and is illustrated through a structured research flowchart that outlines the sequential stages of the research.

Subsection 3.3 defines the antenna design requirements and key performance parameters, including impedance matching, read range, and power transfer coefficient (τ), which serve as the basis for the subsequent design and optimization stages. The RFID design process, which includes the development of the dipolar patch and the characterization of the RFID microchip, is then described, followed by a detailed explanation of the working principles of the Huygens' metasurface (HMS) concept.

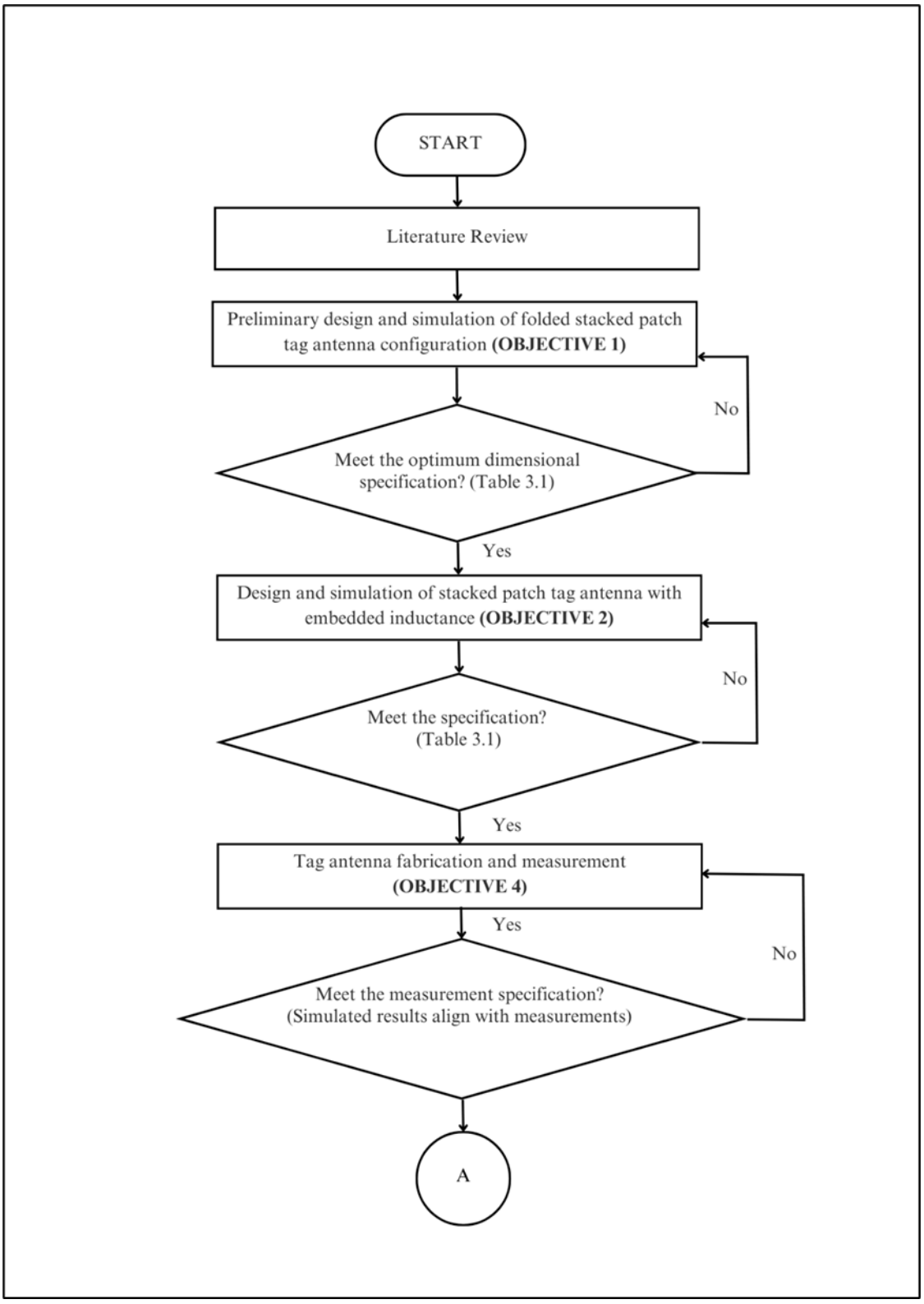
The chapter also describes the fabrication of the antenna prototype using a chemical etching process and its experimental validation using the Voyantic Tagformance Pro measurement system. Overall, the methodology provides a comprehensive framework of simulation, fabrication, and measurement to ensure that the proposed antenna design is both theoretically verified and experimentally validated under a practical metallic environment.

3.2 Research Methodology

Figure 3.1 illustrates the research methodology adopted for the design and development of two novel passive UHF RFID tag antennas. The workflow begins with a comprehensive literature review to establish a foundation in antenna miniaturization, gain enhancement techniques, and passive RFID technology. This is followed by the preliminary design and simulation of a folded stacked patch tag antenna configuration, which is evaluated against the optimum dimensional specifications outlined in Table 3.1. Upon meeting these criteria, the design is further refined by embedding an inductive element to enhance antenna performance. The simulated design is then validated through fabrication and experimental measurement. Any discrepancies between simulated and measured results are addressed through iterative optimization until satisfactory agreement is obtained.

The second phase of the methodology focuses on improving radiation characteristics through the integration of a Huygens' meta element (HME). This begins with the design and simulation of a Huygens' unit cell, which must satisfy the theoretical condition defined in Equation 3.1. Once validated, the HME is integrated into the dipolar tag antenna structure. The integrated design is then evaluated according to the performance specifications summarized in Table 3.2. After achieving optimum simulation performance, the antenna prototype is fabricated and subjected to experimental testing. The measured results are then compared with simulation data to validate accuracy. The research concludes with a comprehensive data analysis, followed by detailed report writing and documentation to ensure that both antenna designs are thoroughly validated for practical implementation in RFID systems.

Throughout the research methodology, sustainability, fabrication scalability, and ethical considerations were incorporated to support the practical implementation of the RFID tag antennas. Both antenna designs employ passive RFID technology, which eliminates the need for batteries and contributes to reduced electronic waste and maintenance requirements. Furthermore, the proposed antenna structures are developed using commercially available substrate materials and conventional PCB fabrication techniques, facilitating cost-effective and scalable manufacturing for practical deployment. As this research involves only electromagnetic simulations and laboratory-based antenna measurements without human or animal participants, ethical approval was not required.


START
Literature Review
Preliminary design and simulation of folded stacked patch tag antenna configuration (OBJECTIVE 1)
No
Meet the optimum dimensional specification? (Table 3.1)
Yes
Design and simulation of stacked patch tag antenna with embedded inductance (OBJECTIVE 2)
No
Meet the specification? (Table 3.1)
Yes
Tag antenna fabrication and measurement (OBJECTIVE 4)
Yes
No
Meet the measurement specification? (Simulated results align with measurements)
A

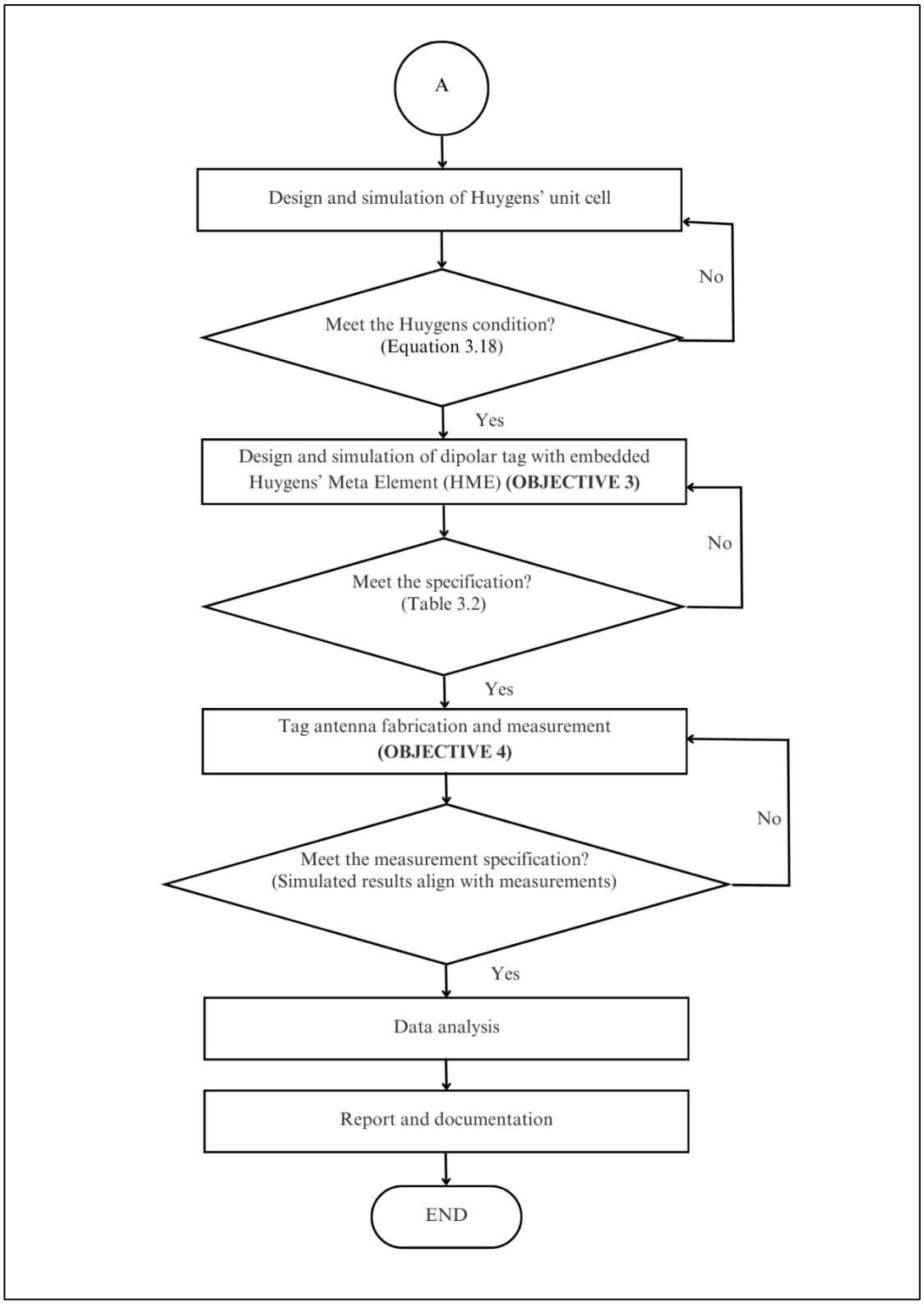


Figure 3.1 Flowchart of the Research Methodology.

3.3 RFID Antenna Design Requirements and Key Technical Parameters

This section outlines the design requirements and key performance parameters considered in the development of the proposed UHF RFID tag antenna. It discusses the RFID design specifications and presents the formulas used to determine the read range and power transfer coefficient (τ).

3.3.1 RFID Design Specification

Table 3.1 and Table 3.2 summarize the key design specifications for the two passive UHF RFID tag antenna structures developed in this research. Table 3.1 outlines the design targets for the folded RFID tag antenna with embedded inductance, operating within the US RFID frequency band (902–928 MHz). The antenna is designed to achieve a return loss (S_{11}) below –10 dB to ensure proper impedance matching and a power transfer coefficient greater than 0.8. The antenna impedance is designed to be nearly conjugate to the NXP UCODE 8 chip impedance, specifically 13 + j191 Ω, to minimize impedance mismatch. A minimum read range of 6 meters is targeted to meet practical deployment requirements. The antenna size is constrained to be less than 0.153λ × 0.153λ × 0.012λ, ensuring a compact footprint. The structure is fabricated on a polyimide substrate chosen for its flexibility and suitability for conformal surface applications.

Table 3.2 outlines the design specifications for the dipolar patch tag antenna integrated with a Huygens' Meta Element (HME), aimed at enhancing the antenna's radiation performance. This design operates within the European RFID band (865–868 MHz). The performance targets remain consistent with the previous design, with a return loss of less than –10 dB, a power transfer coefficient exceeding 0.8, and a minimum read range of 6 meters. The impedance matching goals remain at 10 + j191 Ω. Integration of the HME provides improved radiation shaping while maintaining a compact antenna footprint of less than 0.159λ × 0.159λ × 0.008λ. The antenna is implemented on a Rogers RT-6010 substrate, selected for its high dielectric constant and low-loss characteristics, which support miniaturization.

For both proposed antenna designs, a power transfer coefficient (τ) greater than 0.8 is specified to ensure efficient power transfer from the antenna to the RFID microchip through proper conjugate impedance matching. A high-power transfer coefficient minimizes impedance mismatch losses, thereby maximizing the RF energy

delivered to the passive microchip for reliable activation. In addition to efficient impedance matching, the antennas are designed to achieve high realized gain and radiation efficiency to enhance their overall radiation performance. These parameters play a significant role in determining the performance of passive UHF RFID systems, as higher realized gain and radiation efficiency improve the radiated power and consequently extend the achievable read range. Accordingly, both proposed RFID tag antennas are designed to achieve a minimum read range of more than 6 m under standard UHF RFID operating conditions. These design specifications serve as key performance benchmarks throughout the simulation, fabrication, and experimental validation stages of this research. The read range performance of the fabricated tag antennas is experimentally validated in an anechoic chamber using the Voyantic Tagformance Pro measurement system that will be discussed in detail at Section 3.7.

Table 3.1
Design Specifications for Folded RFID Tag Antenna with Embedded Inductance.

Parameter	Target Specification
Operating Frequency	902 – 928 MHz (US RFID band)
Return Loss (S_{11})	≤ –10 dB
Power Transfer Coefficient	≥ 0.8
Read Range	≥ 6 m
Microchip	NXP UCODE 8
Antenna Impedance, $Z_a(\Omega)$	Nearly conjugate to chip impedance, 13 + j191 Ω
Antenna Size (L × W × H)	≤ 0.15λ × 0.15λ × 0.01λ
Substrate	Polyimide (ε_r = 3.3, tan δ = 0.0027)

Table 3.2
Design Specifications for Dipolar Patch Tag with Huygens' Meta Element

Parameter	Target Specification
Operating Frequency	865 – 868 MHz (LEU RFID band)
Return Loss (S_{11})	≤ –10 dB
Power Transfer Coefficient	≥ 0.8
Read Range	≥ 6 m
Microchip	NXP UCODE 9

Antenna Impedance, $Z_a(\Omega)$	Nearly conjugate to chip impedance, 10 + j191 Ω
Antenna Size (L × W × H)	≤ 0.15λ × 0.15λ × 0.01λ
Substrate	Rogers RT-6010 (ε_r = 10.6, tan δ = 0.0023)

3.3.2 Read range

The read range (R_{max}) RFID tag antenna refers to the maximum distance at which the tag can be activated and correctly detected by a reader. This parameter is critical in determining the effectiveness of RFID systems, especially in logistics, retail, and asset tracking applications.

The read range is commonly calculated using the Friis free-space transmission equation, adapted for passive RFID systems. The basic form of the equation is (Murugesh, Akbar, & Ghazali, 2026):

$$R_{max} = \frac{\lambda}{4}\sqrt{\frac{P_t G_t G_{tag} \tau}{P_r}} \tag{3.1}$$

Where

λ = Wavelength of the operating frequency

P_t = Transmit power of the reader

G_t = Gain of the reader antenna

G_{tag} = Gain of the tag antenna

τ = Power transfer coefficient

P_r = Threshold power

The $G_{tag}.\tau$ represents the realized gain G_r of the tag antenna. During the measurement, the received power P_r is equal to the chip's sensitivity, denoted as P_i which can be obtained from the chip's datasheet. Therefore, the read range equation simplifies to equation (3.2)(Erman et al., 2026).

$$R_{max} = \frac{\lambda}{4}\sqrt{\frac{P_t G_t G_r}{P_i}} \tag{3.2}$$

To further estimate the RFID tag's read range, the Equivalent Isotropically Radiated Power (EIRP) can be used, which simplifies the calculation process. The chip's sensitivity, P_i and the EIRP can also be expressed and defined as in equations (3.3) and (3.4), respectively(Ng et al., 2025) .

$$P_i = P_{tag}\, G_r \tag{3.3}$$

$$P_{EIRP} = P_t G_t \tag{3.4}$$

By setting a fixed maximum allowable EIRP, typically regulated by authorities such as MCMC or FCC and using the tag's sensitivity P_{tag}, obtained through measurement, the maximum activation distance R_{max} can be calculated using equation (3.5).

$$R_{max} = \frac{\lambda}{4}\sqrt{\frac{P_{EIRP}}{P_{tag}}} \tag{3.5}$$

3.3.3 Power Transfer Coefficient (τ)

In RFID antenna design, impedance matching between the antenna and the RFID chip is critical for maximizing power transfer. The power transfer coefficient, denoted as τ, quantifies how efficiently power is delivered from the antenna to the chip. It is mathematically defined by equation (3.6)(Murugesh, Akbar, Ghazali, et al., 2026).

$$\tau = \frac{4R_c R_a}{|Z_c + Z_a|^2} \tag{3.6}$$

τ = Maximum power transfer

R_c = Resistive part of the chip

R_a = Resistive part of the antenna

Z_c = Chip impedance ($R_c + jX_c$)

Z_a = Antenna impedance ($R_a - jX_a$)

A τ value close to 1 indicates maximum power transfer, which occurs when the antenna impedance is the complex conjugate of the chip impedance, i.e., $Z_a = Z_c$. Under this condition, maximum power is transferred from the antenna to the microchip,

resulting in improved tag sensitivity and read range. Conversely, impedance mismatch reduces the value of τ, thereby decreasing the power delivered to the microchip and degrading the overall RFID tag performance.

Therefore, achieving near-perfect conjugate matching ($\tau \approx 1$) is established as one of the primary design objectives of the proposed low frequency RFID tag antenna. Throughout the antenna design process, the antenna geometry is systematically optimized to maximize the power transfer coefficient while simultaneously satisfying the requirements of compactness, operating frequency, and radiation performance. The effectiveness of this design methodology is subsequently validated through the simulation and experimental results presented in Chapter 4.

3.4 RFID Tag Antenna Design

This section describes the overall RFID tag antenna design and its key components. It includes the development of a dipolar patch structure, a fundamental RFID tag antenna structure, the characterization of the RFID microchip, and the theoretical concept of the Huygens' metasurface (HMS).

3.4.1 Dipolar Patch Antenna

Dipolar patch antenna is essentially a planar adaptation of the conventional half-wavelength dipole, optimized for compact and integrated systems such as UHF RFID tags. As shown in Figure 3.2, dipole antenna is a wire-based, center-fed structure that radiates effectively through two symmetrical metal arms and typically resonates at half the free-space wavelength. It operates without the need for a ground plane and exhibits a relatively simple design. The resonant length of a conventional dipole is given by the following expression (Warren L. Stutzman, 2012) :

$$L_{dipole} = \frac{\lambda}{2} = \frac{c}{2f} \tag{3.7}$$

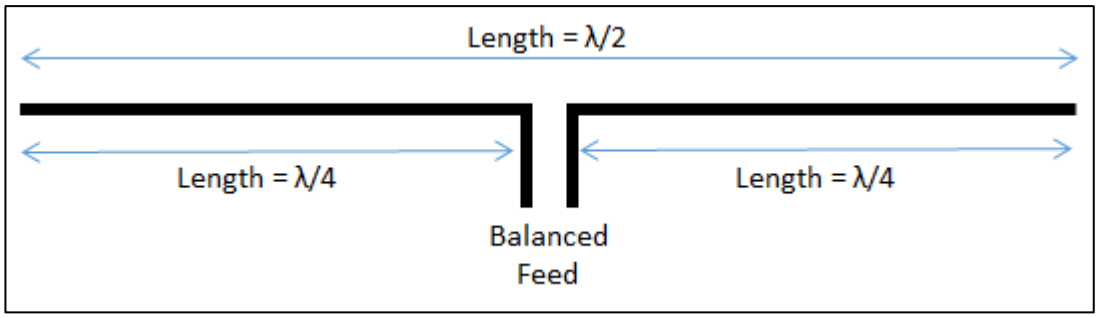


Figure 3.2 Basic Dipole Antenna.

In contrast, a dipolar patch antenna is a planar and printed version of the dipole, designed to emulate the current distribution of a half-wavelength dipole while enabling seamless integration into low-profile and compact platforms. Unlike the wire-based dipole, the dipolar patch is fabricated on a dielectric substrate and typically incorporates a ground plane beneath the radiating element. This configuration supports printed-circuit implementation. To achieve resonance at a desired frequency, f_r the effective length or width of the dipolar patch, as shown in Figure 3.3, can be approximated using the following expression, where ε_r is the dielectric constant of the substrate material(Warren L. Stutzman, 2012):

$$\mathrm{L} = \mathrm{W} = \frac{c}{2f_r\sqrt{\varepsilon_r}} = \frac{\lambda}{2\sqrt{\varepsilon_r}} \tag{3.8}$$

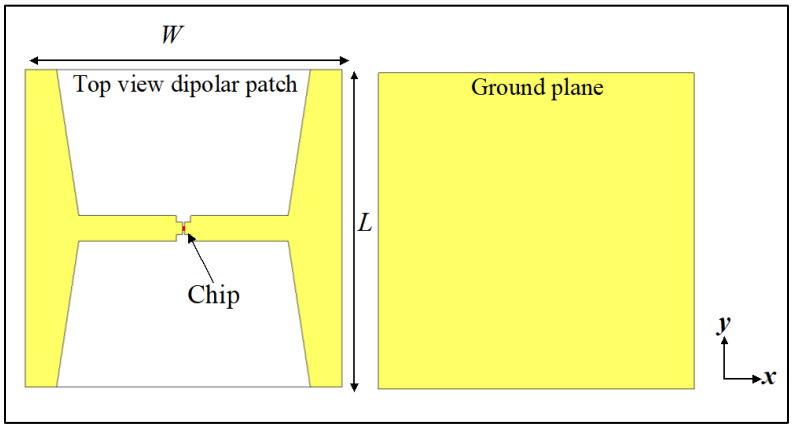


Figure 3.3 Configuration of The Dipolar Patch.

Compared to the classical dipole, the dipolar patch antenna exhibits a significantly shorter physical length due to its substrate-supported structure and planar configuration. For instance, at a resonant frequency of 867 MHz, a conventional half-wave dipole would require a total length of approximately 172 mm. In contrast, a dipolar patch antenna designed on a dielectric substrate may only measure around 53

mm. This size reduction is attributed to the slower wave propagation in the substrate and the influence of fringing fields at the patch edges.

In microstrip-based structures, the electromagnetic wave is not confined entirely within the substrate but also extends into the air above, causing the wave to experience an intermediate dielectric environment. As a result, the resonant length of the dipolar patch is more accurately estimated by incorporating the effective dielectric constant, ε_{reff} together with a fringing field correction term ΔL, as shown below:

$$\mathrm{L} = \frac{c}{2f_r\sqrt{\varepsilon_{reff}}} - 2\Delta\mathrm{L} \tag{3.9}$$

Where ε_{reff} is the effective dielectric constant, and ΔL represents the length extension due to the fringing effects at the edges of the patch. The calculated patch dimensions will undergo further optimization during the simulation phase of the antenna design process.

Table 3.3 presents the calculated dimensions of the dipolar patch antenna, specifically the length (*L*) and width (*W*), designed using Rogers RT-6010 substrate material with a dielectric constant of ε_r=10.6 and a low loss tangent of $tan\delta$ =0.0023. The substrate thickness and copper thickness are 0.635 mm and 0.035 mm, respectively. The initial dimensions were calculated based on the target operating frequency of 867 MHz. These theoretical values were used as the starting parameters in CST Microwave Studio prior to the parametric optimization process. A comprehensive discussion on the dipolar patch antenna, including its structural configuration, optimization procedure, and performance characteristics, is presented in Section 5.3.

Table 3.3
Calculated Dimension of the Dipolar Patch Antenna

Parameter	Dimension (mm)
L	53
W	53
h_c	0.635
h_s	0.035

In this work, a dipolar patch antenna is employed as the baseline structure for the UHF RFID tag to systematically investigate the effect of integrating Huygens Meta-Elements (HME) on tag performance, which will be discussed in detail in Chapter 5.

Based on the review of published works, the application of Huygens-based structures in passive UHF RFID tag antennas has not been previously reported in the literature. The dipolar patch configuration was selected due to its structural simplicity, geometrical symmetry, and relatively straightforward impedance characteristics, providing a stable and well-understood platform for rigorously evaluating the electromagnetic impact of HME integration on radiation behavior, impedance matching stability, gain enhancement, and overall read range performance.

3.4.2 RFID Microchip

Two different NXP UHF RFID microchips were employed in this research work, namely UCODE 8 and UCODE 9, to validate the antenna design across different chip generations. The UCODE 8 provides a read sensitivity of –22.9 dBm and a write sensitivity of –18 dBm, with a typical input impedance of approximately 13 – j191 Ω(NXP Semiconductors, 2021). Read sensitivity refers to the minimum RF power required at the chip input for the tag to be activated and successfully backscatter a response to the reader, while write sensitivity indicates the minimum RF power necessary for the chip to store data into its non-volatile memory. The UCODE 8 is widely adopted in applications such as retail, supply chain management, shipping services, and luggage tracking due to its robust performance.

By comparison, the UCODE 9 offers improved performance with a higher read sensitivity of –24 dBm and an enhanced write sensitivity of –22 dBm, while presenting a slightly lower impedance of about 10 – j191 Ω (NXP Semiconductors, 2025). This newer generation chip is optimized for dense tag environments, featuring dynamic backscatters or improved communication efficiency. It is particularly suited for fashion retail, baggage tracking, and smart logistics, where high inventory speed and reliability are critical. A comparison between the NXP UHF RFID microchips is summarized in Table 3.3, while the detailed RF interface characteristics are provided in Appendix 1 and Appendix 2.

Table 3.4
Comparison of NXP UCODE 8 and UCODE 9 RFID Microchips

	UCODE 8	UCODE 9
Operating frequency	840 – 960 MHz	840 – 960 MHz
Impedance	~ 13 – j191 Ω	~ 10 – j191 Ω
Read sensitivity	-22.9 dBm	-24 dBm
Write sensitivity	-17.8 dBm	-22 dBm

3.4.3 Huygens' Metasurface

Huygens' principle, proposed by Christiaan Huygens, states that "each point on a primary wavefront can be considered a new source of a secondary spherical wave, and a secondary wavefront can be constructed as the envelope of these waves." Figure 3.4 illustrates this concept and its analogy to antenna apertures.

In Figure 3.4(a), each point on the incident wavefront (blue line) acts as a secondary source that radiates a small spherical wave. The resulting wavefront (red line) is formed as the smooth envelope of these contributions. Similarly, in Figure 3.4(b), the same principle is applied to antennas, where each point on the aperture behaves as a secondary source. The combined effect produces a strong forward-directed main beam, while partial cancellations in other directions give rise to weaker sidelobes.

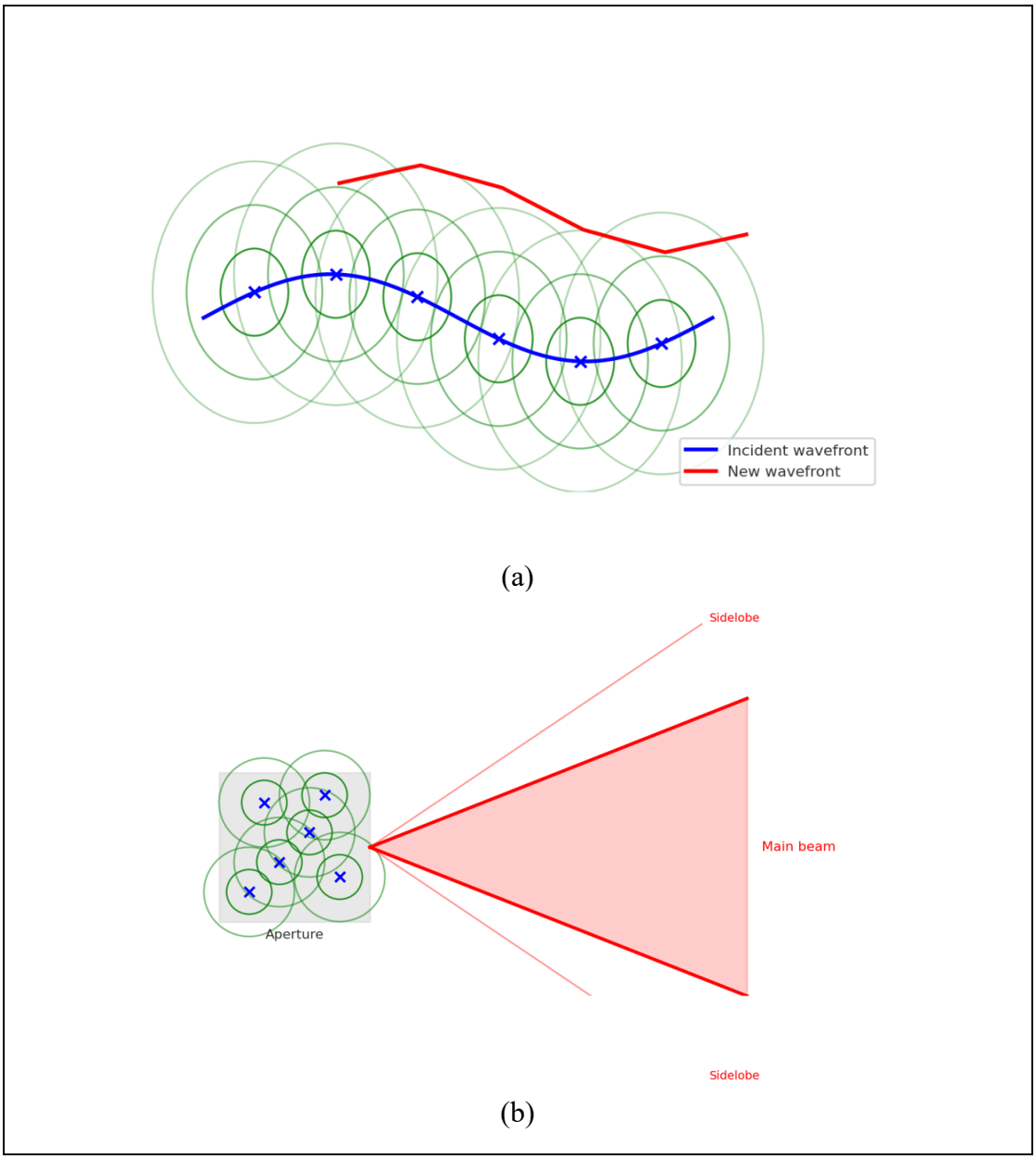


Figure 3.4 (a) Illustration of Huygens' Principle And (b) Its Interpretation in The Antenna Aperture Analogy.

The relation of Huygens' theory to the dipolar patch with a Huygens' Meta Element (HME) can be summarized as follows:

1. The radiated signal of the dipolar patch antenna generates the incident wavefront.
2. Each point of this radiated field behaves as a secondary source when interacting with the HME.

3. As the wave propagates through the HME, these secondary sources are transformed and recombined to form a new wavefront in accordance with Huygens' principle.
4. The newly constructed wavefront produces a directive main beam, while sidelobes are suppressed due to the balanced electric and magnetic responses of the HME.

The theoretical foundation of the Huygens' surface can also be understood through the equivalence principle. A typical Huygens' surface consists of three layers, comprising a dielectric substrate sandwiched between two metallic sheets. As illustrated in Figure 3.5, the surface separates two regions, Region 1 and Region 2, with tangential electric (E_1, E_2) and magnetic (H_1, H_2) field components defined on either side. The surface impedance excites equivalent currents (J_s ,M_s) , that account for the discontinuity of tangential fields across the metasurface, in accordance with the boundary conditions expressed in Equation (3.10) and (3.11)(Xue et al., 2022).

$$J_s = \hat{n} \times (H_2 - H_1)\ ;\ J_s = Y_{es} \times E_{av} \tag{3.10}$$

$$M_s = -\hat{n} \times (E_2 - E_1)\ ;\ M_s = Z_{ms} \times H_{av} \tag{3.11}$$

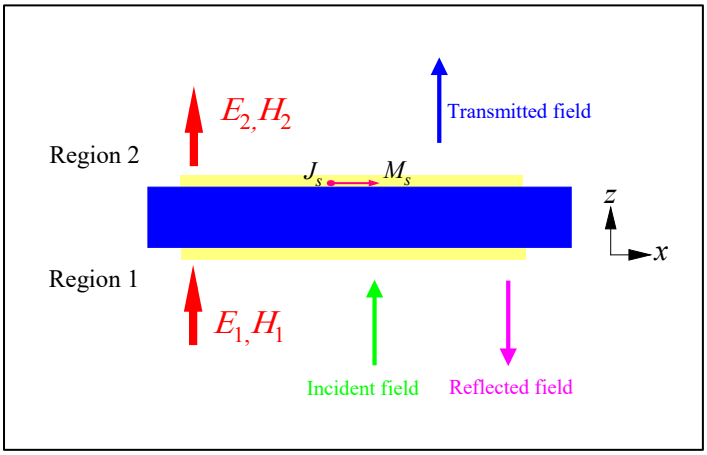


Figure 3.5 Side-View Configuration of The Proposed Huygens' Surface.

By applying generalized sheet transition conditions in equations (3.10) and (3.11), the incident wave is assumed to be linearly polarized. The fields on both sides of the surface can then be decomposed into incident fields (E_i , H_i), reflected fields (E_r , H_r), transmitted fields (E_t , H_t). Accordingly, the field relations at Region 1 and Region 2 are expressed as(Peng et al., 2020):

$$E_1 = E_i + E_r \tag{3.12}$$

$$H_1 = H_i - H_r \tag{3.13}$$

$$E_2 = E_t \tag{3.14}$$

$$H_2 = H_t \tag{3.15}$$

By combining equations (3.10) - (3.15), the electric surface admittance, Y_{es} and magnetic surface impedance, Z_{ms} can be realized. In practice, these parameters are extracted from the reflection ($S_{11} = R$) and transmission ($S_{21} = T$) coefficients, yielding the normalized forms(Zohre Pourgholamhossein, 2017):

$$Y_{es}\eta = \frac{2\,(1 - T - R)}{(1 + T + R)} \tag{3.16}$$

$$\frac{Z_{ms}}{\eta} = \frac{2\,(1 - T + R)}{(1 + T - R)} \tag{3.17}$$

where, $\eta = \sqrt{\mu_o/\varepsilon_o}$ is the intrinsic impedance of free space, μ_o and ε_o denoting permittivity and permeability in free space, respectively.

Once the normalized electric surface admittance and magnetic surface impedance are obtained, the reflectionless Huygens' surface condition can be verified. For a reflectionless Huygens' surface(Pourgholamhossein et al., 2022):

$$Y_{es}\eta = \frac{Z_{ms}}{\eta} \tag{3.18}$$

In this case, the real parts of both parameters should be small and close to zero, indicating low-loss performance of the unit cell. Meanwhile, the imaginary parts of the admittance and impedance should be equal, ensuring balanced electric and magnetic responses. Correspondingly, at the Huygens' resonance frequency, the reflection coefficient (S_{11}) approaches zero, while the transmission coefficient (S_{21}) approaches unity.

In this research work, the Huygens' Meta Element is demonstrated in the form of as a planar meta element printed on a thin dielectric substrate and positioned top-loaded onto dipolar patch radiator. In this configuration, the Huygens' does not function as a reflective ground plane but operates in transmission mode to shape and enhance the radiation profile of the underlying tag antenna. By strategically positioning the Huygens' metasurface substrate above the radiating element, the electromagnetic fields

are redistributed to improve broadside gain without increasing the antenna footprint or introducing complex structures. The detailed design methodology, parametric optimization, and performance validation of the HME-integrated RFID tag antenna will be presented in Chapter 5.

3.5 Simulation of RFID Tag Antenna with Integrated Microchip

The RFID tag antenna was designed and analyzed using CST Microwave Studio, after all design specifications and performance requirements were clearly defined. CST was selected due to its robust electromagnetic solver capabilities, user-friendly interface, and reliable simulation performance for high-frequency applications. The software provides accurate and efficient electromagnetic analysis for various microwave and RF components, including antennas, filters, transmission lines, couplers, and resonators.

During the design process, the antenna geometry was systematically optimized through parametric simulations to achieve the desired impedance matching, radiation characteristics, and overall tag performance. Iterative refinement was conducted until the optimum geometry was obtained.

The simulation results extracted from CST include the reflection coefficient (S_{11}), power transmission coefficient, input impedance, realized gain, radiation pattern, and surface current distribution. These parameters were carefully analysed to evaluate the antenna's impedance matching with the RFID chip and its radiation efficiency, ensuring that the design meets the required operational criteria for UHF RFID applications.

CST Microwave Studio offers several electromagnetic simulation techniques, including the Time Domain Solver, Frequency Domain Solver, Asymptotic Solver, Integral Equation Solver, and Eigenmode Solver. The selection of the solver depends on the application requirements, operating frequency range, computational resources, and desired accuracy. Each solver also supports specific meshing techniques that are compatible with its numerical formulation.

In this research, the Frequency Domain Solver was employed as it is based on the Finite Element Method (FEM), which provides high numerical accuracy for narrowband antenna analysis and complex geometrical configurations. The FEM formulation utilizes a tetrahedral mesh, enabling precise modelling of fine structural features such as inclined slots, thin dielectric substrates, and detailed impedance

matching elements. This characteristic makes it highly suitable for the analysis and optimization of the proposed UHF passive RFID tag antennas.

CST Microwave Studio was used to construct the antenna structure through its graphical modelling environment. After the geometry was completed and material properties were assigned, the meshing process was performed prior to simulation. The mesh density plays a critical role in determining simulation accuracy. Generally, increasing the number of mesh elements improves field resolution and numerical precision, thereby reducing discrepancies between simulated and measured results. However, higher mesh density also increases computational time and memory requirements.

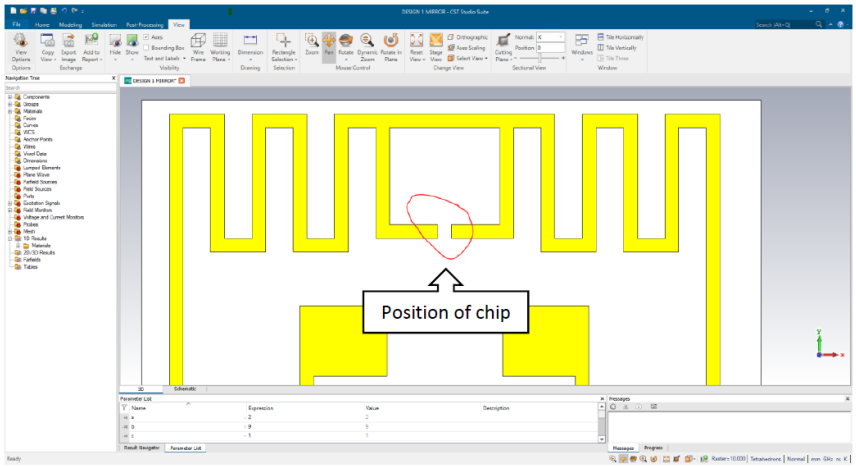
An adaptive mesh refinement technique was applied, where CST automatically refines the tetrahedral mesh iteratively until the S-parameter convergence criteria were satisfied. For the folded-patch tag antenna presented in Chapter 4, the final mesh consisted of 189,592 tetrahedral elements. In Chapter 5, the dipolar patch RFID tag antenna with HME required 208,489 tetrahedral elements, while the simulation of the Huygens unit cell comprised 115,898 tetrahedral elements. These mesh settings ensured an optimal balance between simulation accuracy and computational efficiency.

The next stage involves the simulation of the RFID tag antenna integrated with the microchip. After the antenna structure was fully modelled, the chip position was determined at the designated feeding location. A small gap was then created at the feed point to represent the chip connection, as illustrated in Figure 3.6(a). The gap dimensions were defined according to the physical size and pad configuration of the selected RFID microchip.

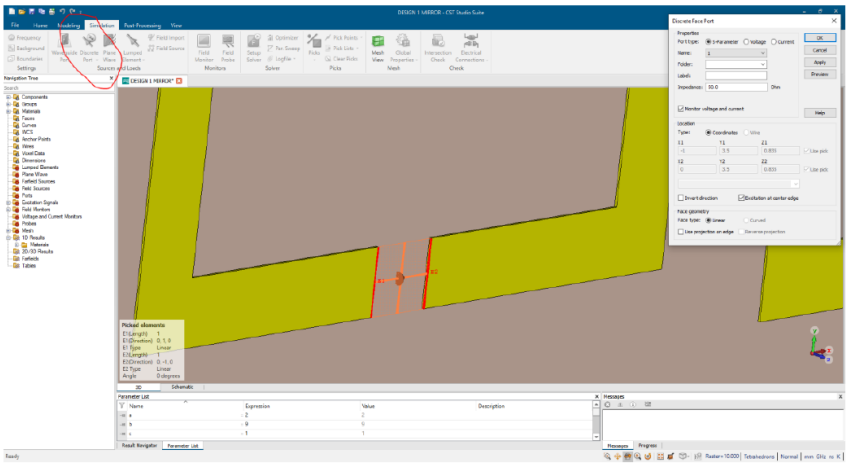
A discrete port was subsequently assigned across the gap to model the chip excitation. In the Frequency Domain Solver, this discrete port represents the lumped connection between the antenna terminals and the RFID chip as shown in Figure 3.6(b).After defining the port in the 3D model, the design was linked to the schematic window, where the external port was connected to the antenna structure for proper circuit integration as shown in Figure 3.6(c).

In the Figure 3.6(d), the reference impedance of the discrete port was then set to match the complex impedance of the RFID chip to ensure accurate power transfer analysis. This step is crucial for evaluating impedance matching and maximizing the power transmission coefficient between the antenna and the chip. Once all simulation

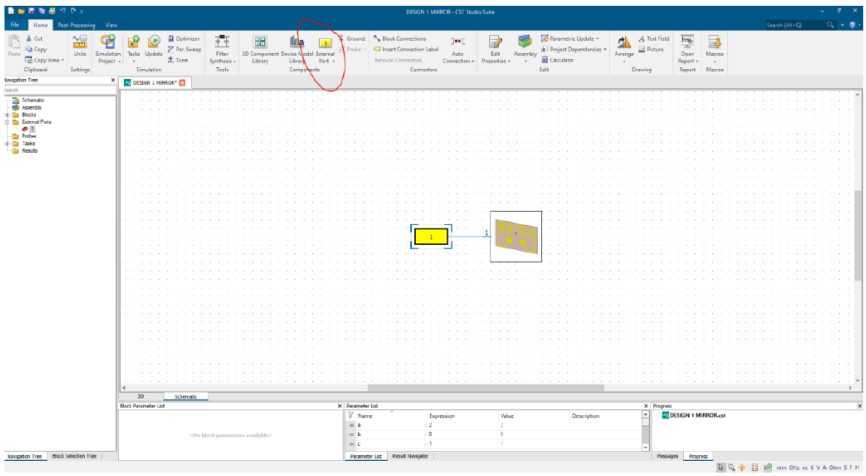
parameters, solver settings, and port configurations were completed, the simulation was initiated by updating and running the solver as depicted in Figure 3.6(e).



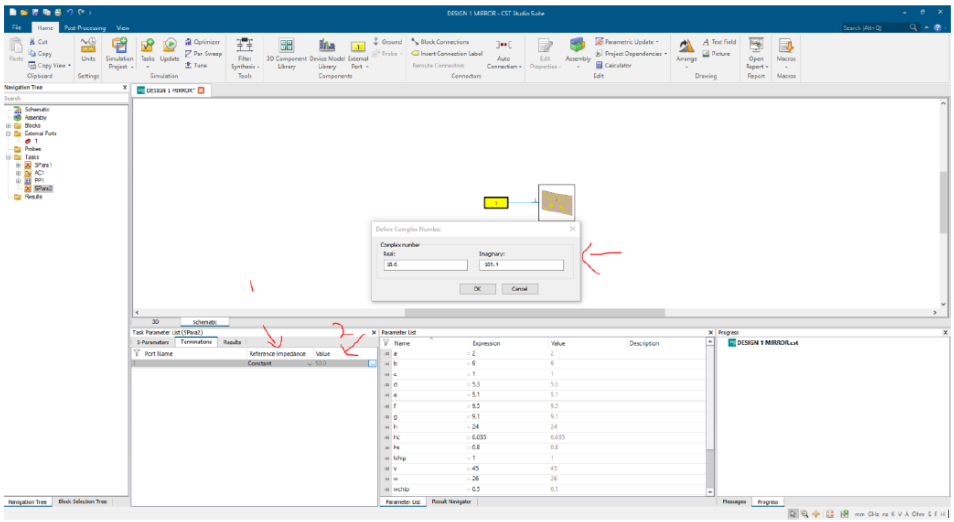
(a)



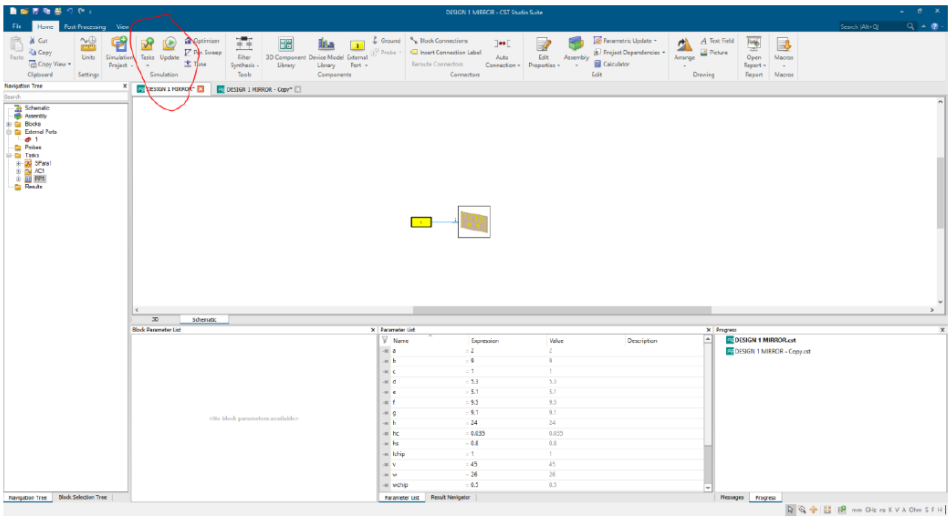
(b)



(c)



(d)



(e)

Figure 3.6 Simulation Setup Of The RFID Tag Antenna With Microchip In CST: (a) 3D Antenna Model With Chip Placement, (b) Discrete Port Across The Feed Gap, (c) Schematic Port Connection, (d) Chip Impedance Setting, And (e) Final Solver Execution.

3.6 Fabrication of RFID Tag Antenna

The process of RFID tag antenna prototype fabrication using the chemical etching technique is illustrated in Figure 3.7 and is explained in detail in this section. The fabrication begins with printing the final layout mask of the antenna design onto a sheet of tracing paper. A photoresist layer is then applied onto the PCB substrate, with care to prevent premature exposure to light that would compromise its effectiveness. The first protective film of the photoresist is peeled off, and the substrate is passed

through a pre-heated lamination machine. This step must be performed carefully to avoid the formation of air bubbles on the laminated PCB substrate.

Next, the printed mask is carefully aligned with the laminated substrate and exposed to ultraviolet (UV) light for approximately 30 seconds using a double-sided UV vacuum exposure machine. Following UV exposure, the second protective layer of the photoresist is removed, and the substrate is immersed in a PCB developer containing sodium carbonate. During this developing process, gentle agitation is applied until the antenna pattern becomes clearly visible on the substrate. The developed substrate is then transferred into an etching tank for 15–30 minutes, during which the unwanted copper is dissolved, leaving only the copper pattern corresponding to the antenna design. After etching, the substrate board is rinsed with distilled water and immersed in a strip-off solution consisting of sodium hydroxide to remove any residual photoresist. Finally, the substrate is rinsed once more and dried, completing the fabrication process.

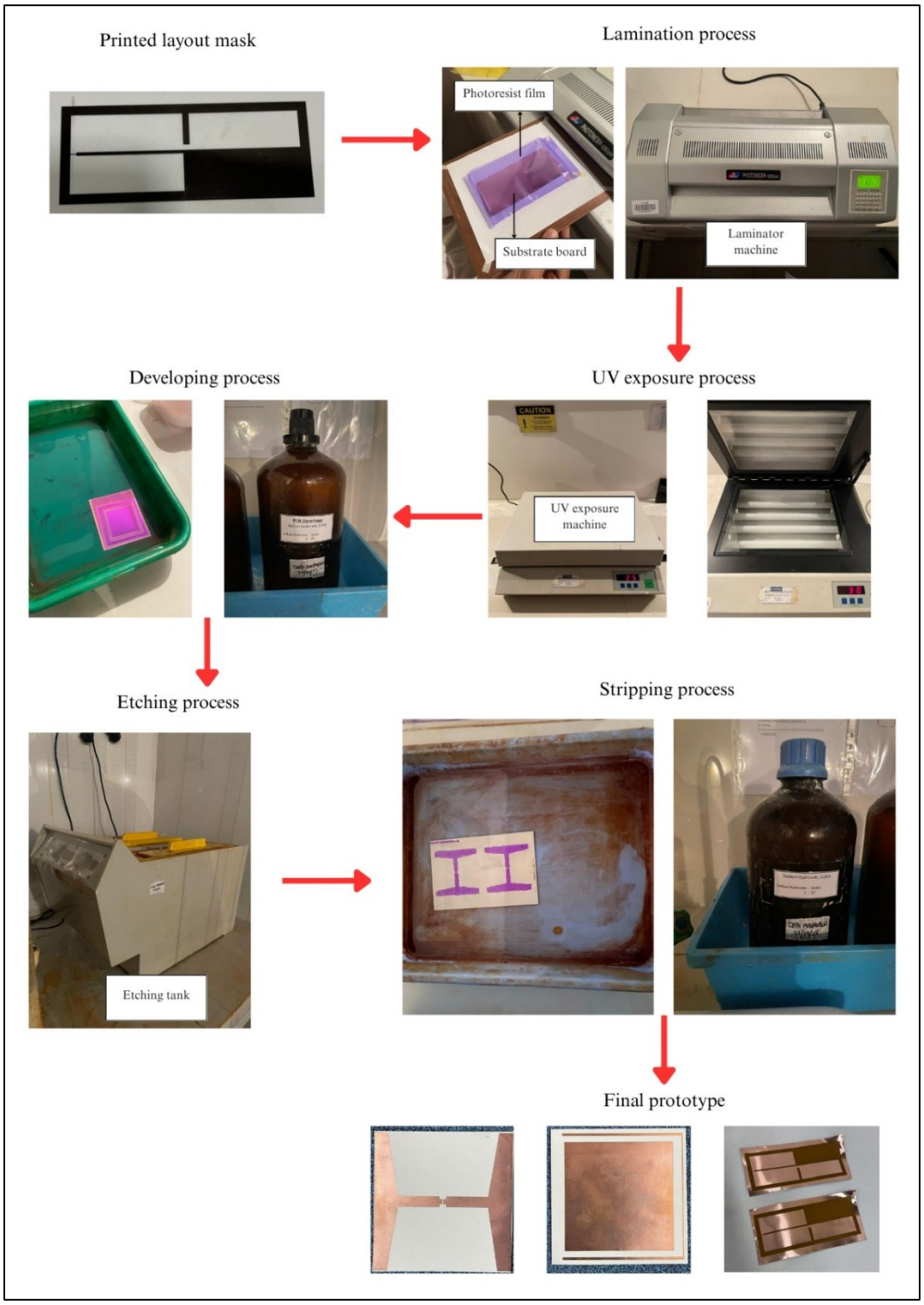


Figure 3.7 RFID Antenna Prototype Fabrication Using Chemical Etching Technique.

3.7 Measurement of RFID Tag Antenna Technical Parameters using Voyantic Tagformance Pro System

The Voyantic Tagformance Pro is an RFID measurement platform used to evaluate the performance of UHF RFID tag prototypes under standardized test conditions. It operates across the frequency range of 800 MHz to 1 GHz, enabling

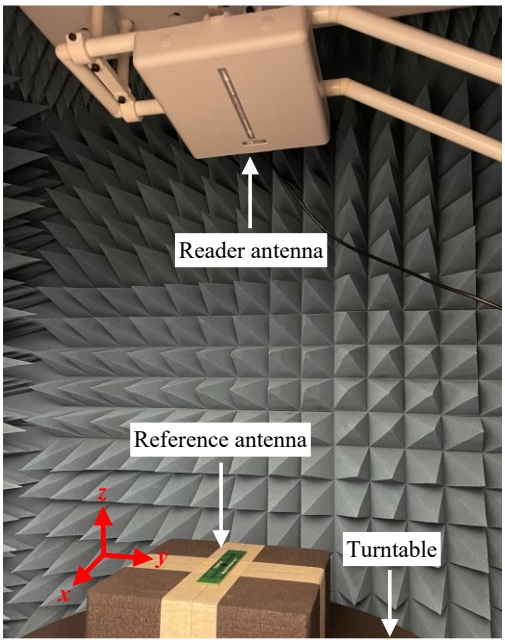
accurate measurement of parameters such as tag sensitivity also can be called power on tag forward (P_{tag}), read range (R_{max}), and frequency response. For clarity of visualization, the measurement setup and schematic diagram inside the anechoic chamber are illustrated in Figure 3.8.

The Voyantic Tagformance Pro measurement system, which integrates two 8 dBi linearly polarized (LP) reader antennas, is installed inside a shielded anechoic cabinet to provide a controlled environment and eliminate interference from unwanted external signals. During calibration, a UHF reference antenna tag is placed at the centre of a turntable inside the anechoic cabinet and used as the tag under test (TUT). The reference tag is supported by a Styrofoam block ($\varepsilon_r \approx 1$) as illustrated in Figure 3.8(a). Upon completing calibration, the reference tag is replaced with the proposed tag antenna, which is mounted at the centre of a 200 mm × 200 mm metal plate to measure its read distance.

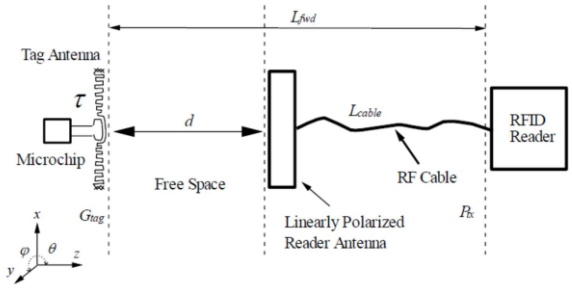
The forward path loss (L_{fwd}) between the RFID reader and tag under test (TUT), as shown in Figure 3.8(b), is calibrated across the frequency range of 800–1000 MHz and is defined as

$$L_{fwd}(dB) = -L_{cable}(dB) + G_t + -FSPL \tag{3.19}$$

where G_t is the gain of the reader antenna, L_{cable} denotes the cable loss between the reader and antenna, and FSPL represents the free-space path loss (S. R. Lee et al., 2022b). The reader antenna is positioned at a fixed distance along the z-axis from the tag under test and maintained consistently for all measurements.



(a)



(b)

Figure 3.8 Experimental Validation Setup: (A) Actual Measurement Configuration for The RFID Tag Antenna, and (B) Schematic Diagram of The Voyantic Tagformance Pro Measurement System Used for Tag Performance Characterization.

3.8 Summary

This chapter has presented the research methodology employed in the development of the proposed UHF RFID tag antenna for on-metal applications. The overall process composed design modelling, full-wave electromagnetic simulation using CST Microwave Studio, prototype fabrication, and measurement validation to achieve the targeted performance objectives.

The chapter established the key design requirements and performance parameters that guided the overall research process. It also detailed the antenna design, including the dipolar patch, RFID microchip, and the working principles of the Huygens' metasurface (HMS). The simulation of the RFID tag with microchip was

elaborated. The fabrication and measurement procedures were further described. The close agreement between the simulated and measured results verifies the effectiveness of the proposed methodology and confirms the antenna's reliability and performance in metallic environments

CHAPTER 4
EMBEDDED - INDUCTANCE FOLDED STACKED PATCH TAG ANTENNA WITH INCLINED SLOTS

4.1 Introduction

This chapter presents a novel double-layered folded-patch tag antenna with embedded inclined slots designed for on-metal RFID applications. It begins by exploring folding as a miniaturization technique, enabling a compact and efficient design suitable for challenging metallic environments in Subsection 4.2.

In Subsection 4.3, the antenna's design is detailed, highlighting the double-layered configuration and embedded inclined slots that optimize performance. A thorough analysis of the design principles, parametric optimization, and working mechanism is provided, emphasizing how the inclined slots facilitate precise frequency tuning and impedance matching without modifying the antenna's structure.

Subsection 4.4 focuses on the experimental evaluation of the fabricated prototype. Performance metrics such as read distance, realized gain, and radiation patterns are measured to validate the antenna's real-world effectiveness. The results confirm the reliability and practicality of the proposed design for on-metal applications.

This chapter comprehensively analyses the novel folded-patch tag antenna, from design and optimization to experimental validation. Integrating embedded inclined slots and a folded structure addresses traditional tuning challenges, offering a compact, high-performance solution for on-metal RFID applications. These findings contribute to further advancements in RFID technology, particularly for metallic environments.

4.2 Preliminary Design of Folded Stacked Patch On-Metal Tag Antenna

This section investigates the concept of a folded stacked patch configuration for the miniaturization of RFID tag antennas and identifies the key geometrical parameters that influence its electromagnetic performance. The preliminary folded tag-antenna design is first presented to examine the effectiveness of the folded configuration as a miniaturization technique and to serve as a reference model for subsequent design refinement. An initial evaluation of its fundamental performance characteristics is then carried out. The assessment focuses on the power transmission coefficient and antenna

input impedance, which provide essential indicators prior to further optimization and experimental validation.

The study begins with a conventional single-layer patch configuration, illustrated in Figure 4.1, which consists of a single radiating patch and a ground plane connected through a shorting stub. This structure serves as the reference design for evaluating the effectiveness of the proposed folded approach. CST Microwave Studio was employed to design, simulate, and optimize both antenna configurations. For consistency in simulation and measurement, the tag antenna was positioned at the center of a 200 mm × 200 mm metal plate, as the design is specifically intended for on-metal applications.

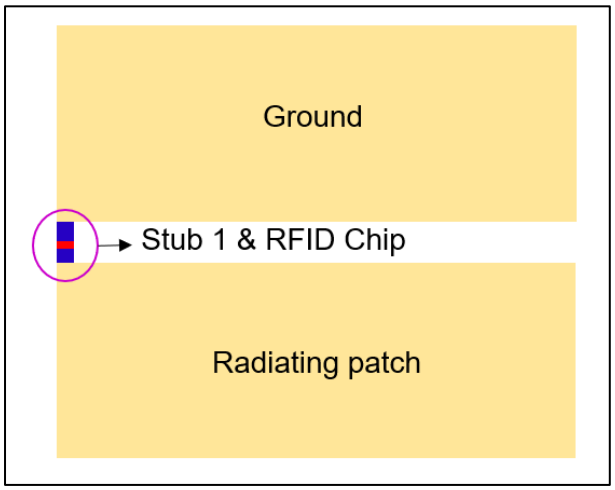


Figure 4.1 The Single-Layered Tag Antenna Configuration.

To achieve size reduction and performance enhancement, a folded stacked-patch configuration was subsequently developed. The proposed double-layered tag antenna, with overall dimensions of 10 mm × 58 mm × 3.6 mm, comprises two radiating patches located at the top and middle layers, with a ground plane at the bottom, as shown in Figure 4.2(a). The antenna is fabricated on a flexible polyimide substrate (ε_r = 3.3, *tan* δ = 0.0027) with a thickness of 0.05 mm and a copper layer of 0.009 mm. Stub 2, with a width of 0.3 mm, connects the top patch to the ground, while Stub 1 shorts the bottom patch to the ground to facilitate integration with the NXP UCODE 8 RFID chip (input impedance 13 – j191 Ω, reading sensitivity –22.9 dBm). Structural stability during folding is provided by two PP4 foam layers, each 1.6 mm thick (ε_r = 1.06, *tan* δ = 0.0001). The unfolded inlay configuration is illustrated in Figure 4.2(b).

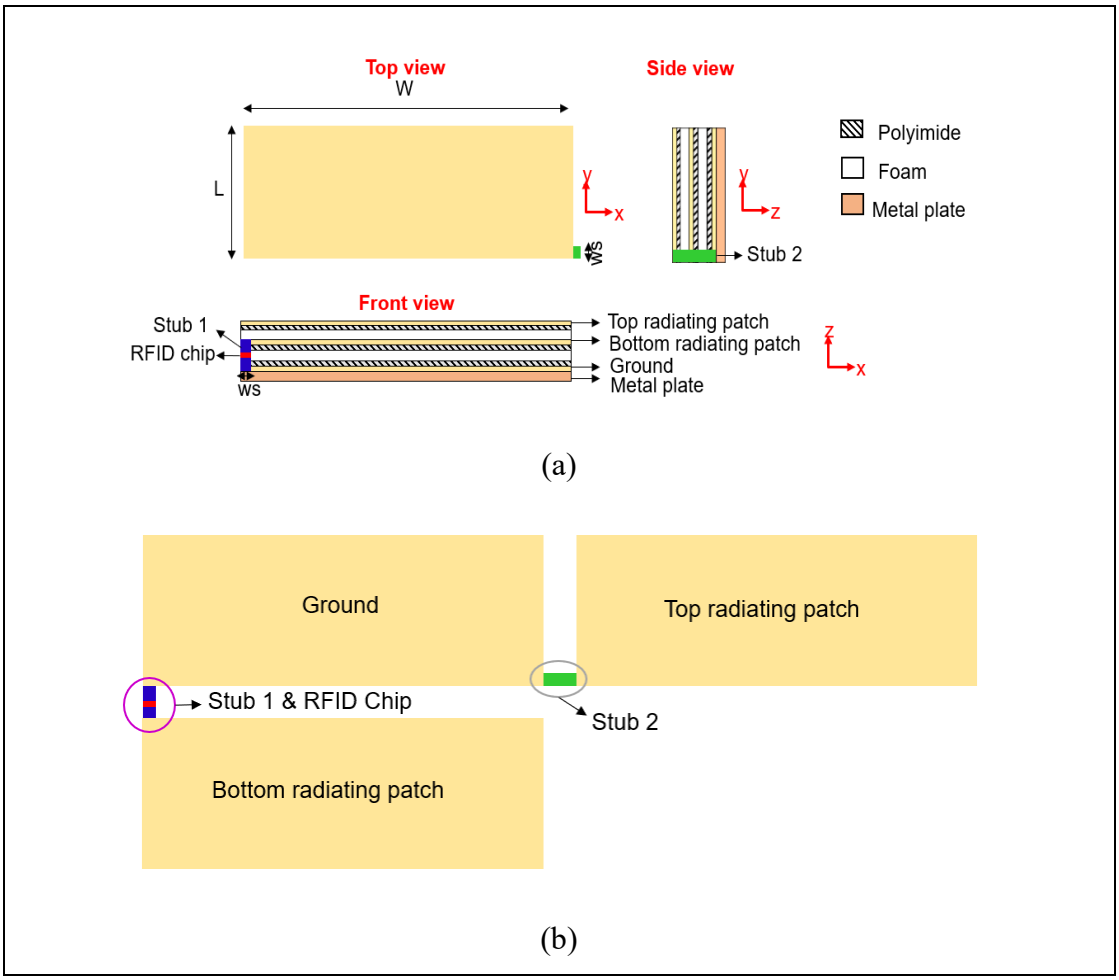


Figure 4.2 (a)Tag Prototype Mounting on the Copper Plate (b) Maximum Read Range in US band.(Mo & Li, 2019)

A comparative performance evaluation between the single-layered and double-layered configurations is conducted in terms of the power transmission coefficient (τ) and input impedance (Z_{in}), as summarized in Table 4.1. This systematic comparison enables assessment of the effectiveness of the folded configuration in achieving antenna miniaturization and improved impedance matching for on-metal RFID applications.

Table 4.1
Comparison of Single and Double-Layered Tag Antenna

	Single-layered tag antenna	**Double–layered tag antenna**
Width (mm)	143	58
Length (mm)	10	10
Frequency (MHz)	915	915
Power transmission coefficient, τ	0.88	0.97
Antenna impedance, Z_{in}	8 + j197	19 + j 191

This single-layered configuration resonated at 915 MHz with an input impedance of 8 + j197 Ω and achieved a τ value of 0.88 as shown in Figure 4.3.. However, its relatively large physical footprint limited its suitability for compact RFID tag applications. To address this limitation, the double-layered configuration incorporated a stacked radiating patch using a folding technique. This modification reduced the tag length by 84 mm while increasing the power transmission coefficient to 0.97, representing a 9% improvement compared to the single-layered design. These findings show that the folded double-layered architecture improves miniaturization and impedance matching, thereby enhancing overall RFID tag performance.

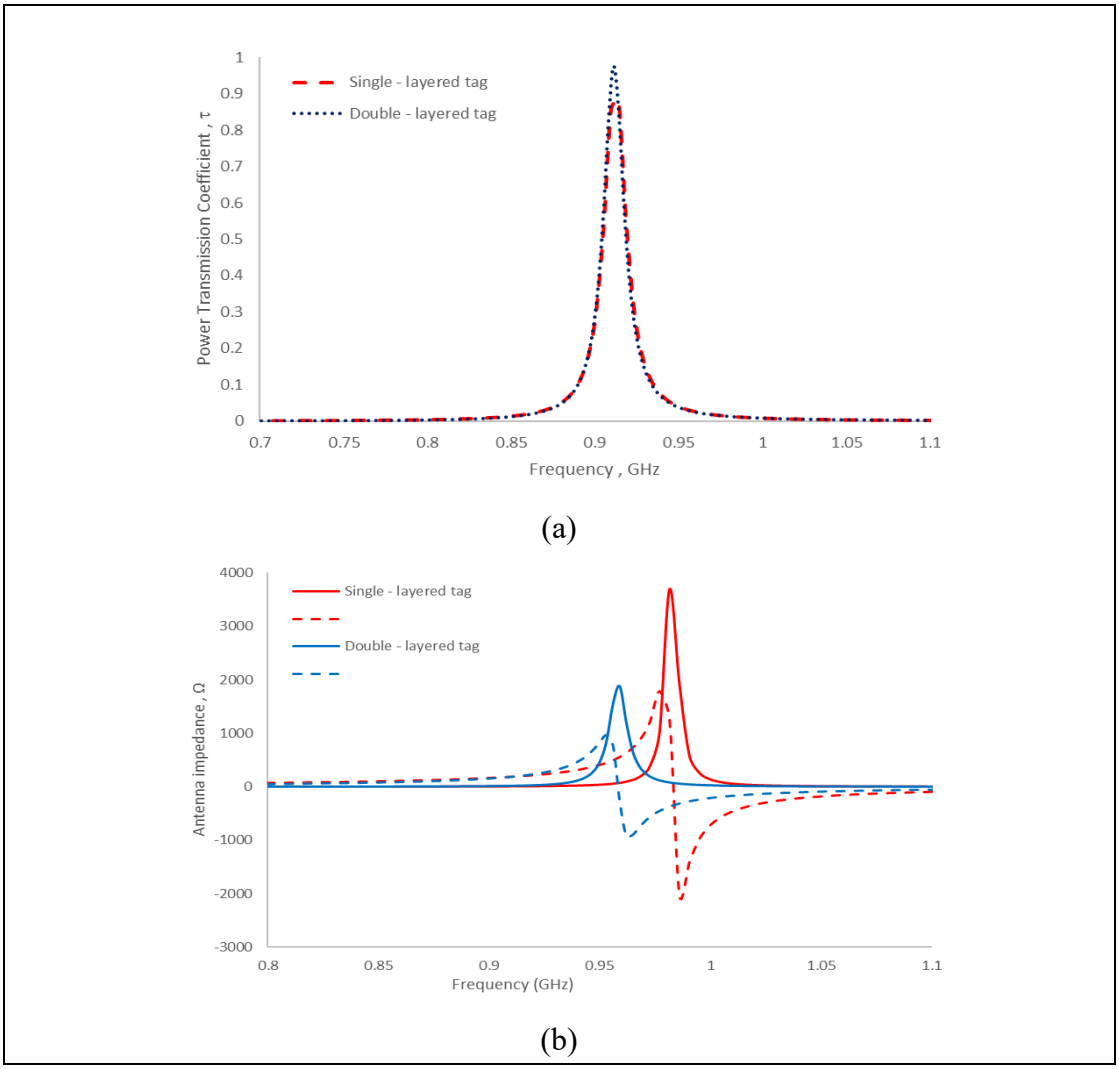


Figure 4.3 (a) Power Transmission Coefficient, τ (b) Antenna Impedance of The Single-Layered and Double-Layered Tag Antenna

Furthermore, integrating an extra stub optimizes current distribution and improves conjugate matching, resulting in better power transfer efficiency. The double-layered structure minimizes the tag's physical footprint and significantly enhances its

performance. While the double-layered configuration introduces additional capacitance to reduce the antenna size, it lacks a tuning mechanism, and the overall dimensions are still affected. Modifications to the overall structure are necessary to minimize the antenna footprint further and precisely shift the operating frequency to the desired range.

4.3 Folded Stacked Patch Antenna with Inclined Slot

This section presents a novel radio frequency identification (RFID) folded-patch tag antenna employing a double-layered configuration with embedded inclined slots for efficient on-metal applications. The double-layer structure, illustrated in Figure 4.2 introduces additional capacitance that contributes to footprint reduction and antenna miniaturization. However, as discussed in Subsection 4.2, the configuration lacks an effective tuning mechanism. To address this limitation, the folded stacked-patch antenna integrates five inclined slots that act as embedded inductive elements, thereby introducing an effective tuning mechanism for improved impedance matching and tag performance. A comprehensive discussion of the design evolution and its working principles is presented in the following section.

The configuration and design evolution of the tag antenna will be explained in this section, with particular emphasis on the role of the inclined slots, which function as embedded inductors. This tuning approach offers a significant advantage by enabling frequency and reactance adjustments without altering the overall antenna dimensions, thus preserving its compact footprint. Finally, the working principle of the embedded inductance as a tuning mechanism is discussed, including the finer adjustments of the inclined slot dimensions.

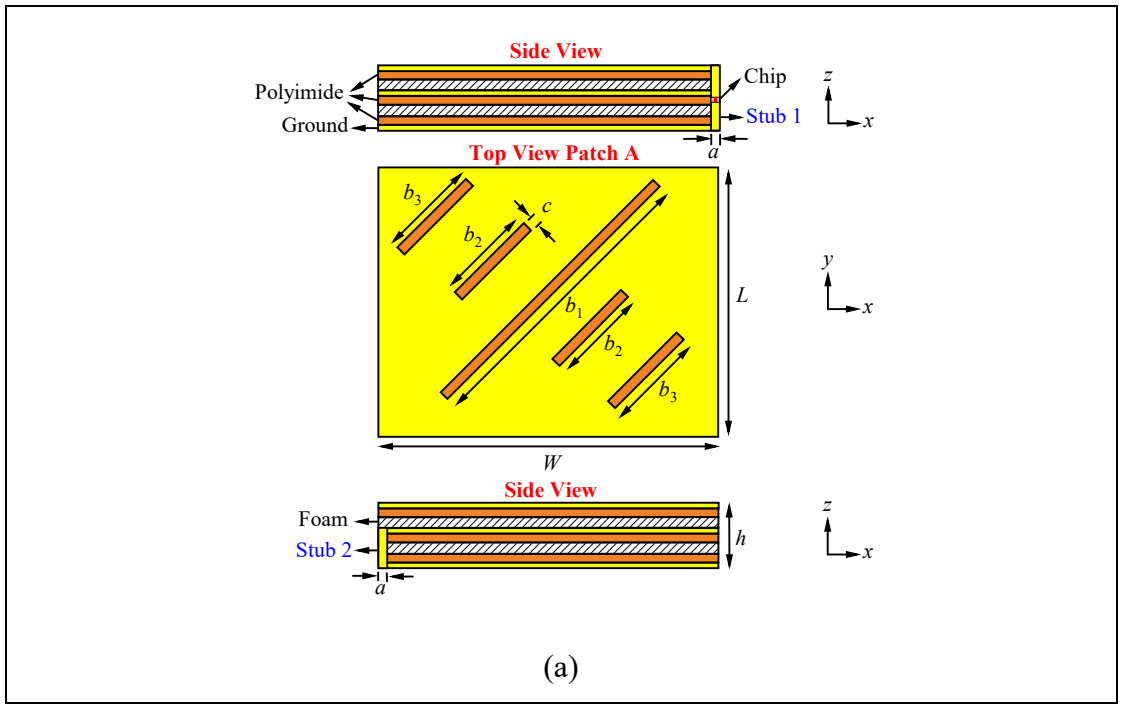
4.3.1 Simulation Model of a Double-Layered Folded-Patch Tag Antenna with Slots

This section comprehensively describes the double-layer folded patch tag antenna with embedded inductance configuration, including the optimal dimensions, fabrication process, and prototype development. To accurately model the tag antenna, a complex-impedance external discrete port is employed in the simulation to represent the RFID chip.

The tag is realized by depositing a thin copper layer (thickness = 9 μm) onto a 50 μm flexible polyimide substrate with a dielectric constant of 3.3 and a loss tangent

of 0.0027. Figure 4.4 (a) presents the top view of Patch A, highlighting the tunable inclined slots, while the side perspective illustrates the positions of the stubs and the chip. The design incorporates five slim inclined rectangular slots, measuring $b_1 \times c$, $b_2 \times c$, and $b_3 \times c$, which are integrated into Patch A and B. The slots on Patch A are oriented 45° clockwise, while those on Patch B are positioned 45° counterclockwise. These inclined slots serve as embedded inductances, with a detailed analysis provided in the following subsection.

Patch A and B are shorted to the ground plane via two inductive stubs in the side view. As shown in the side view, a UCODE 8 microchip is bonded at the center of Stub 1. The chip has an input impedance of $13 - j191\ \Omega$ at 915 MHz, with a reading sensitivity of –22.9 dBm. As shown in the side view in Figure 4.4(a), the antenna structure is supported by two layers of PP4 foam, which have a dielectric constant of 1.06 and a loss tangent of 0.0001. These foam layers provide structural stability, ensuring the tag maintains its shape. Figure 4.4(b) and (c) illustrate the top view of Patch B and the ground plane. The optimal design parameters are summarized in Table 4.2.



(a)

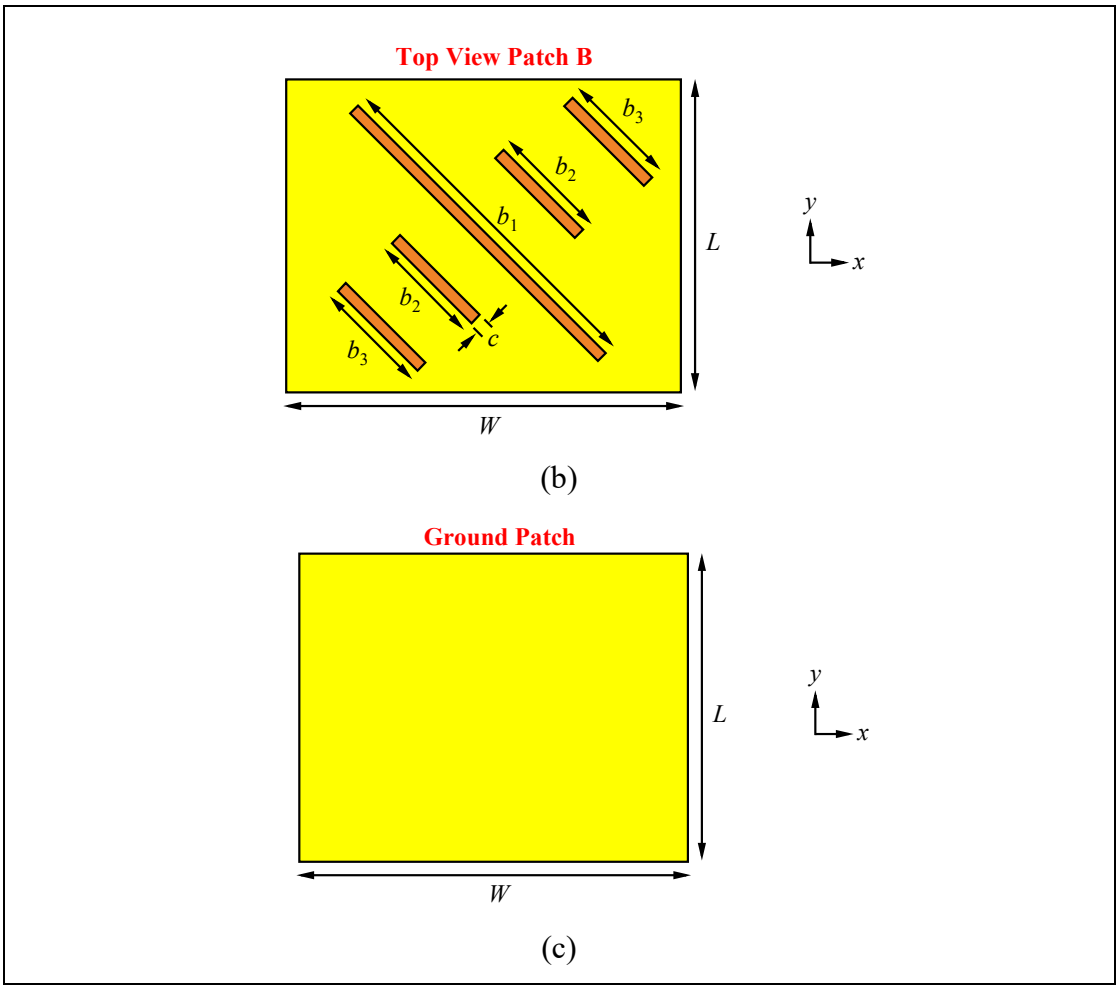


Figure 4.4 The Double-Layered Tag Antenna Configuration: (a) Top and Corresponding Views of Patch A, (b) Top View of Patch B, And (c) Ground Plane.

Table 4.2
Optimum Design Parameters of The Tag Antenna

Parameter	Dimension (mm)	Parameter	Dimension (mm)
L	32	b_2	5
W	40	b_3	5
a	3	c	1
b_1	35	h	3.35

4.3.2 Parametric Analysis and Design Evolution of Double-Layer Folded Patch Tag Antenna with Embedded Inductance

A detailed parametric analysis is conducted to examine the structural evolution of the folded patch RFID tag antenna and to evaluate the impact of each design modification on its performance characteristics. The design progression consists of three configurations: a single-layered patch, a double-layer patch, and a slotted double-

layer patch, as illustrated in Figure 4.5. The key performance parameters corresponding to each configuration, including resonant frequency, input impedance, power transmission coefficient, and realized gain, are summarized in Table 4.3.

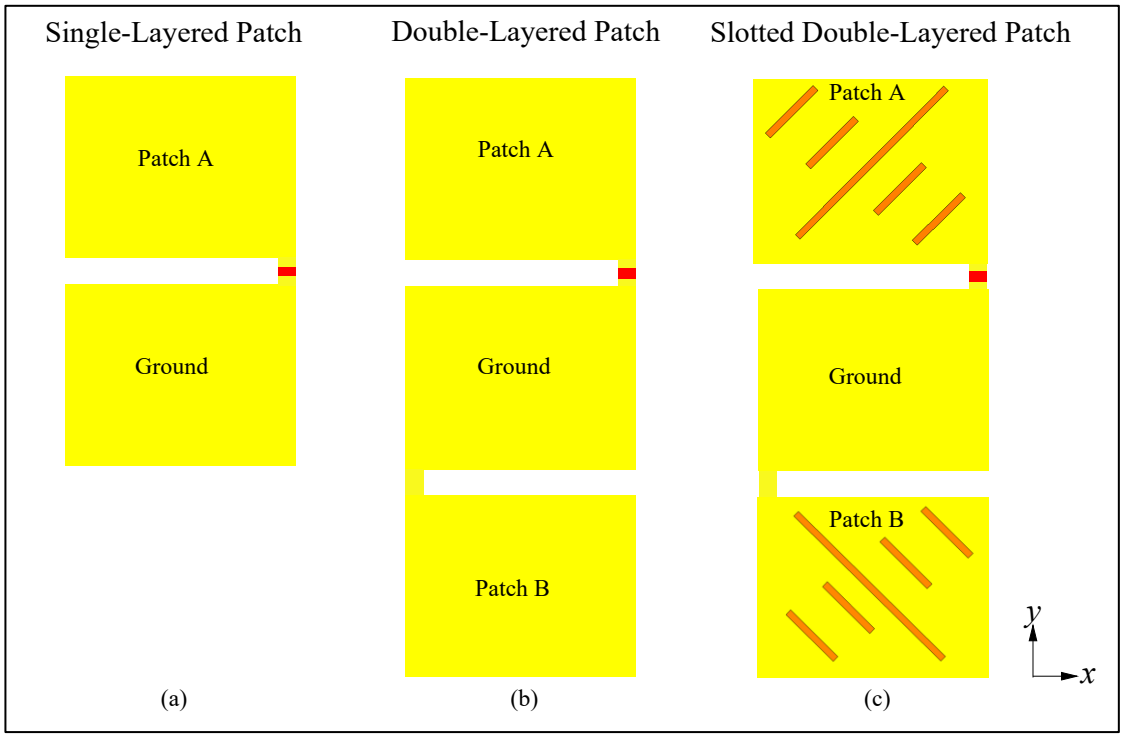
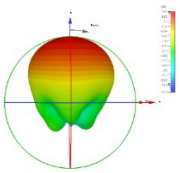
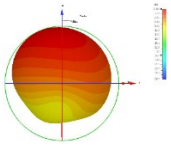
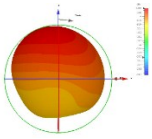


Figure 4.5 Design Evolution Of The Double-Layer Folded Patch Tag Antenna, Showing (a) The Single-Layered Patch Configuration, (b) The Formation Of The Double-Layer Patch Structure, And (c) The Final Configuration Incorporating Inclined Slots.

Table 4.3
Comparison Of the Key Performance Parameters of the RFID Tag Antenna Across the Three Stages of Structural Evolution

Design	Single-layered patch	Double-layered patch	Slotted double-layered patch
Resonant frequency (MHz)	2460	967	916
Antenna impedance (Ω)	41.05 + j174.86	12.82 + j192.07	8.64 + j190.93

Power transfer coefficient	0.67	0.97	0.96
Realized gain (dBi)	7.050	0.288	0.853
Realized gain (3D)			

The analysis begins with the single-layered patch configuration, in which the bottom patch (Patch B) is removed, leaving only Patch A above the ground plane. The configuration, as shown in Figure 4.5(a) results in a resonance frequency of 2.46 GHz, with an antenna impedance of 41.05 + j174.86 Ω, as shown by the blue curve in Figure 4.6(a). Although this structure exhibits a relatively high realized gain of 7.05 dBi as indicated in Table 4.3, it suffers from poor impedance matching, as evidenced by the low power transmission coefficient of 0.67 in Figure 4.6(b). Furthermore, the operating frequency resonates outside the regulated RFID UHF passband, rendering this configuration unsuitable for practical RFID tag applications.

To address these limitations, a double-layered patch configuration is introduced by incorporating Patch B between Patch A and the ground plane. This modification shifts the operating frequency downward to 967 MHz, bringing it closer to the desired RFID operating range. The antenna impedance for this configuration is 12.82 + j192.07 Ω, as shown in Figure 4.6(a), with a power transmission coefficient of 0.97, indicating substantially improved impedance matching. The cascading of Patch A and Patch B introduces additional capacitance, which plays a critical role in lowering the operating frequency and enhancing the overall electromagnetic performance of the tag.

Further optimization is achieved by integrating inclined slots on both radiating patches, as illustrated in Figure 4.5(c). This modification results in a resonance frequency of 916 MHz, placing the antenna within the US UHF RFID passband. The antenna impedance is adjusted to 8.64 + j190.93 Ω, with a corresponding power transmission coefficient of 0.96, demonstrating excellent impedance matching. The realized gain of the tag is measured at 0.850 dBi. The introduction of inclined slots effectively fine-tunes the current distribution on the radiating patches, enabling precise control of the operating frequency and contributing to optimal impedance matching.

This detailed analysis highlights the critical role of each design modification in achieving a high-performance RFID tag antenna.

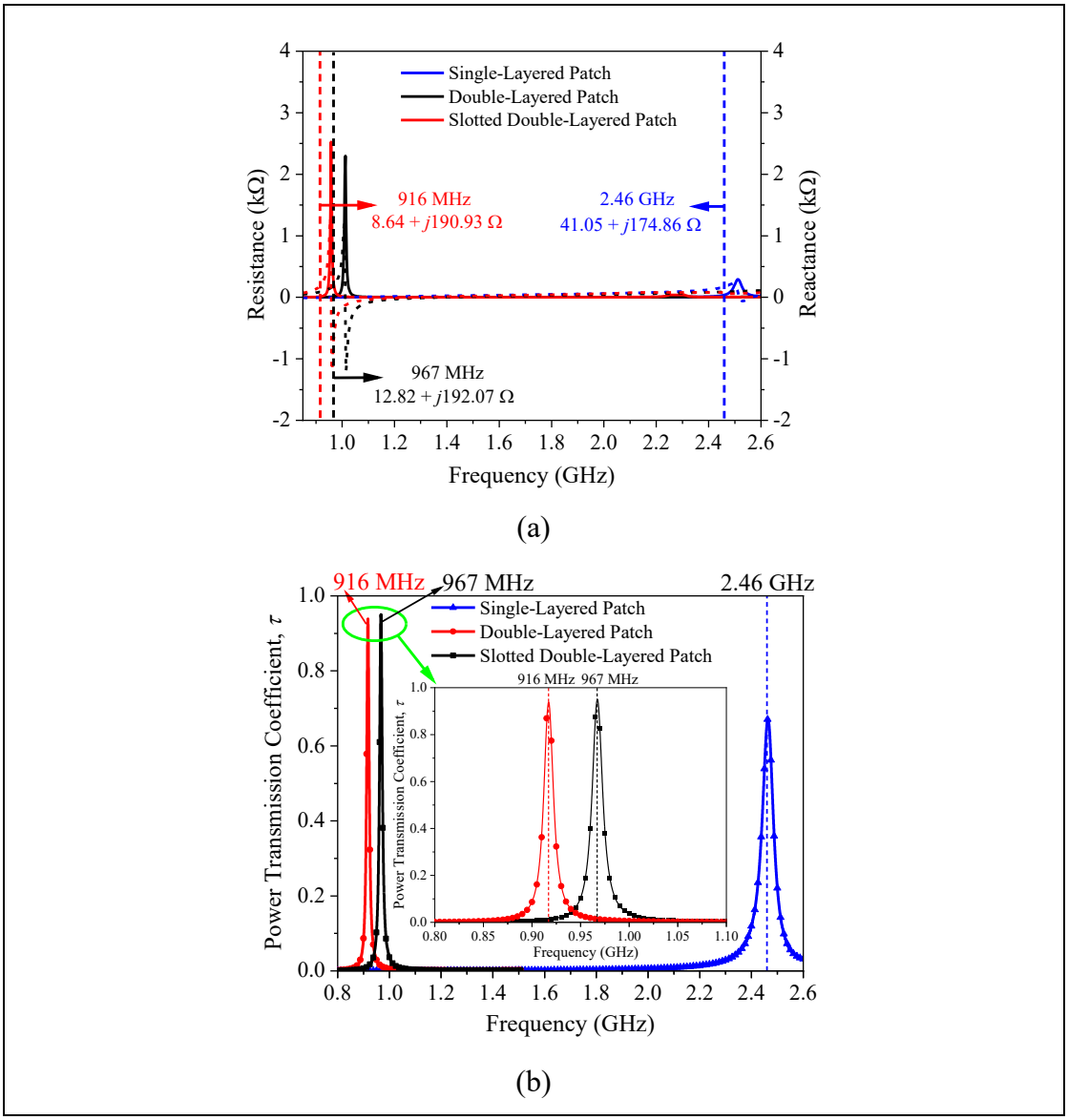


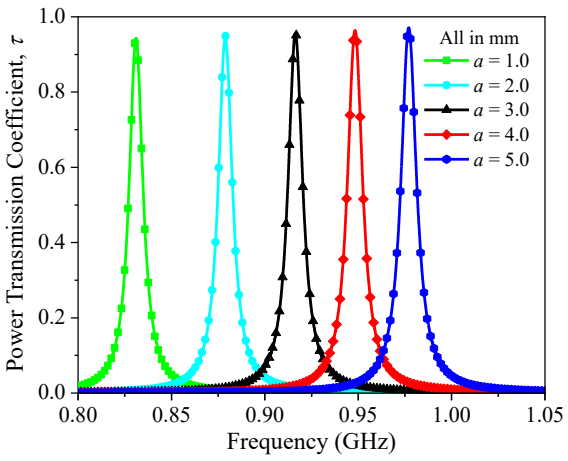
Figure 4.6 (a) Antenna Input Impedance and (b) Power Transmission Coefficient (T) for The Three Design Stages: The Single-Layered Patch Configuration, The Double-Layer Patch Configuration, And The Final Structure With Inclined Slots On Both Patches.

4.3.3 Slot and Stub Parameter Optimization

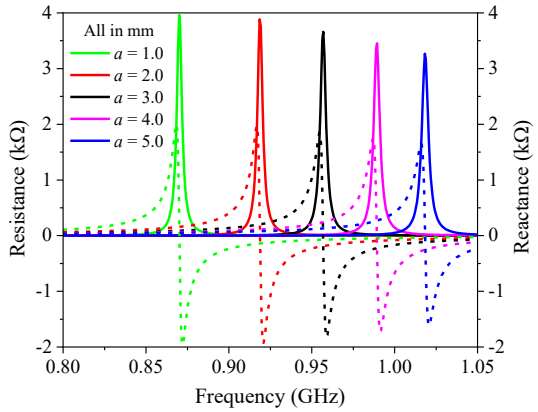
A parametric analysis is systematically conducted to evaluate the influence of critical design parameters on the power transmission coefficient (τ) and antenna impedance (Z_{ant}). The first parameter under investigation is the stub width (a), which is varied incrementally from 1 mm to 5 mm while maintaining constant values of b_1 = 35 mm and c = 1 mm, as depicted in Figure 4.7(a)–(c). As illustrated in Figure 4.7(a),

increasing the stub width (a) makes a shift in the resonant frequency from 831 MHz to 976 MHz while maintaining a power transmission coefficient (τ) above 0.95. This frequency shift is attributed to the reduction in inductive reactance associated with broader stubs, which lowers the overall antenna reactance. The observed average frequency shift rate of 36 MHz per 1 mm increment in stub width highlights the potential of this parameter for coarse frequency tuning in the design process.

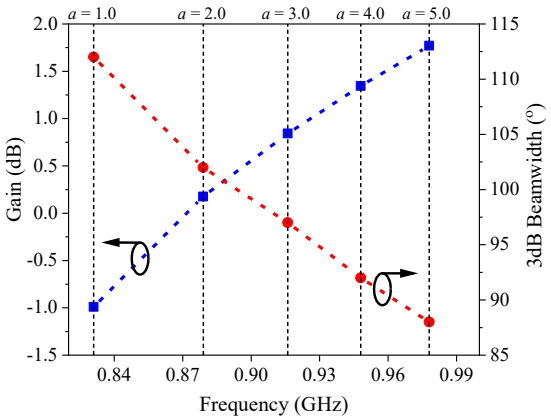
The impact of the stub width (a) on the realized gain and 3 dB beamwidth is further analyzed to provide a comprehensive understanding of its effects. As depicted in Figure 4.7(c), the realized gain of the tag antenna improves from –0.99 dB to 1.77 dB as the stub width is increased from 1 mm to 5 mm. This improvement in gain is due to the expanded antenna footprint, which creates a larger radiating aperture and enhances the antenna's ability to emit energy more efficiently. Additionally, since gain and beamwidth are inversely related, the increase in gain corresponds to a reduction in the 3 dB beamwidth.



(a)



(b)

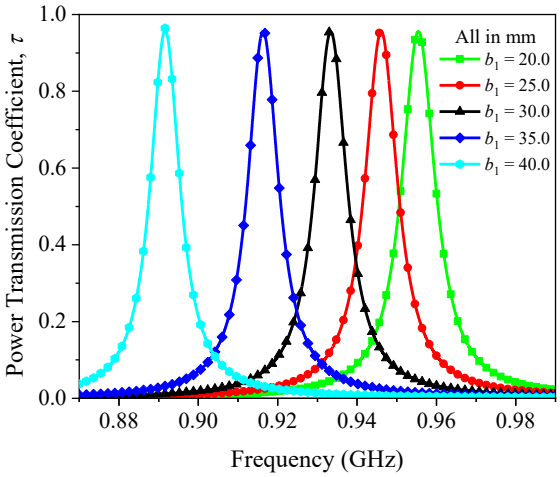


(c)

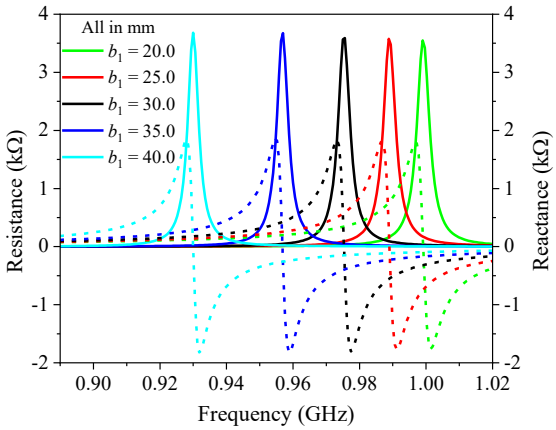
Figure 4.7 Simulated (a) Power Transmission Coefficient, (b) Antenna Impedance and Its (c) Realized Gain And 3dB Beamwidth by Varying the Stub Width, *a*.

Next, the length (b_1) of the centre slot is varied in increments of 5 mm to analyze its impact on the tag's performance. As illustrated in Figure 4.8(a), the resonant frequency of the tag shifts downward from 955 MHz to 891 MHz as b_1 is lengthened while keeping a = 35 mm and c = 3 mm. This is attributed to the elongation of the current path, which forces surface currents to navigate a longer distance, thereby increasing the effective electrical length of the antenna. Despite this frequency shift, the power transmission coefficient (τ) remains consistently high, maintaining a value of 0.95 across all variations of b_1 throughout the parameter sweep.

Furthermore, the antenna's resistance and reactance exhibit minimal variation as b_1 is increased from 20 mm to 40 mm, as demonstrated in Figure 4.8(b). The reactance shows negligible variation, suggesting that the inductive and capacitive properties of the antenna remain balanced despite the modification to the slot length. This impedance stability highlights the design's robustness to b_1 variations, ensuring consistent performance despite resonant frequency adjustments. The parametric analysis of the centre slot length (b_1) reveals its critical role in fine-tuning the resonant frequency of the tag antenna.



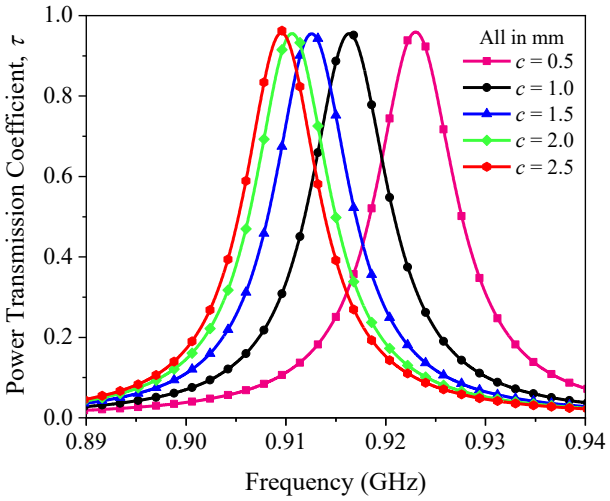
(a)



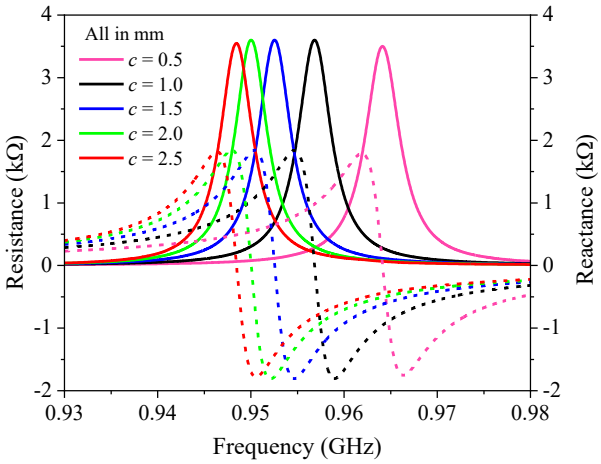
(b)

Figure 4.8 Simulated (a) Power Transmission Coefficient And (b) Antenna Impedance by Varying Slot Length ,b_1.

Increasing the width (c) of the embedded slots from 0.5 mm to 2.0 mm while maintaining constant values of a = 3 mm and b_1 = 35 mm results in a downward shift in the tag's resonant frequency. This frequency reduction is accompanied by a simultaneous increase in antenna resistance and reactance, as illustrated in Figure 4.9. The observed behavior is attributed to the additional inductance introduced by the widening of the slots, which alters the current distribution and increases the effective electrical length of the antenna.



(a)



(b)

Figure 4.9 Simulated (a) Power Transmission Coefficient And (b) Antenna Impedance by Varying Slot Width, *c*

In summary, parametric analysis highlights the distinct roles of key design parameters in tuning the resonant frequency of the RFID tag antenna. The stub width (*a*) serves as a coarse tuning mechanism, enabling significant frequency adjustments through modifications to the antenna's inductive properties and radiating aperture. On the other hand, the parameters of the inclined slots, including their length (*b*) and width (*c*), provide fine-tuning capabilities. Altering these embedded slots introduces additional inductance, allowing precise control over the resonant frequency while maintaining optimal impedance characteristics. Together, these parameters offer a comprehensive approach to frequency tuning. The stub width facilitates coarse

adjustments, while fine adjustments are achieved through the inclined slots, ensuring the antenna operates within the desired frequency range with high efficiency.

4.3.4 Embedded Inductance: Working Principles of the Inclined Slot Structure

The working principles of the proposed tag antenna are analyzed to clarify the role of the five inclined slots, which function as embedded inductive elements. The motivation for introducing the five inclined slots is to provide additional degrees of freedom for impedance tuning by increasing the effective current path and inductive loading. This enables precise adjustment of the antenna impedance to closely match the conjugate impedance of the RFID microchip while preserving the compact dimensions of the proposed antenna. To validate this design concept, the relationship between slot length, antenna inductance, and resonant frequency is systematically investigated. As illustrated in Figure 4.10 (a)–(c), a comprehensive study is conducted to evaluate the impact of varying slot lengths on the antenna impedance and frequency resonant.

First, the effect of increasing the length of b_1 is examined while keeping other slot parameters constant at b_2 =5mm and b_3=5 mm. As shown in Figure 4.10 (a), lengthening b_1 increases antenna reactance from 101 Ω to 518 Ω, accompanied by a resonant frequency shifted downward from 955 MHz to 890 MHz.

Next, the parameter b_2 is investigated, with b_1 and b_3 fixed at 35 mm and 5 mm, respectively. As depicted in Figure 4.10 (b), increasing b_2 from 5 mm to 25 mm in 5 mm increments increases antenna reactance due to enhanced inductance. Consequently, the resonant frequency decreases from 916 MHz to 882 MHz.

Similarly, the influence of b_3 is analyzed, as shown in Figure 4.10(c). Increasing the length of b_3 increases reactance from 184 Ω to 369 Ω while the resonant frequency shifts downward.

The analysis reveals that increasing the length of the inclined slots enhances antenna reactance by introducing additional inductance, lowering the resonant frequency without changing the antenna's overall size. These embedded slots function as an effective frequency-tuning mechanism, enabling precise control over impedance and operating frequency. Adjusting the b_1, b_2, and b_3 lengths allows the antenna's inductance to be finely tuned, optimizing RFID tag performance. This inductance-based tuning facilitates frequency control and supports tag miniaturization, making it a valuable design feature for modern RFID applications.

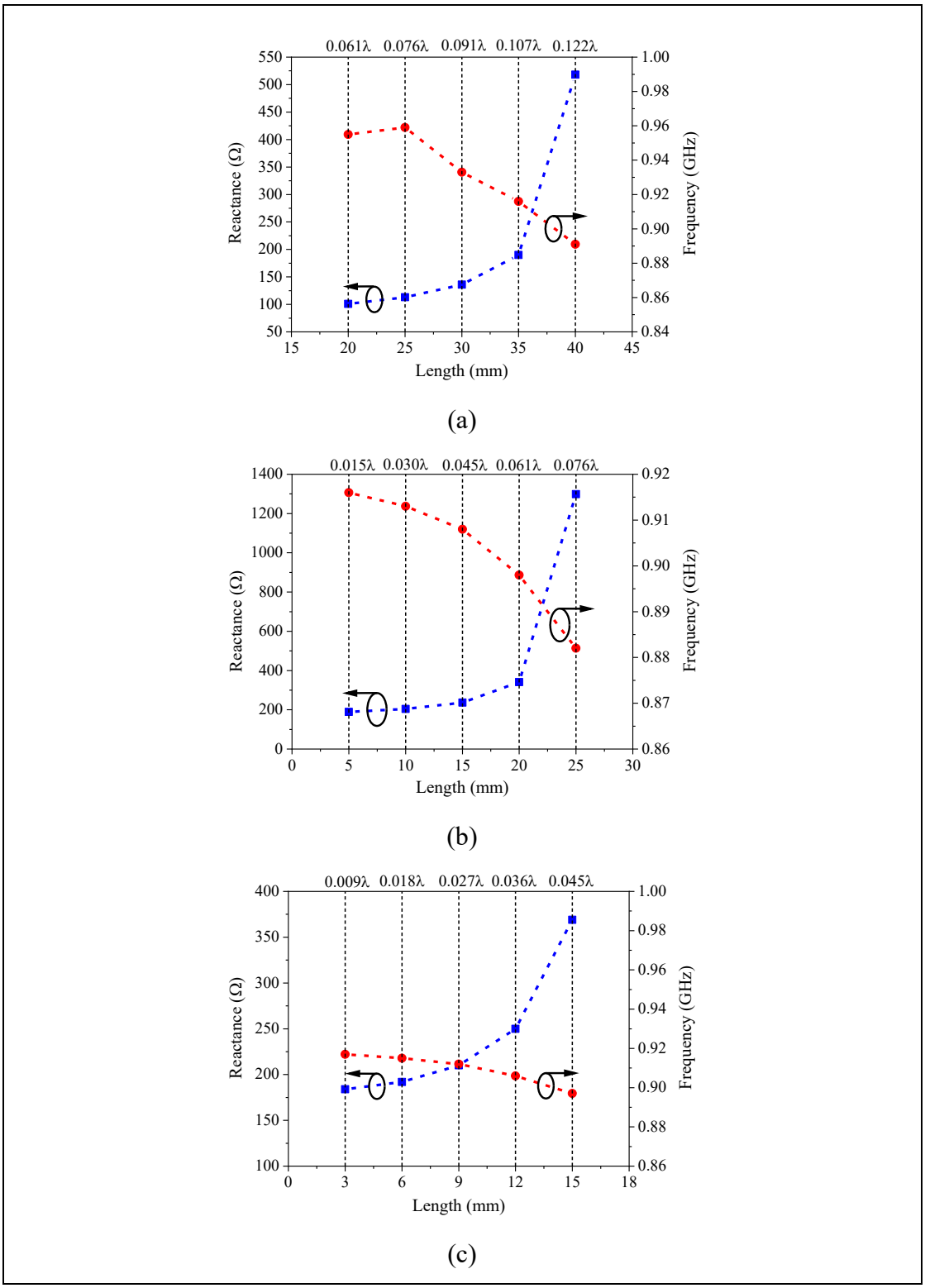


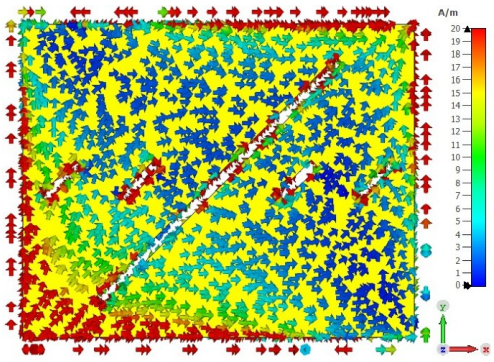
Figure 4.10 Simulated Antenna Reactance and Operating Frequency by Varying (a) b_1, (b) b_2, (c) b_3.

Figure 4.11(a) illustrates the tag antenna's simulated surface current distribution on Patch A. The currents flow from Stub 1 at the lower left corner toward Stub 2 at the upper right corner. Including inclined slots elongates the current path, forcing the

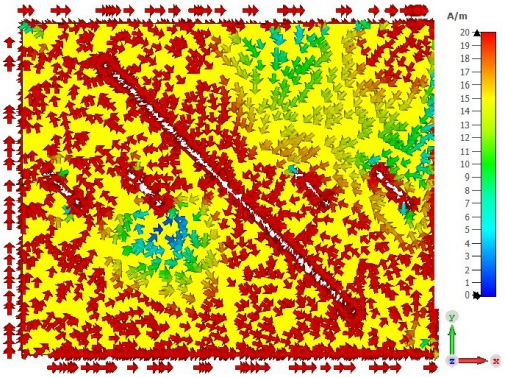
currents to travel a greater distance. This extended path increases the effective electrical length of the antenna, contributing to the tuning of its resonant frequency. Similarly, Figure 4.11(b) depicts the current surface distribution on the bottom patch (Patch B), where the embedded 45° inclined slots exhibit a comparable effect. These slots redirect the current flow, further extending the current path and enhancing the antenna's inductive properties. By adjusting the length of these slots, the resonant frequency of the tag can be finely tuned within a narrow range to achieve a specific target value, demonstrating the effectiveness of this design feature for precise frequency adjustment.

To complement the analysis, the magnetic field (H-field) magnitude along the x-axis is evaluated at y = 2 mm and y = 30 mm, as shown in Figure 4.11(c). Peak magnetic field intensities of 161.75 A/m and 157.40 A/m are observed at the x–y coordinates (–20, 2) and (20, 30), respectively, both located at a z-coordinate of 3.37 mm. These high-intensity regions correspond to zones of elevated current density, consistent with the red-coloured areas in Figure 4.11(a).

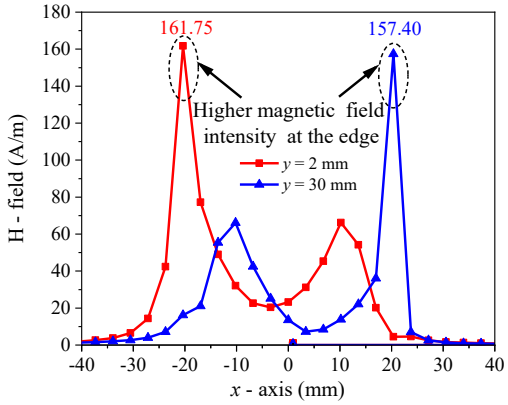
The coordinate positions of the peak field magnitudes are shown in Figure 4.11(d), providing a clear reference for correlating the H-field distribution with the geometry of Patch A. The magnetic field is evaluated at two different y-coordinate positions, namely y = 2 mm and y = 30 mm, because these locations are close to the edges of the patch where Stub 1 and Stub 2 are located, respectively. Consequently, Figure 4.11(d) is not symmetrical because the magnetic field is evaluated at two different y - coordinate positions ($y = 2$ mm and $y = 30$mm). Therefore, the observed asymmetry results from the selected evaluation positions rather than the antenna structure itself.



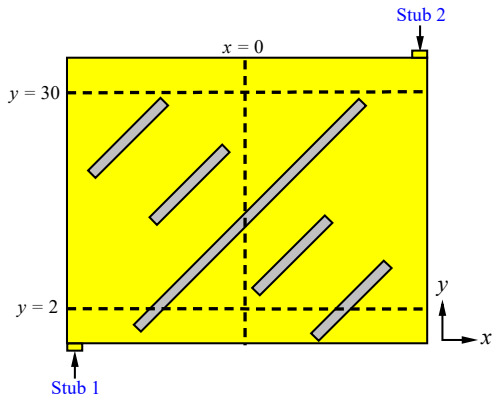
(a)



(b)



(c)



(d)

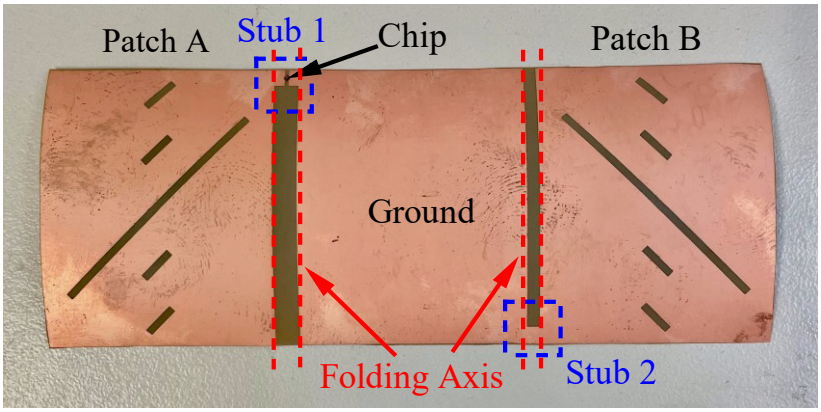
Figure 4.11 Simulated Field And Current Characteristics Of The Tag Antenna: (a) Surface Current Distribution On Patch A; (b) Surface Current Distribution On Patch B; (c) Magnetic Field (H-Field) Magnitude Along The x-axis At y = 2 mm And y = 30 mm; (d) Positions Corresponding To The Peak H-Field Magnitudes.

4.4 Experimental Validation and Performance Analysis

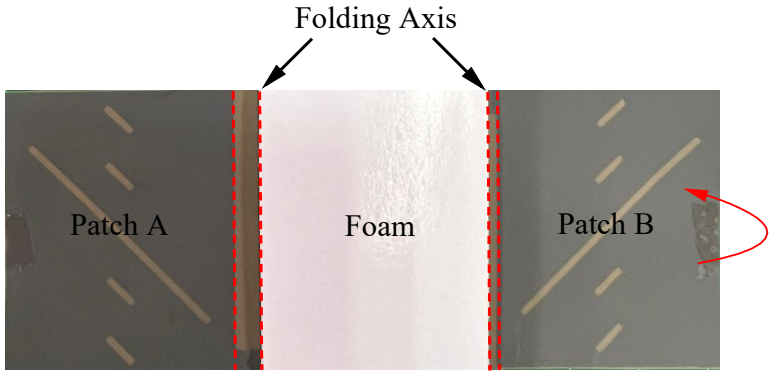
The fabricated tag antenna is implemented using a single-sided copper inlay comprising the radiating patches (Patch A and Patch B), the inductive stubs (Stub 1 and Stub 2), and the ground plane all etched on the same conductive layer, as shown in

Figure 4.12(a).The three-layer configuration is achieved through a folding-based assembly process.

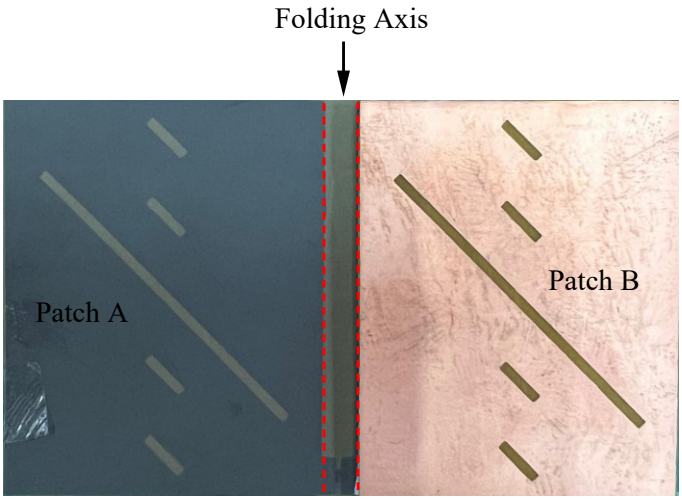
Figure 4.12(b)–(d) illustrate the folding steps, beginning with the placement of a PP4 foam on the ground-plane region of the inlay. The flap containing Patch B is then folded upward and wrapped around the foam using adhesive, as shown in Figure 4.12(b) and (c). A second PP4 foam layer is subsequently positioned, after which Patch A is folded and overlapped onto Patch B to form the complete double-layer structure, as depicted in Figure 4.12(d).The resulting top and perspective views of the assembled prototype are presented in Figure 4.12(e).



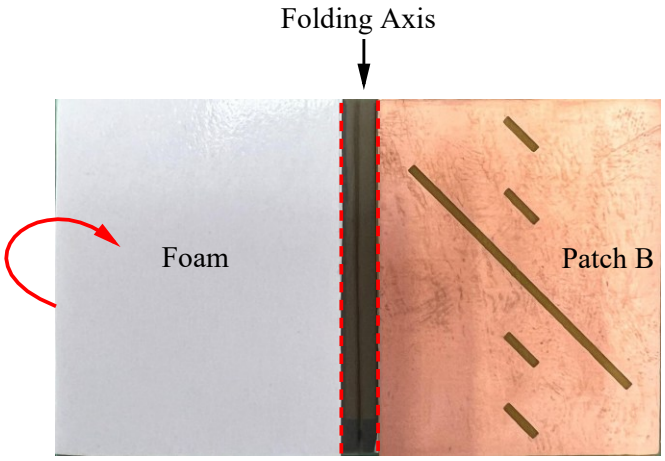
(a)



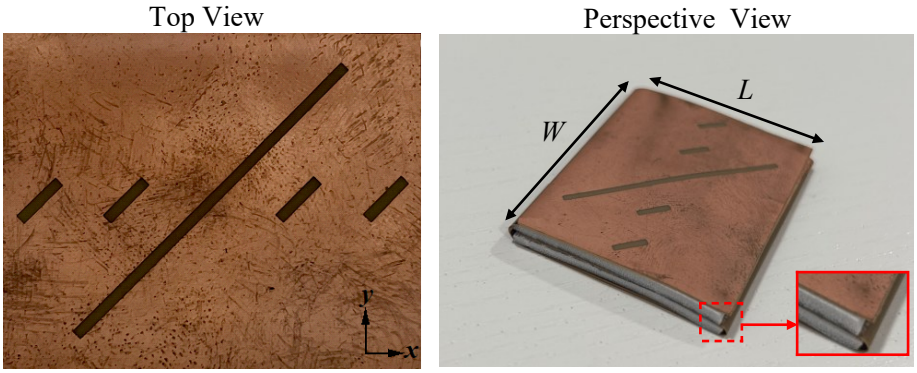
(b)



(c)



(d)



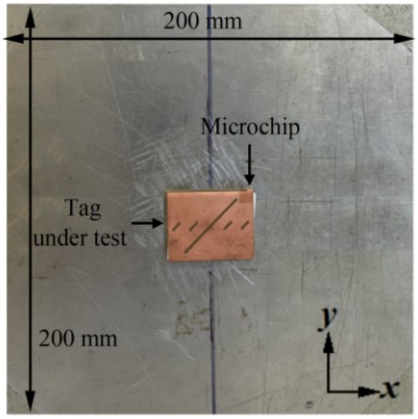
(e)

Figure 4.12 (a) Naked Inlay (b) Step 1 (c) Step 2 (d) Step 3 of the Tag Prototype Folding Process (e) Top and Perspective View of The Fabricated Tag.

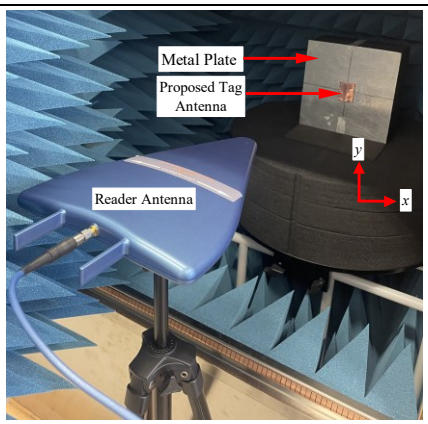
Following the fabrication of the folded prototype, the tag's read distance, realized gain, and radiation pattern were experimentally evaluated inside an anechoic

chamber equipped with the Voyantic Tagformance measurement system. To emulate realistic on-metal deployment conditions, the completed tag was centrally mounted on a 200 mm × 200 mm metal plate. The measurement setup, shown in Figure 4.13(a), the tag under test, incorporating the NXP UCODE 9 microchip, was positioned on a motorized turntable to facilitate angular scanning during radiation pattern measurements.

A linearly polarized reader antenna with a gain of 8 dBi (G_r) was used to transmit radio waves to activate the RFID microchip embedded in the tag while simultaneously receiving the backscattered signal for performance evaluation. During the measurements, the distance between the reader antenna and the tag (d) was fixed at 52 cm and maintained constant throughout the test. The transmitted power (P_{tx}) was then gradually increased until the tag was successfully activated, and the corresponding activation threshold was recorded. This fixed-distance, variable-power measurement approach is widely adopted by the RFID research community as a site-independent benchmark for evaluating tag performance. Figure 4.13(b) provides a detailed depiction of the measurement setup inside the Voyantic anechoic chamber, highlighting the tag, reader antenna, and turntable arrangement.



(a)



(b)

Figure 4.13 (a) Tag Prototype Mounted on A Centre 200 mm × 200 mm Metal Plate (b) Measurement Setup in The Voyantic Anechoic Chamber.

The simulated realized gain is determined to be 0.858 dBi at 916 MHz, as shown in Figure 4.14, while the measured realized gain is –0.411 dBi at 918 MHz. The slight discrepancy between the simulated and measured frequencies can be attributed to fabrication tolerances, material imperfections, and minor misalignments introduced during the folding process of the tag antenna. Despite this, the measured frequency closely aligns with the simulated value, validating the design's accuracy.

Figure 4.15 (a) and (b) present the measured read patterns of the tag antenna at 918 MHz in the *xy*-, *xz*-, and *yz*-planes, obtained using the maximum permissible 4W EIRP (Effective Isotropic Radiated Power) of transmitted power. The read pattern in the *xy*-plane was generated by rotating the tag around the z-axis, which also allows for identifying the tag antenna's polarization characteristics. Subsequently, the read patterns in the *yz*- and *xz*-planes were obtained by rotating the tag around its *x*-axis and *y*-axis, respectively.

As shown in Figure 4.15 (a), the tag antenna achieves a maximum read distance of 16 m at ϕ = 320° and ϕ = 140°, confirming its linear polarization. Figure 4.15(b) depicts the read patterns in the *xz*- and *yz*-planes. In the *xz*-plane, the maximum read distance of 16 m is observed at an angle of 40°, indicating a strong directional response in this plane. In the *yz*-plane, the read distance reaches a maximum of 12 m within the angular range of 15° to 25°, demonstrating a slightly narrower beamwidth than the *xz*-plane. These results highlight the tag antenna's directional characteristics and sensitivity to orientation, which are critical factors in optimising read performance for practical RFID applications.

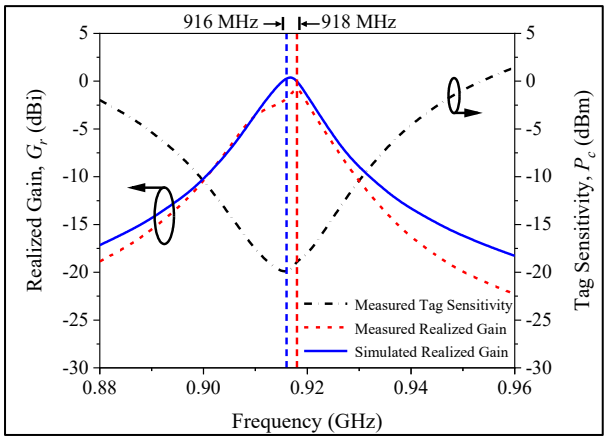
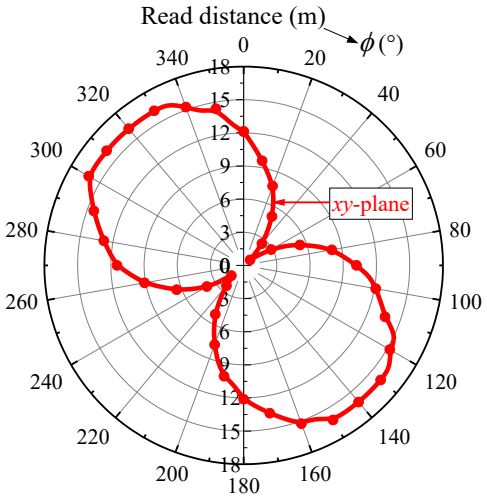
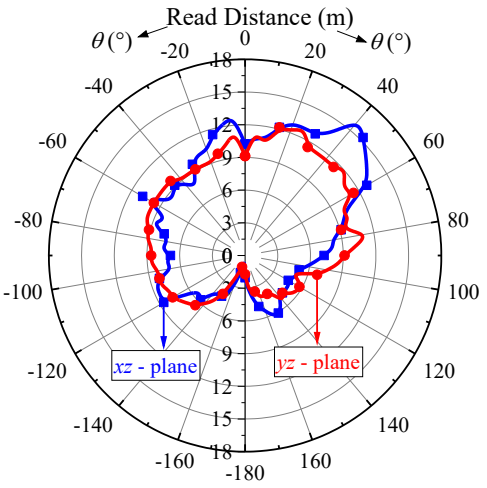


Figure 4.14 Comparison Simulated and Measured Realised Gain of The Fabricated Tag Along with The Measured Tag Sensitivity.



(a)



(b)

Figure 4.15 Measured Read Distances in the (a) *xy*-plane (b) *xz*- and *yz*-planes At the Frequency Of 918 MHz

Figure 4.16 (a) and (b) illustrate the simulated and measured realized gains of the tag antenna in the *yz*- and *xz*-planes, respectively. In the *yz*-plane, as shown in Figure 4.16(a), the maximum realized gain is observed at θ=25°, with simulated and measured values of 0.452 dBi and –0.51 dBi, respectively. Similarly, Figure 4.16(b) illustrates the realized gain in the *xz*-plane, where the simulated and measured results also demonstrate good agreement. The close agreement across both planes validates the design's accuracy and measurement reliability, with minor discrepancies attributed to fabrication tolerances, material variations, or measurement uncertainties. This consistency confirms the antenna's reliability and expected performance.

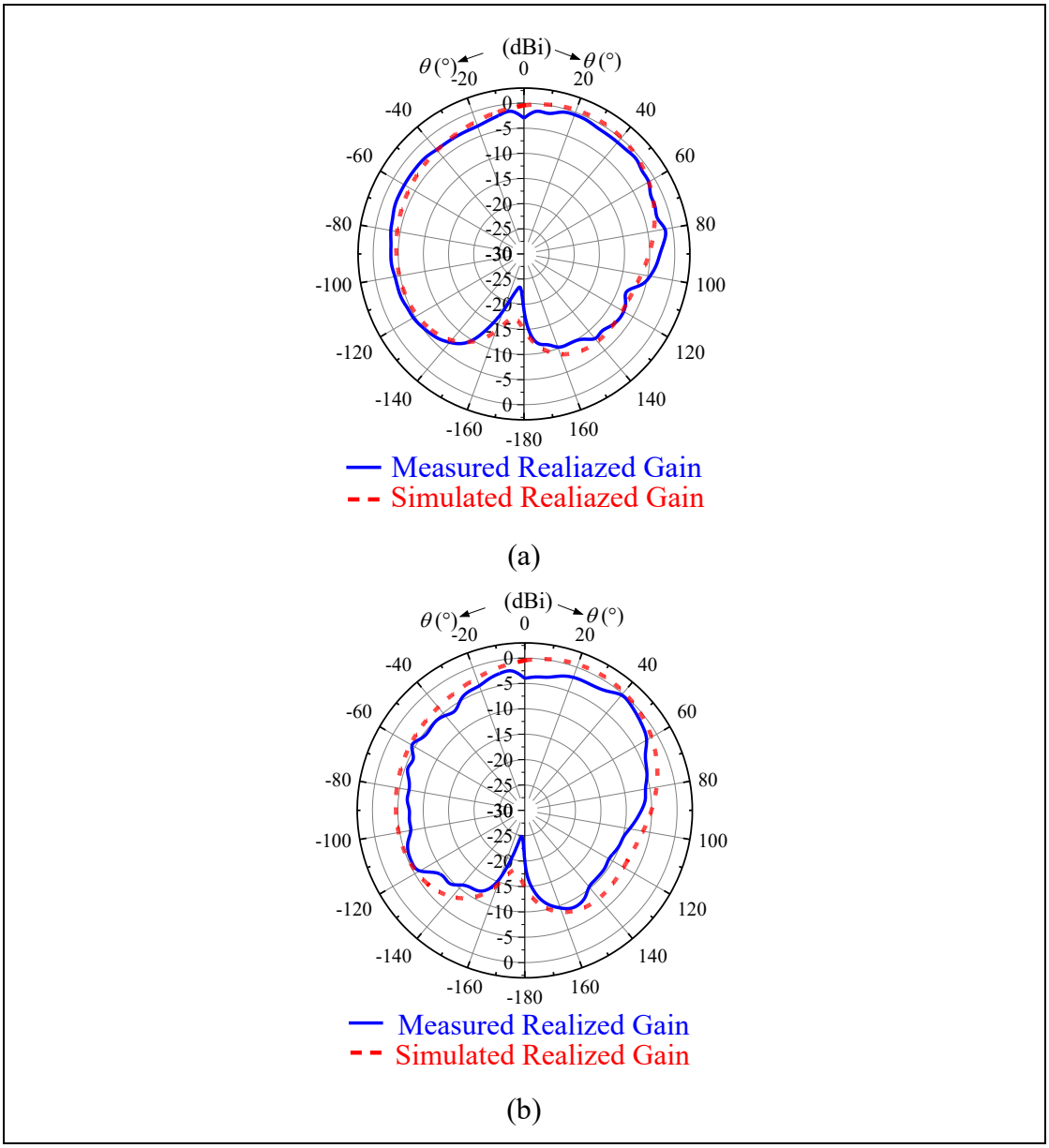


Figure 4.16 Simulated and Measured Realized Gain in the (a) *yz*-plane and (b) *xz*-planes At the Frequency Of 918 Mhz.

To further evaluate the robustness of the tag prototype for on-metal applications, the tag was tested on metal plates of varying dimensions ($Wp \times Lp$). The prototype was positioned at the center of each plate during the measurements, and the read range was measured in the z-direction. Figure 4.17(a) illustrates the read distances for various Lp values while maintaining a fixed Wp of 20 mm. Similarly, Figure 4.17(b) shows the read distances for various Wp values while keeping Lp constant at 20 mm. The maximum read distances remain stable in all cases, ranging between 15.5 m and 16.1 m, demonstrating the tag's consistent performance across different plate sizes. Additionally, the tag's resonant frequency shows minimal variation, indicating that changes in the plate dimensions have a negligible impact on its operating frequency.

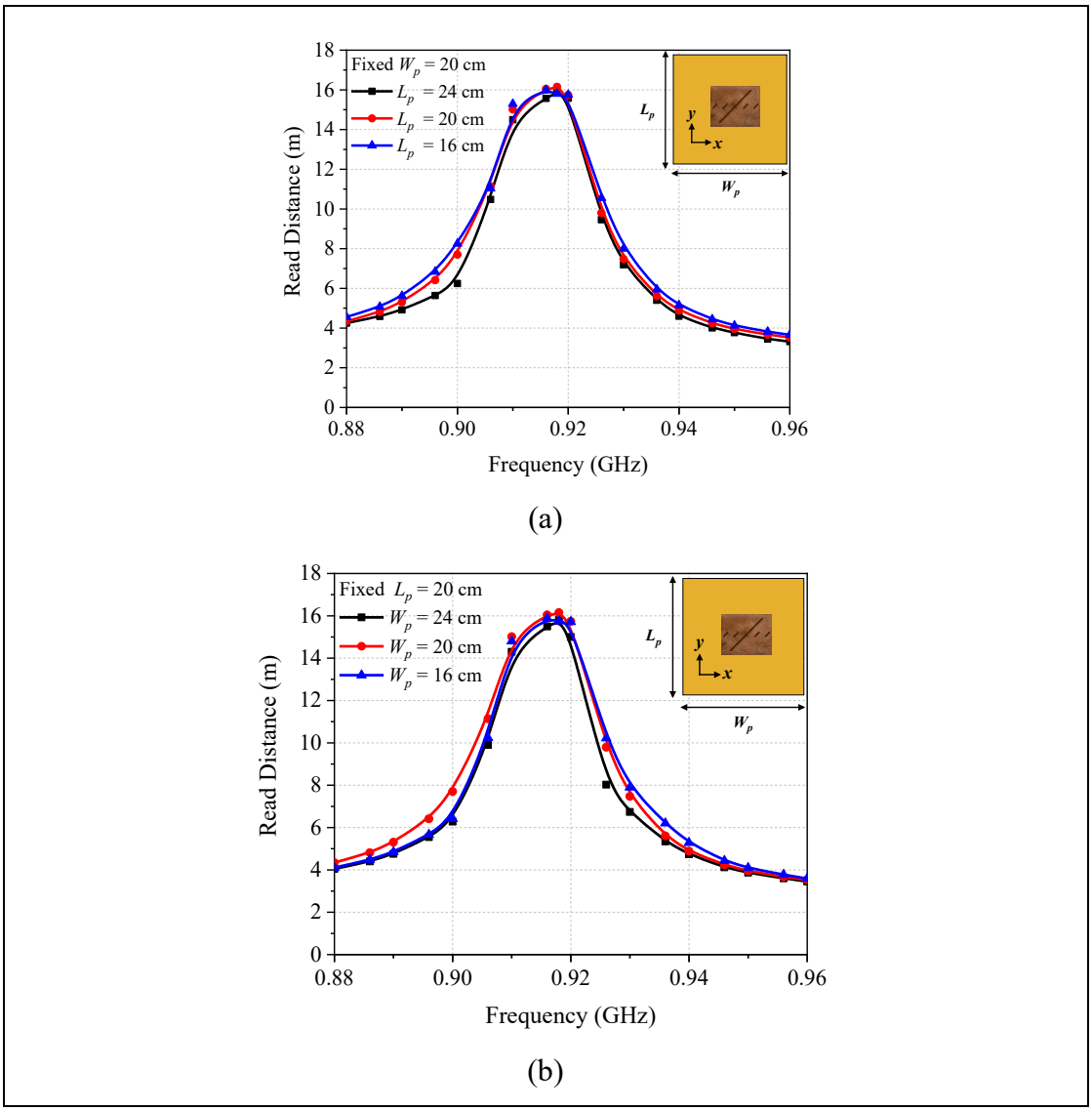


Figure 4.17 Measurement of Read Distances at Various (a) L_p and (b) W_p.

To further validate the tag's robustness, it was mounted to the base and body of several metallic household products, as shown in Figure 4.18(a) and (b). The maximum read distances achieved in these scenarios are summarized in Figure 4.19. When attached to the base of a Milo powder container with a diameter of 15.5 cm, the tag achieves a maximum read distance of approximately 15 m. Similarly, when placed on the body and base of Jacob's container with a volume of 57.92 cm^3, the tag achieves read distances of 14 m and 13 m, respectively. Additionally, the tag can be read at 12 m when attached to the body of a Munchy's biscuit container. Notably, the operating frequency of the tag remains stable across all scenarios, demonstrating its resilience to variations in the backing object's size and shape. These results highlight the tag's robustness and suitability for on-metal applications, as it maintains consistent read distances and stable operating frequencies regardless of the underlying metal surface or object.



(a)



(b)

Figure 4.18 Placement of The Tag on Various Household Items: (a) Base And (b) Body.

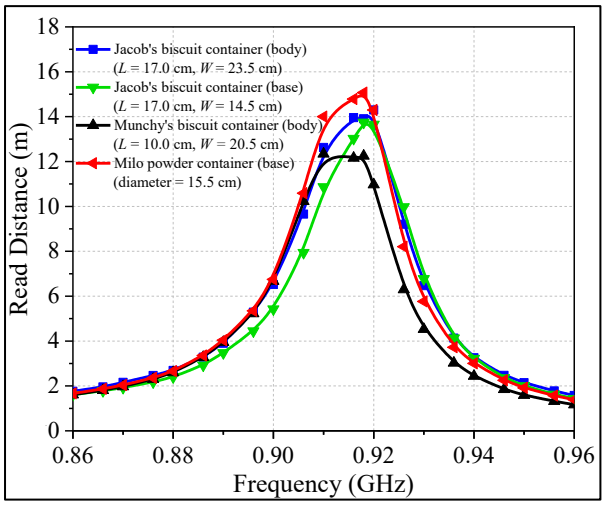


Figure 4.19 Measurement of Read Distances on Various Metallic Household Products.

A comparative analysis in terms of performance between the tag antenna and several recently published on-metal patch-type tag antennas is presented in Table 4.3. In (Sun et al., 2017), a folded tag antenna with an offset feeder was designed to mitigate the effects of metallic surfaces. While effective in reducing metallic interference, this design suffers from a large footprint. The tag proposed in (F.-L. Bong et al., 2018) utilizes two orthogonal dipolar patches with four tuning stubs, enabling installation on metallic surfaces while maintaining compactness. However, its detection range remains limited to 2–3.5 m across different metallic and dielectric surfaces.

A miniaturized folded dipolar tag with meandered slots was introduced in [6], achieving a read range of 4.5 m on metal surfaces with 4 W EIRP. Similarly, [7] proposed a semi-flexible tag antenna embedded with multiple slots for tracking miniature metallic objects. Still, its read range was restricted to 5 m. Although the designs in (F. L. Bong et al., 2017) and (Thirappa et al., 2019) are compact, the incorporation of slots degrades their Q-factor, resulting in significantly shorter read distances (< 10 m) compared with the present design.

Additionally, the folded-patch tag antenna in (Zhao et al., 2023), which includes four etched slots, also exhibits a substantially larger footprint while achieving a maximum read distance of only 7.29 m in metallic environments.

In contrast, the tag antenna developed in this work incorporates embedded inductance, enabling compactness without compromising the Q-factor. As a result, it achieves the longest read distance among the compared designs, demonstrating superior performance in metallic environments.

Table 4.4
Comparative Analysis of On-Metal Patch-Type Tag Antennas and the Tag Presented in this Study

Reference	Power EIRP (W)	Chip Sensitivity (dBm)	Tag Dimension (λ)	Metal Plate Size (cm)	Read Distance (m)
This work	4	–20.85	0.097λ × 0.122λ × 0.010λ	20 × 20	16
(Sun et al., 2017)	3.2	–18.5	0.30λ × 0.01λ × 0.004λ	23 × 15	8
(F.-L. Bong et al., 2018)	4	–17.4	0.09λ × 0.09λ × 0.004λ	20 × 20	3.5
(F. L. Bong et al., 2017)	4	–17.4	0.07λ × 0.04λ × 0.004λ	20 × 20	4.5
(Thirappa et al., 2019)	4	–20	0.07λ × 0.02λ × 0.009λ	20 × 20	5
(Zhao et al., 2023)	4	–21.85	0.152λ × 0.152λ × 0.003λ	20 × 20	7.3

4.5 Summary

Chapter 4 presented a comprehensive analysis of a novel radio frequency identification (RFID) folded-patch tag antenna designed with a double-layered configuration and embedded inclined slots for on-metal applications. The inclined slots act as an effective tuning mechanism, enabling precise control of both the operating frequency and antenna reactance. This approach allows the operating frequency to be efficiently adjusted within the ultra-high frequency (UHF) band, while the reactance can be matched to the chip impedance without necessitating any structural changes to the antenna. The tag antenna achieves a compact size of 32 mm × 40 mm × 3.35 mm (0.097λ × 0.122λ × 0.010λ) and can be fabricated on a single side of a thin polyimide substrate using a low-cost chemical etching process, highlighting its practicality and manufacturability.

The antenna exhibits excellent performance, recording a far-read distance of 16 m under an effective isotropic radiated power (EIRP) of 4 W. This result reflects the effectiveness of integrating inclined slots as a tuning mechanism while preserving compact geometry. Moreover, the operating frequency remains stable across variations

in the size of the underlying metallic surface, demonstrating effective mitigation to detuning effects and confirming its suitability for deployment in diverse real-world industrial environments.

Nonetheless, several limitations identified in this study provide opportunities for future research. The optimization of the embedded slots, which is essential for achieving the desired tuning behavior and near-perfect conjugate impedance matching, requires careful parametric optimization and is computationally intensive. Furthermore, the measured antenna performance is slightly lower than the simulated results, primarily due to fabrication tolerances introduced during the manual folding process. Since the antenna structure is folded manually, slight variations in the folding angle, alignment, and spacing between the folded layers may occur, resulting in deviations from the optimized design dimensions. These fabrication imperfections can alter the current distribution and input impedance of the antenna, leading to slight degradation in realized gain, impedance matching, radiation characteristics, and consequently, the achievable read range. Future work may therefore focus on adopting advanced fabrication techniques to reduce such misalignments and enhance the repeatability of the design, addressing the fabrication-related limitations identified in Chapter 4.

CHAPTER 5
DEVELOPMENT OF AN ANTI-METAL DIPOLAR TAG ANTENNA INCORPORATING A HUYGENS' META ELEMENT FOR GAIN ENHANCEMENT

5.1 Introduction

Chapter 5 presents the design, simulation, and experimental validation of a novel dipolar RFID tag antenna integrated with a Huygens' meta element (HME) for on-metal UHF applications. The core contribution of this work lies in the first implementation of a Huygens' surface within an RFID tag antenna.

This chapter also addresses the fabrication-related limitations identified in Chapter 4, where deviations between simulated and measured, results were attributed to misalignment caused by the manual folding process. To overcome this issue, a folding-free tag design is proposed to improve fabrication accuracy and minimize performance discrepancies.

Subsection 5.2 presents the design and analysis of a broadband Huygens' meta element (HME) developed to enhance the radiation characteristics of the tag antenna. The unit cell is simulated under periodic boundary conditions to model its electromagnetic behavior accurately. This subsection begins by examining the standalone performance of the HME, providing a comprehensive analysis of its operational principles and underlying electromagnetic mechanisms.

Section 5.3 describes the integration of the Huygens' meta element (HME) with a conventional dipolar patch antenna to form the proposed RFID tag. The dipolar patch RFID was chosen for its simplicity, symmetry, and ease of design, making it an ideal platform to evaluate the feasibility and performance impact of HME integration. As the first application of a Huygens' surface in an RFID context, this section outlines the final prototype and explains the working mechanism of the integrated structure.

Section 5.4 presents the performance evaluation of the HME-integrated tag under various test conditions. The tag's far-field read range, gain, and impedance characteristics are examined to validate the effectiveness of the HME integration. Its robustness is further assessed through placement on metal plates of different sizes and various metallic household items to simulate real-world use cases. The consistent

performance and minimal deviation across different environments confirm the reliability and practicality of the proposed design for on-metal RFID applications.

5.2 Design and Analysis of Broadband Huygens' Meta Element

This section presents the design methodology and electromagnetic analysis of the broadband Huygens' meta element. The investigation begins with the configuration and structural development of the unit cell, followed by a comprehensive evaluation of its reflection and transmission responses, including both magnitude and phase characteristics. To verify the Huygens' behaviour, the electric surface admittance and magnetic surface impedance are extracted and analysed. In addition, the surface current distribution is examined to provide deeper insight into the underlying operating mechanisms of the Huygens' surface.

5.2.1 Configuration of the unit cell

The Huygens unit cell, illustrated in Figure 5.1 (a) and (b), consists of metallic patterns printed on both the top and bottom layers of a dielectric substrate. Each layer incorporates an antisymmetric square split-ring resonator (SRR), designed to generate the required electromagnetic response for Huygens' operation. The two conductive layers are separated by a dielectric substrate that determines the overall resonant characteristics of the structure and supports the miniaturized configuration of the unit cell.

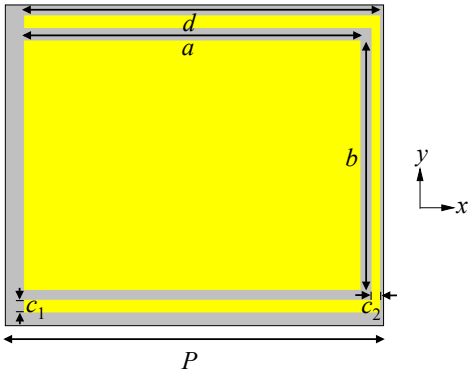
Rogers RT-6010 is selected as the substrate material due to its high dielectric constant ($\varepsilon_r = 10.6$) and low loss tangent ($tan\ \delta = 0.0023$). The high permittivity supports substantial wavelength reduction, enabling a compact unit cell design suitable for operation within the 860–960 MHz UHF RFID band. The substrate thickness is 0.635 mm, providing an appropriate separation between the metallic layers to achieve the desired coupling effect necessary for balanced Huygens behaviors.

The conductive layers are fabricated using copper cladding with a thickness of 0.035 mm, ensuring good conductivity and minimal resistive losses. The antisymmetric split-ring design enhances magnetic and electric dipole interactions, supporting the Huygens' principle for near-field manipulation and wavefront control.

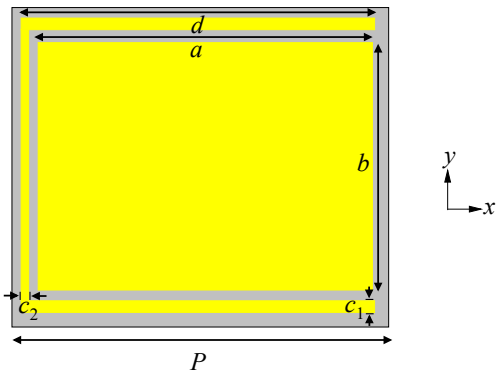
The unit cell features a periodicity (P) of 50 mm to ensure operation within the target frequency range. To characterize its electromagnetic response, the unit cell is

simulated in CST Microwave Studio using periodic boundary conditions (PBC) and Floquet port excitation, as shown in Figure 5.1(c). The PBC models the unit cell as part of an infinite periodic array, thereby eliminating edge effects and enabling the intrinsic electromagnetic response of the unit cell to be accurately characterized under ideal periodic conditions.The Z_{min} and Z_{max} boundaries are assigned as Floquet ports to launch uniform plane waves onto the unit cell. This configuration enables accurate extraction of the transmission (S_{21}) and reflection (S_{11}) coefficients, thereby facilitating the characterization of the unit cell's scattering behavior and evaluates its suitability for metasurface applications.

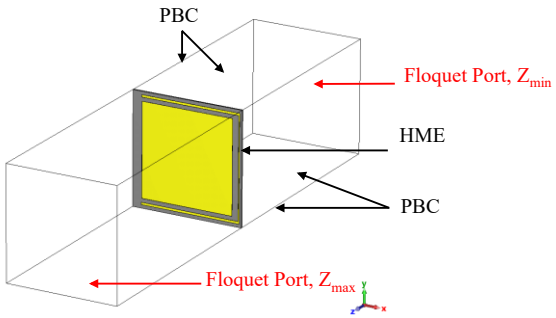
The PBC based unit cell characterization serves as a preliminary step to evaluate the electromagnetic characteristics of the Huygens' meta element and investigate the feasibility of applying the Huygens' metasurface concept to enhance the performance of a compact RFID tag antenna. After optimization, only a single Huygens' meta-element is integrated into the proposed RFID tag antenna for full-wave simulation and fabrication, demonstrating the practical implementation of the concept while maintaining a compact antenna profile.



(a)



(b)



(c)

Figure 5.1 Huygens' Unit Cell Configuration Showing (a) The Top View And (b) The Bottom View, and (c) The Simulated Model Used for Electromagnetic Analysis.

5.2.2 Reflection (Magnitude) and Transmission (Magnitude and Phase) Characteristics of the Huygens' Meta Element (HME)

The electromagnetic behaviour of the unit cell was initially examined by simulating configurations containing only the top Huygens' Meta Element (HME) layer, followed by a configuration containing only the bottom layer. The corresponding S_{11} and S_{21} magnitude responses for these cases are presented in Figure 5.2. A transmission notch is observed at 740 MHz, where the S_{21} magnitude reaches −40.42 dB. This indicates that the single-layer configurations operate in a reflective mode and do not satisfy the required transmission characteristics.

Subsequently, the unit cell was simulated with both HME layers etched on the top and bottom surfaces of the substrate. The reflection and transmission characteristics of the complete HME structure are shown in Figure 5.3 and Figure 5.4.The unit cell exhibits a wide operational bandwidth, with the −10 dB reflection threshold extending from 815 MHz to 952 MHz. This broad passband demonstrates the capability of the HME to support efficient wave transmission with minimal reflection loss across a wide frequency range.

At the resonant frequency of 868 MHz, the unit cell achieves optimal electromagnetic performance. The reflection coefficient S_{11} reaches a minimum of −39.55 dB, signifying minimal reflection and indicating that the majority of the incident energy is transmitted through the structure. The transmission coefficient S_{21} is measured at −0.09 dB, confirming near-lossless forward transmission and efficient energy transfer. These results verify that the HME-based unit cell operates effectively in transmission mode at the desired UHF RFID frequency range.

Furthermore, the transmission phase response shown in Figure 5.4 spans from −179.6° to 179.3° across the operational bandwidth. This nearly continuous 360° phase coverage highlights the Huygens' unit cell ability to provide full-phase control, a key requirement for advanced wavefront manipulation. Such phase agility enables functionalities including beam steering, wave focusing, gain enhancement, and custom radiation shaping. These characteristics demonstrate the suitability of the HME unit cell for integration into advanced antenna and metasurface designs.

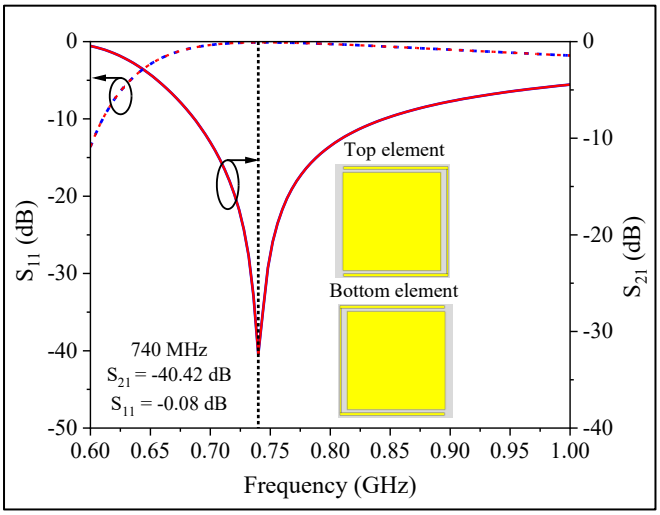


Figure 5.2 Simulated $S_{11}$and S_{21} Magnitude Responses of The Unit Cell with Only the Top and Only the Bottom HME Layers.

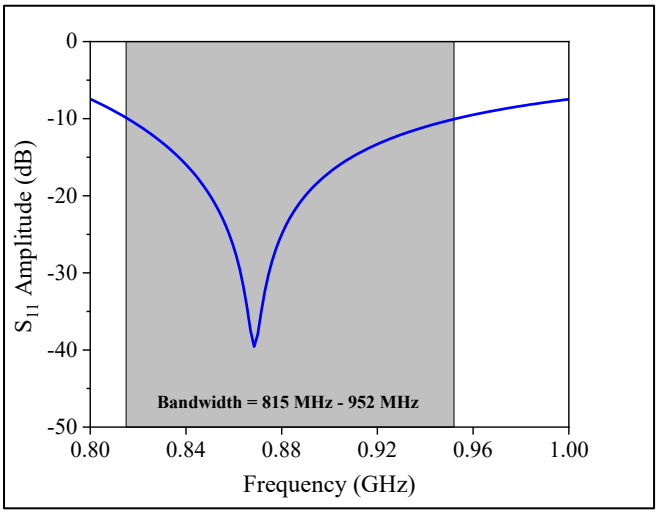


Figure 5.3 Magnitude Curve of S_{11} for the HME with Both Top and Bottom Layers.

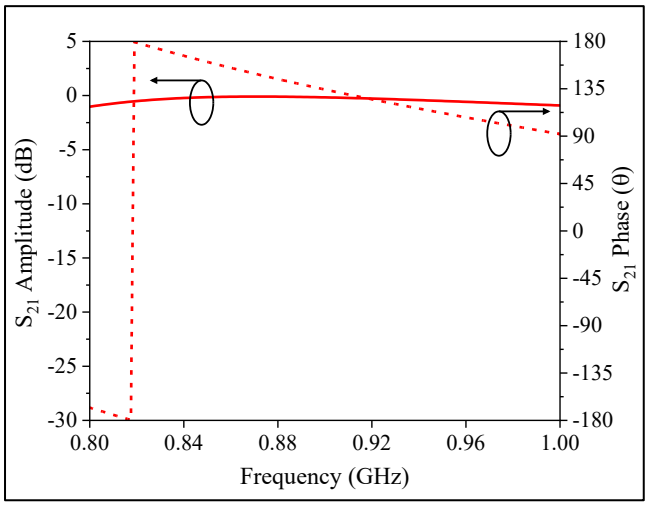


Figure 5.4 Magnitude and Phase Curves of S_{21} for the HME With Both Top and Bottom Layers.

5.2.3 Electric Admittance and Magnetic Impedance Analysis of the Huygens' Meta Element (HME)

The electric surface admittance, Y_{es} and magnetic surface impedance, Z_{ms} of the Huygens' Meta Element (HME) unit cell were extracted to evaluate its electromagnetic behaviour, as shown in Figure 5.5. At the operating frequency of 868 MHz, the electric admittance is obtained as 0.0053+j7.5221, while the magnetic impedance is 0.3281+j7.5223. The real parts of both parameters are minimal and approaching zero, indicating negligible resistive losses and confirming the low-loss characteristics of the unit cell.

Crucially, the imaginary parts of the admittance and impedance were nearly identical in magnitude, j7.5221 and j7.5223 Ω, respectively. This near equality satisfies the fundamental condition for reflectionless Huygens' surfaces, where $Y_{es}\eta = Z_{ms}/\eta$ where η is the intrinsic impedance of free space, as defined in Equation (3.18) . This demonstrates that the electric and magnetic responses of the HME are well balanced, enabling the unit cell to function effectively as a Huygens' element.

This theoretical condition is further supported by the S-parameters in subsection 5.2.2. The unit cell exhibits a low reflection coefficient of $S_{11} = -39.55$ dB and a near-unity transmission coefficient of S21 = −0.09 dB, confirming efficient transmission-mode operation with minimal reflection.

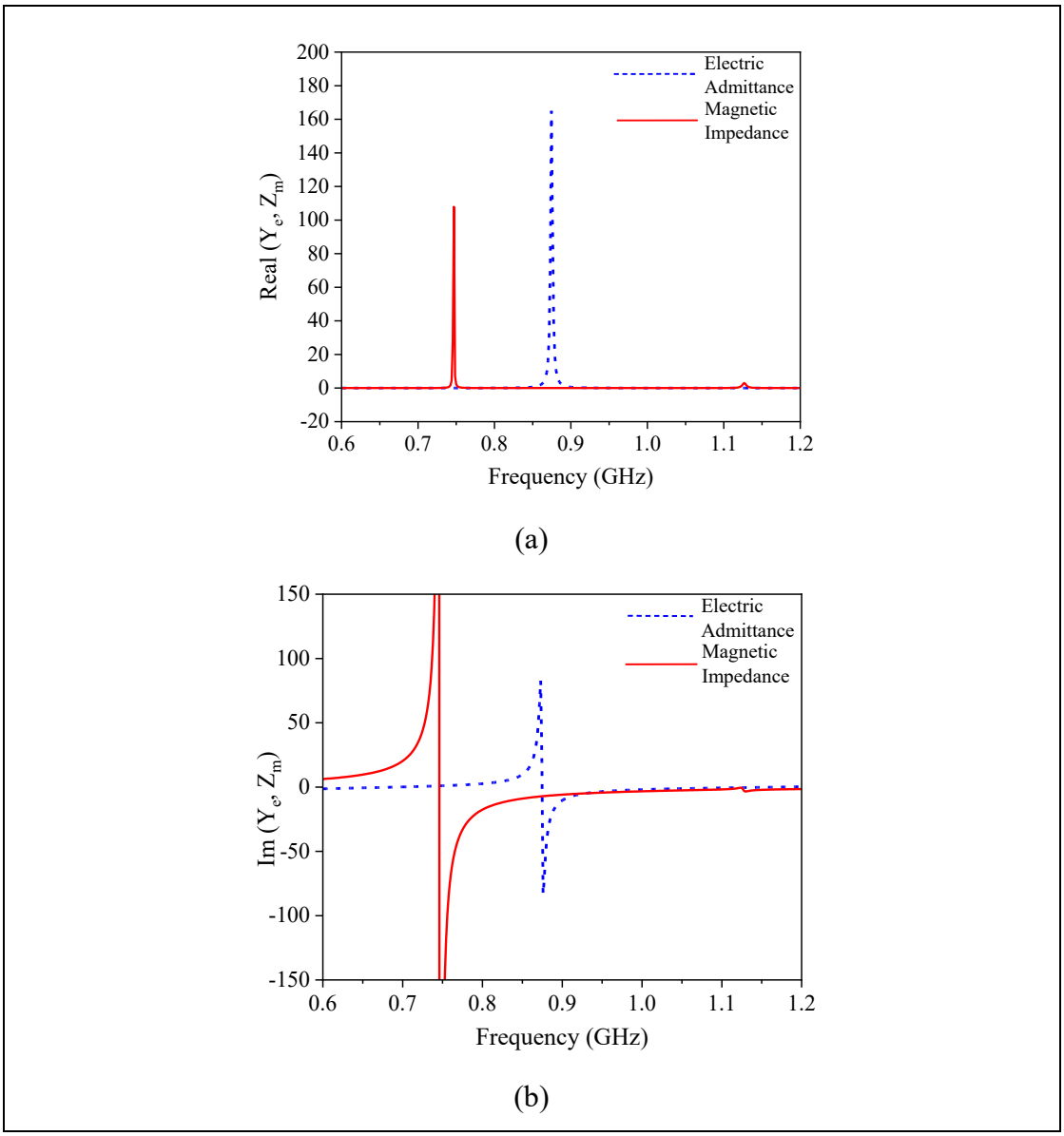


Figure 5.5 Normalized Electric Admittance, $Y_{es}\eta$ And Magnetic Impedance, Z_{ms}/η of the HME unit Cell: (a) Real Components And (b) Imaginary Components.

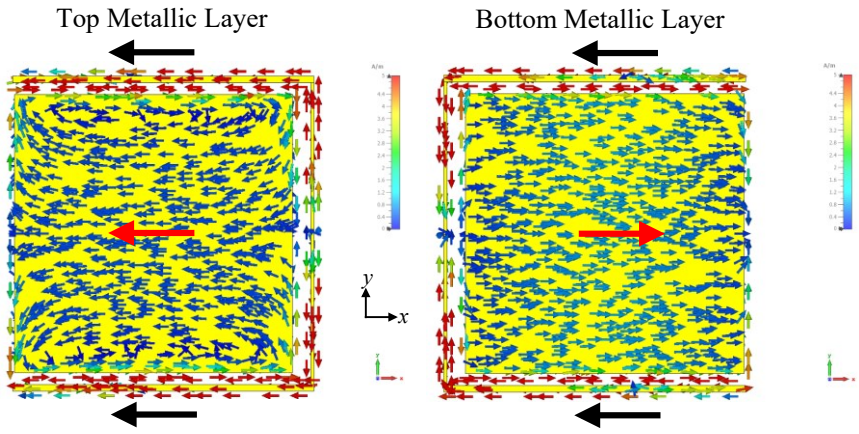
5.2.4 Surface Current Distribution and Behaviour Analysis of the Huygens' Meta Element (HME)

The operational behaviour of the Huygens' Meta Element (HME) is further elucidated through the surface current distribution plots shown in Figure 5.6, which illustrate the induced surface currents on both the top and bottom metallic layers of the unit cell at the resonant frequency of 868 MHz. The current profiles are examined over a single unit-cell period to reveal the underlying electromagnetic mechanisms responsible for Huygens' behaviour.

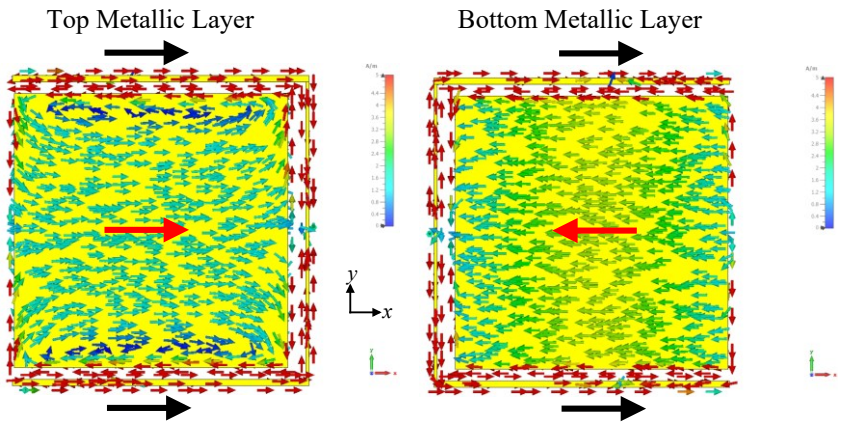
The centre patches on the top and bottom layers exhibit antiparallel current flow, forming a closed-loop current path. This looped current distribution generates the

magnetic dipole response required to satisfy the Huygens' condition. Concurrently, an electric dipole response is produced by the induced currents along the horizontal arms of the structure, oriented in the *x*-direction. These currents are in-phase on both layers, resulting in a constructive electric response along the $_x$-axis.

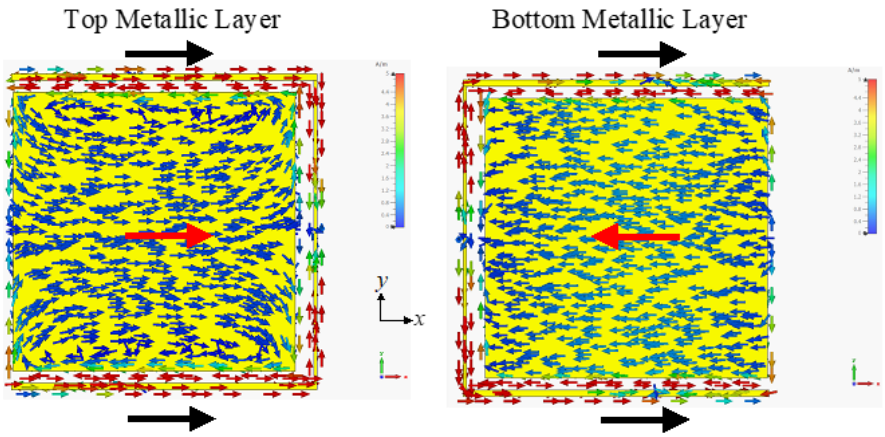
In contrast, the vertical arms oriented along the y-direction carry counter-propagating currents that cancel each other, resulting in negligible contribution to the overall electric response. The concurrent excitation of well-balanced electric and magnetic dipole moments within the same unit-cell period confirms the effective realization of Huygens' resonance at 868 MHz.



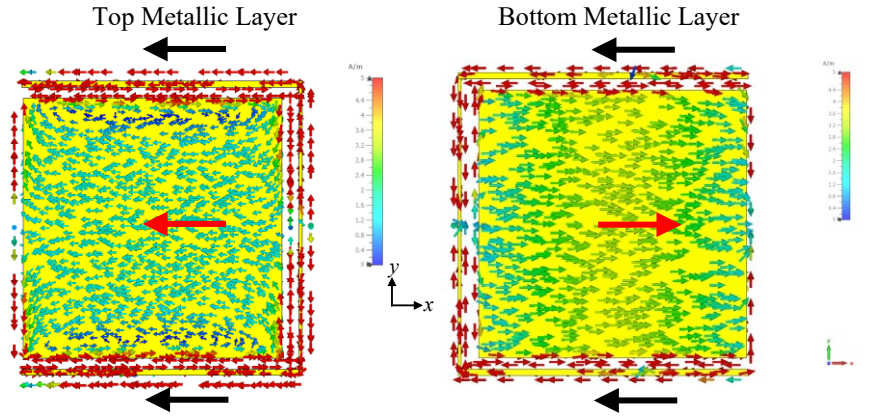
(a)



(b)



(c)



(e)

Figure 5.6 Surface Current Distribution Of The Huygens' Unit Cell On The Top And The Bottom Layers in One Period T at 868 MHz (a) $t = 0$ (b) $t = T/4$ (c) $t = T/2$ (d) $t = 3T/4$.

5.3 Simulation and Analysis Integration of Huygens' Meta-Element (HME) with the Dipolar Patch

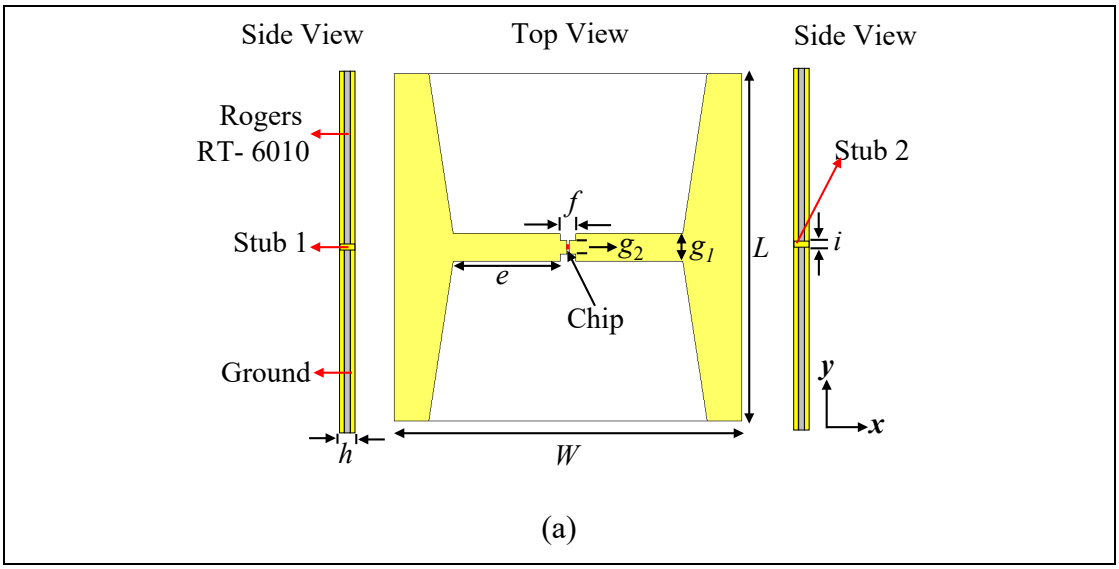
This section presents a detailed explanation of the integration between the embedded Huygens' meta-element (HME) and the dipolar patch antenna. It addresses the configuration and design evolution of the HME-integrated dipolar patch RFID tag, followed by a discussion of its operating principle. Particular emphasis is placed on the resulting gain pattern and magnetic field (H-field) distribution, which together illustrate the influence of the HME on the antenna's overall radiation performance.

5.3.1 Antenna configuration of the HME-Integrated Dipolar Patch

The configuration of the HME-integrated dipolar patch RFID tag is presented in this section, accompanied by the illustrations in Figure 5.7. The antenna was designed, simulated, and optimized using CST Microwave Studio. For both simulation and measurement, the structure was positioned at the centre of a 200 mm × 200 mm to replicate metallic environment scenarios. This section provides a comprehensive description of the antenna configuration, detailing the optimized dimensions and the development process.

Figure 5.7 (a) illustrates the triangular dipolar patch radiator in both top and side views. This patch is printed on Rogers RT-6010 substrate and is bonded to an NXP UCODE 9 RFID microchip, which has a complex input impedance of 10 – j191 Ω and a reading sensitivity of –24 dBm. The dipolar patch is electrically connected to the ground plane through two vertical shorting stubs, as shown in the side-view depiction. The corresponding ground plane used to support on-metal operation is shown in Figure 5.7(b).

All final physical dimensions and optimization parameters used in the fabrication and analysis are summarized in Table 5.1.



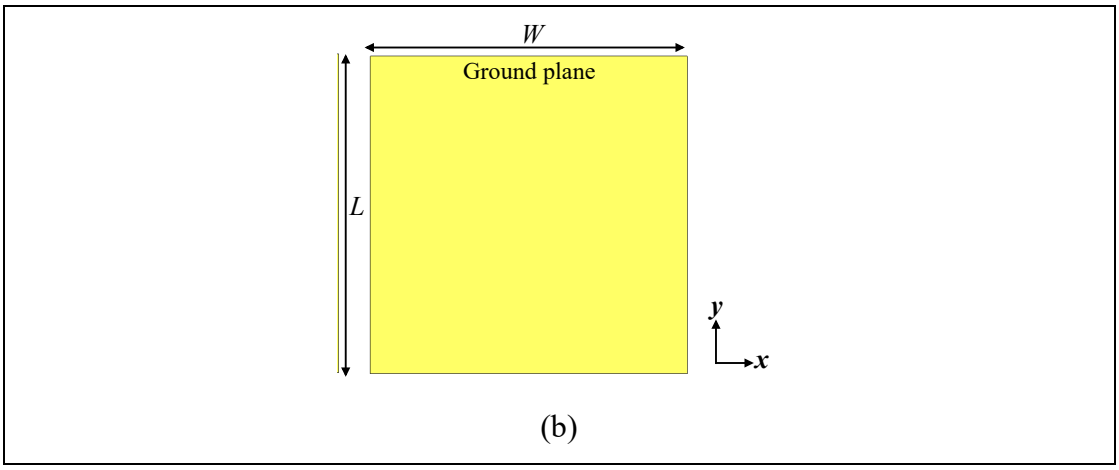


Figure 5.7 (a) Triangular Dipolar Patch Radiator with Top and Side Views; (b) Ground Plane of Dipolar Patch.

Table 5.1
Optimized Design Parameters of the HME-Integrated Dipolar Patch RFID Tag

Parameter	Dimension (mm)	Parameter	Dimension (mm)
a	41.50	g_1	4
b	41.50	g_2	2
c_1	1	h	2.01
c_2	0.50	i	5.20
d	45	L	50
e	15.35	W	50
f	2.30	p	50

5.3.2 HME-Integrated Dipolar Patch RFID: Working Principles and Result Analysis

The Huygens' surface characteristics were initially investigated through the simulation of a single unit cell, as part of the design evolution process. The detailed configuration and electromagnetic behavior of the Huygens' Meta Element (HME) have been comprehensively discussed in Section 5.2. Following this analysis, the HME is further analyzed by integrating it with a dipolar RFID tag structure.

The conventional dipolar tag consists of a pair of triangular patch elements, two vertical shorting stubs, and a full ground plane. This configuration is specifically optimized to operate within the UHF RFID band, and simulations confirm that the dipolar tag resonates at 868 MHz, corresponding to the lower end of the UHF RFID frequency band (LEU).

Subsequently, the HME was integrated onto the top of the dipolar tag to evaluate its effect on the overall antenna performance. The addition of the HME introduces a slight frequency shift, lowering the resonant frequency by approximately 1 MHz. As a result, the integrated structure now operates at 867 MHz, as shown in Figure 5.8. This shift is attributed to electromagnetic coupling between the HME and the underlying dipolar patch, which modifies the effective permittivity and alters the surface current distribution.

Impedance matching performance was examined for both configurations, with and without the HME.As depicted in Figure 5.9, the impedance at resonance is 16.71 + j190.43 Ω for the dipolar tag, and improves slightly to 18.94 + j189.63 Ω following HME integration. These results demonstrate that the integration of the HME introduces minimal detuning while preserving good impedance matching, thereby confirming its compatibility with the dipolar tag and its effectiveness in enhancing antenna performance without compromising resonance characteristics.

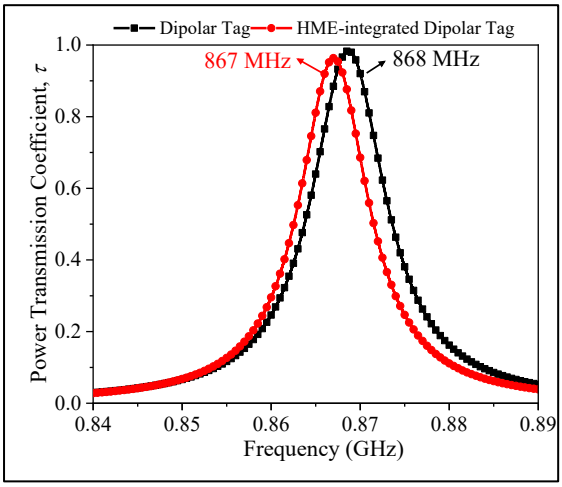


Figure 5.8 Comparison of Power Transmission Coefficients Between the Dipolar Tag and the Dipolar Tag Integrated With HME.

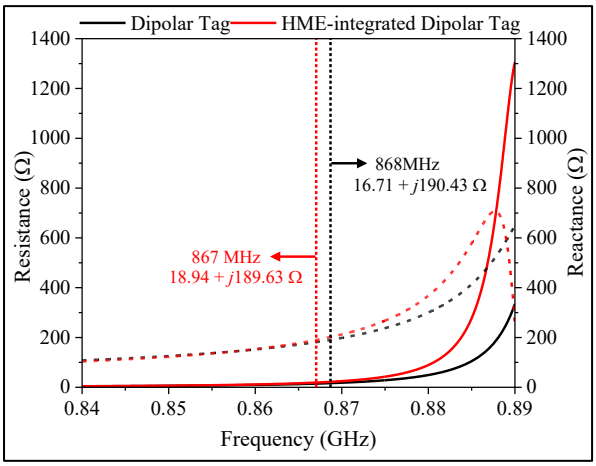
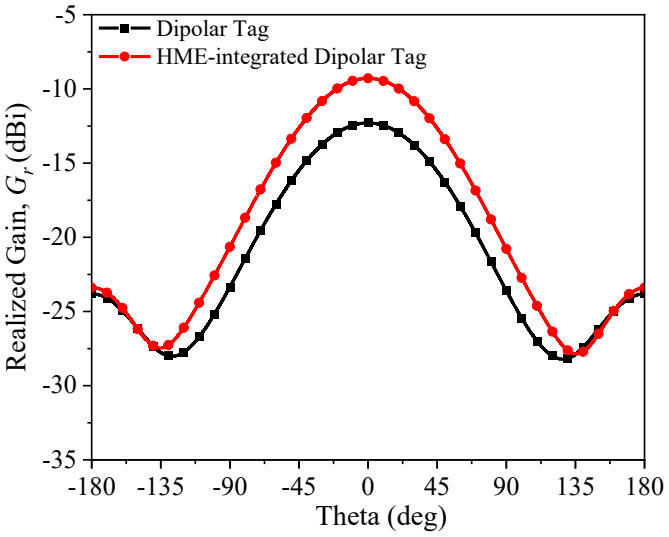


Figure 5.9 Comparison of Antenna Impedances Between the Dipolar Tag and The Dipolar Tag Integrated With HME.

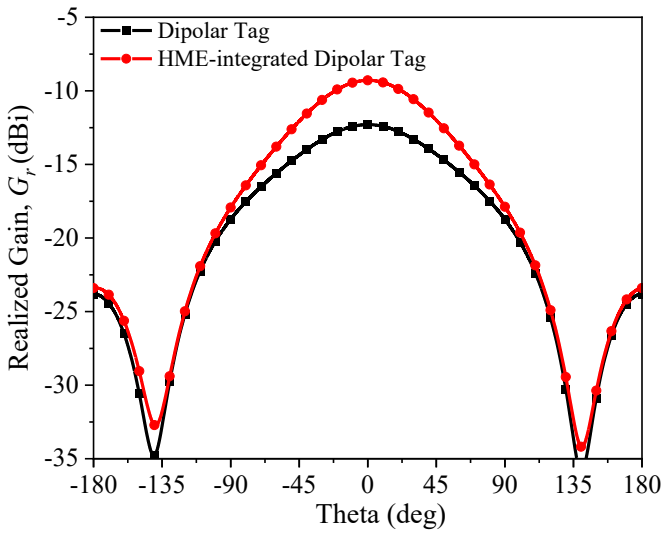
Figure 5.10 illustrates the realized gain of the dipolar patch RFID tag in both the *yz* and *xz* - planes, comparing the performance of the tag with and without the Huygens' Meta Element (HME) integration. For the dipolar patch configuration, the realized gain is observed to be −12.3 dBi. With the incorporation of the HME layer above the dipolar patch, the realized gain increases markedly to −9.28 dBi, corresponding to a gain enhancement of 3.02 dBi. This improvement is attributed to the wave-shaping capability of the HME, which alters the radiation pattern by narrowing the beamwidth, thereby concentrating the radiated power more effectively in the forward direction.

The enhanced directivity introduced by the HME is further confirmed through an examination of the 3 dB beamwidth in both principal planes. In the *yz*-plane, the 3 dB beamwidth reduces slightly from 86.7° to 84.8°, while in the *xz*-plane, the beamwidth exhibits a more substantial reduction, decreasing from 113.8° to 94.7°, a narrowing of 19.1°. These beamwidth reductions indicate a more directive radiation pattern, which directly contributes to the observed gain enhancement.

Importantly, this gain improvement is achieved without introducing significant shifts in the operating frequency or affecting the impedance matching of the tag. The integration of the HME, therefore, not only preserves the original performance characteristics of the dipolar tag but also enhances its radiation efficiency, making it more suitable for RFID applications requiring improved read range and signal strength.



(a)



(b)

Figure 5.10 Simulated Realized Gain Patterns in the (a) *yz*-plane and (b) *xz*-plane

The simulated magnetic field (H-field) distributions for both the conventional dipolar antenna and the dipolar tag integrated with the Huygens' Meta-Element (HME) are shown in Figure 5.11 . With the integration of the HME above the dipolar tag, the magnetic field becomes more uniformly distributed across the antenna surface. This redistribution effectively enlarges the radiating aperture compared to the conventional dipolar configuration, thereby contributing to an increase in antenna gain.

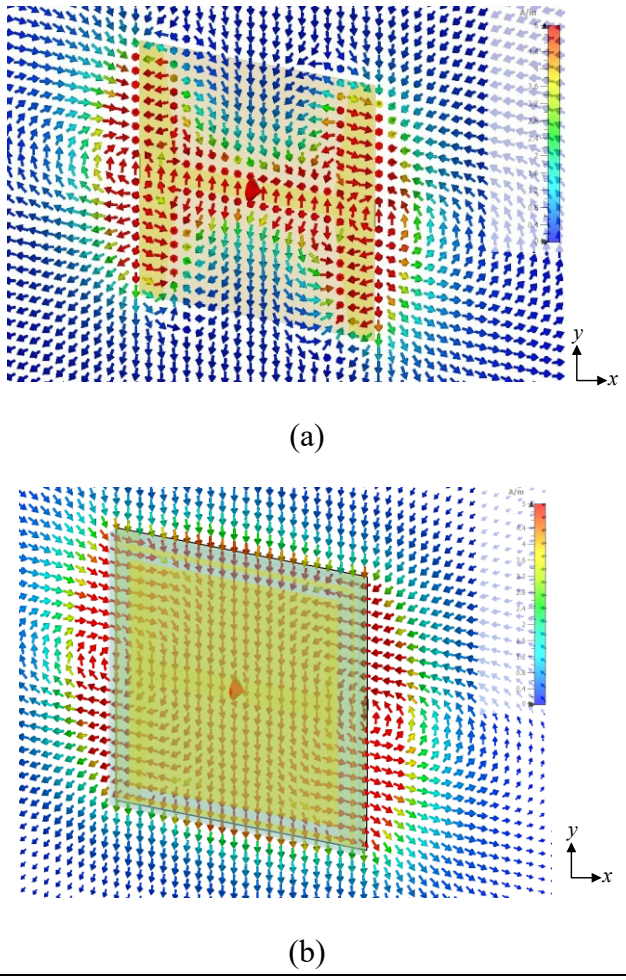


Figure 5.11 Simulated H-Field Distribution at 868 MHz: (a) Conventional Dipolar Tag and (b) HME-Integrated Dipolar Tag.

To gain further insight this effect, the H-field intensity is analyzed at an observation plane located at z = 2.4 mm, as illustrated in Figure 5.12. At this plane, the H-field distribution clearly reveals that the embedding of the Huygens' surface significantly strengthens the radiated field compared to the conventional dipolar tag. The red curve, corresponding to the HME-integrated configuration, exhibits higher peak H-field values of approximately 40.91 A/m, along with a more directive distribution along the x-axis. This corresponds to an increase of 18.28 A/m, representing an improvement of approximately 80% in magnetic field intensity.

Since antenna gain is directly proportional to radiation intensity for a given input power, this substantial enhancement in H-field magnitude confirms that the HME enables more efficient and directional energy radiation. Consequently, the observed increase in magnetic field intensity provides clear electromagnetic evidence of the gain enhancement achieved through HME integration at the specified observation plane.

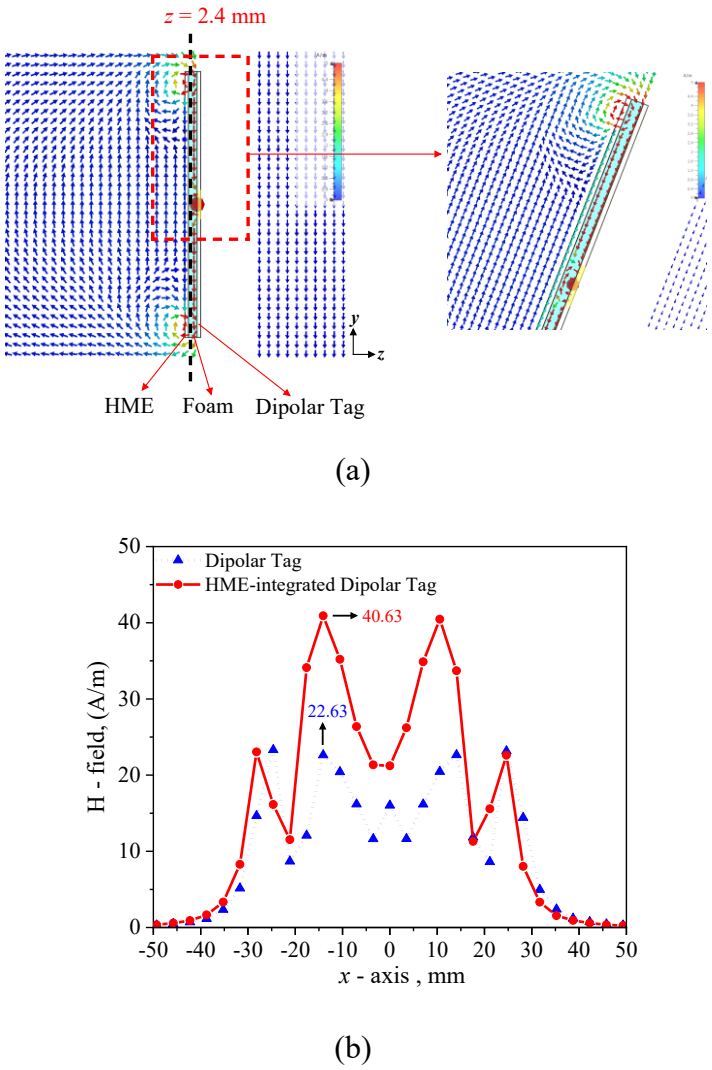


Figure 5.12 H-Field Analysis of the HME-Integrated Dipolar Tag Showing(a) Side-View Distribution And (b) H-Field Magnitude Along the *x*-axis At $z = 2.4$ mm.

5.4 Experimental Validation and Performance Measurement

This subsection presents the fabrication details and experimental assembly of the dipolar patch antenna integrated with the Huygens' Meta Element (HME), forming the basis for subsequent performance validation.

The fabricated dipolar patch antenna is shown in Figure 5.13 (a), while the fabricated Huygens' Meta-Element (HME) is presented in Figure 5.13 (b). The HME is implemented on a separate RT-6010 substrate and is electromagnetically coupled to the underlying dipolar patch without any direct electrical connection to either the patch or the ground plane. This configuration allows the HME to operate purely as a field-shaping structure, enhancing the antenna's radiation characteristics.

A complete view of the antenna assembly process is provided in Figure 5.13(c). The left portion of the figure illustrates the individual fabricated components prior to stacking, namely the dipolar patch layer, the PP4 foam spacer, and the HME layer, while the right portion shows the fully assembled antenna configuration. The low-permittivity PP4 foam spacer (ε_r = 1.06, $tan\delta$ = 0.0001), inserted between the HME and the dipolar patch, establishes the interlayer.

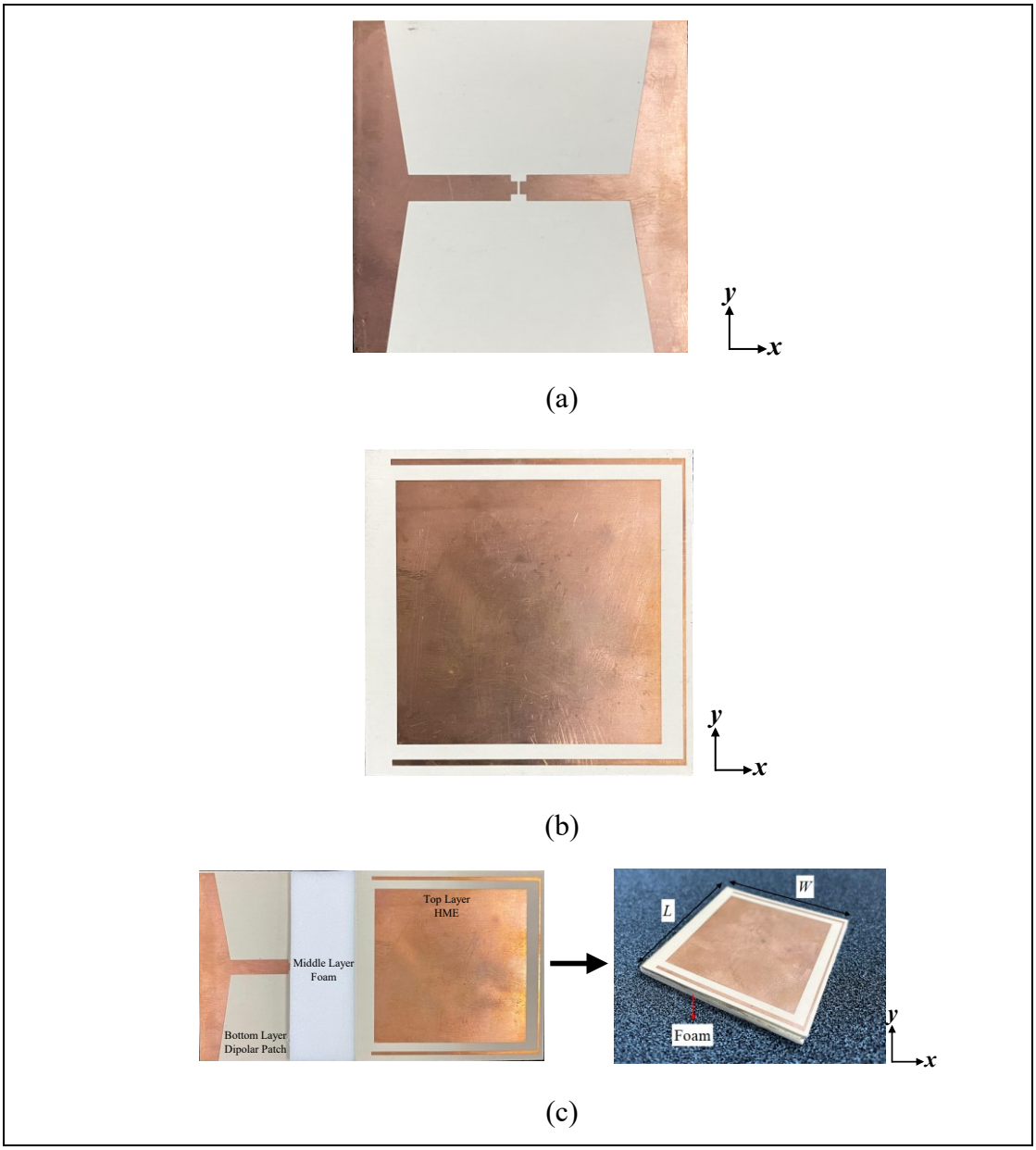
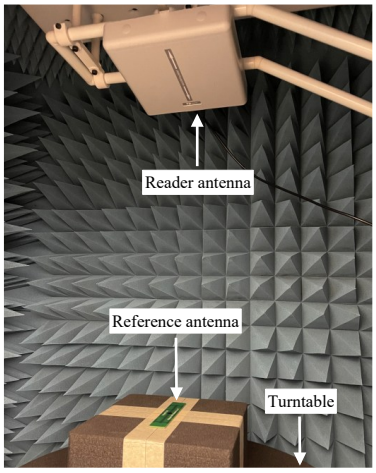


Figure 5.13 Fabricated Antenna Components and Assembly: (a) Dipolar Patch Layer with Shorting Stubs; (b) Huygens' Meta Element (HME); And (c) Fabricated Layers Prior To Stacking (Left) And the Fully Assembled Tag with PP4 Foam (Right).

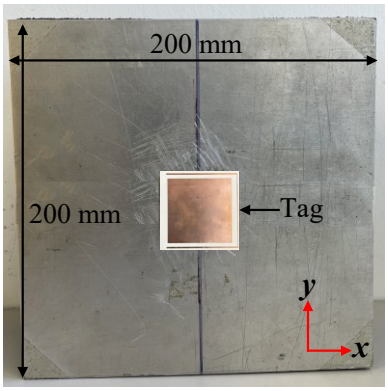
Next, the performance of the tag antennas specifically its read distance, realized gain, and read pattern—was evaluated in a controlled environment using an anechoic

chamber. Measurements were carried out using the Voyantic Tagformance Measurement System, which comprises an integrated reader antenna and a motorized turntable. The measurement procedure began with system calibration using a reference antenna, as illustrated in Figure 5.14(a), to ensure the accuracy and reliability of subsequent measurements.

Following calibration, the reference antenna was replaced with the tag antenna, which was mounted at the center of a 200 mm × 200 mm metal plate, as shown in Figure 5.14(b). The tag was placed on a motorized turntable, enabling angular measurements over different orientation. The tag's microchip was energized by radio waves transmitted from a linearly polarized reader antenna with a gain of 8 dBi, while the backscattered signal from the tag was simultaneously received by the reader. To maintain measurement consistency, the separation distance between the reader antenna and the tag was fixed at 52 cm for all tests. This measurement configuration ensured repeatable and reliable characterization of the tag antenna's performance.



(a)



(b)

Figure 5.14 (a) Measurement Setup Within the Anechoic Chamber. (b) Proposed HME RFID Tag Positioned at The Centre of A 200 mm × 200 mm Metal Plate.

Realized gain and read range are key parameters for evaluating the performance of a passive RFID tag antenna. The realized gain reflects the tag's ability to effectively receive power from the reader and backscatter the modulated signal, while the read range represents the maximum achievable operating distance between the reader and the tag. Figure 5.15 presents the simulated and measured realized gain, together with the measured tag sensitivity, over the frequency range from 840 MHz to 890 MHz.

At 867 MHz, the simulated realized gain is −9.28 dBi, whereas the measured realized gain reaches a peak value of −10.53 dBi at 868 MHz. The slight frequency shift of approximately 1 MHz and the gain deviation of about 1.25 dB are mainly attributed to fabrication tolerances, including etching inaccuracies and minor misalignment between the dipolar radiator and the embedded Huygens' surface structure. Despite these discrepancies, the fabricated tag demonstrates stable operation within the European UHF RFID band (865–868 MHz), confirming reliable performance and suitability for practical deployment RFID applications.

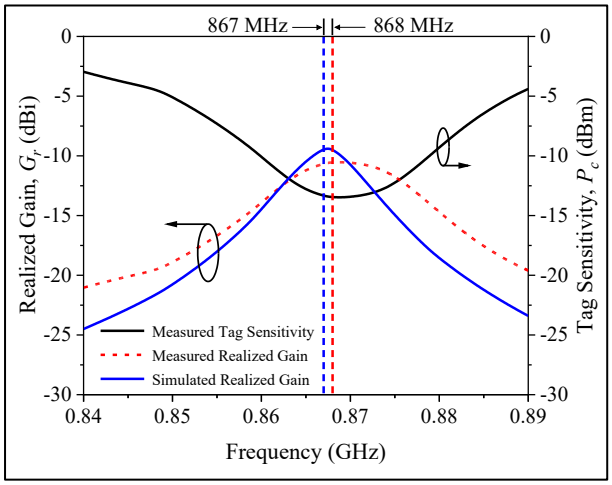


Figure 5.15 Simulated and Measured Realized Gain Alongside Tag Sensitivity Measurements.

The radiation pattern of the tag at 868 MHz was evaluated under a regulated equivalent isotropic radiated power (PEIRP) of 4 W. The read pattern in the xy-plane was obtained by rotating the tag about the z-axis, producing a characteristic figure-eight pattern with peak read distances of approximately 8.23 m at 0° and 180°. This behavior confirms the linearly polarized radiation characteristic of the tag antenna, as illustrated in Figure 5.16(a).

Additional measurements were conducted in the xz-plane and yz-plane by rotating the tag about the y-axis and x-axis, respectively. In both planes, a maximum read range of up to 8 m was achieved at 0°, demonstrating consistent radiation behavior and stable performance across multiple orientations.

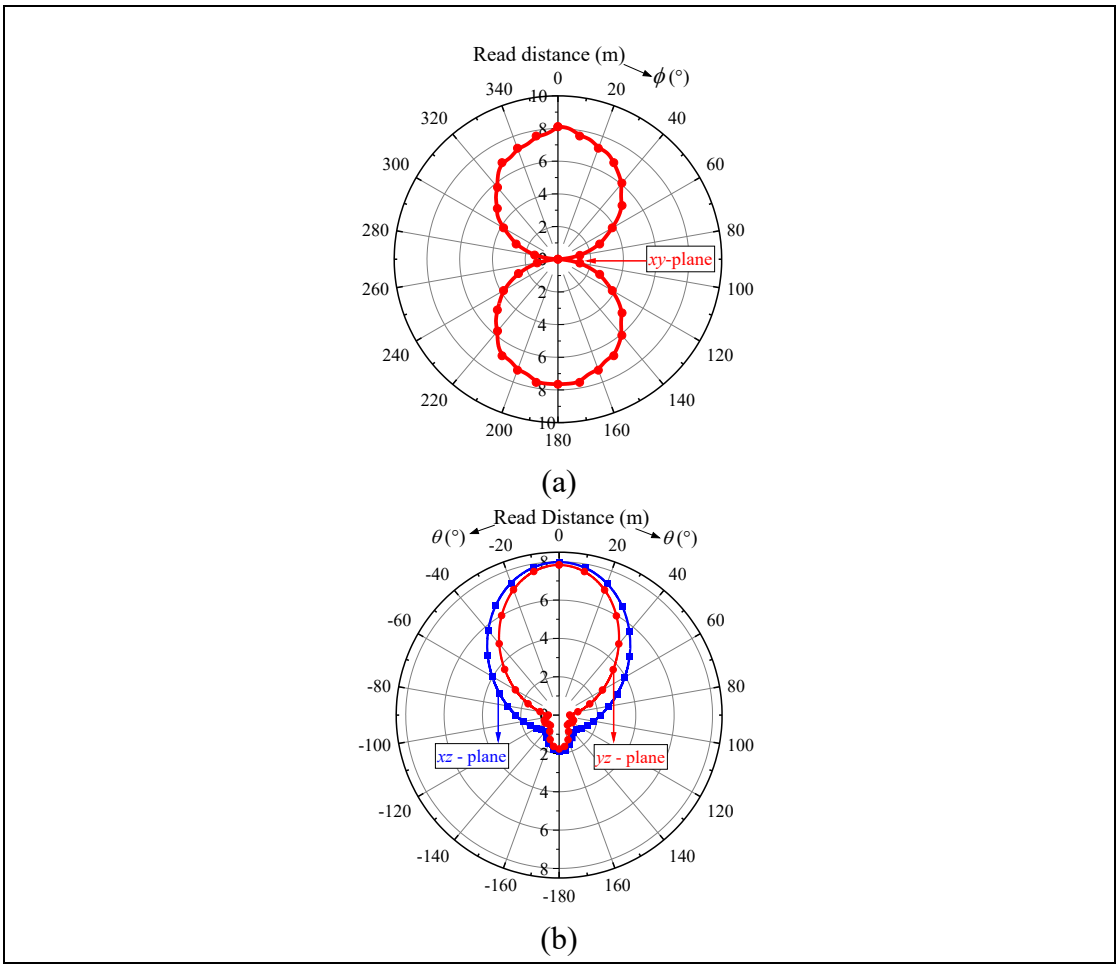


Figure 5.16 Read Pattern Measurements Conducted At 868 MHz in The (a) *xy*-plane, and (b) *xz*- and *yz*-planes.

To evaluate the robustness of the tag antenna for on-metal applications, experiments were conducted using aluminum plates of varying dimensions ($Wp \times Lp$) to simulate real-world UHF RFID deployment scenarios involving different metal surface sizes. During the measurements, the fabricated tag was centrally mounted on each aluminum plate, and the read range was measured along the z-direction using a standard RFID reader configuration over the frequency range of 840–860 MHz, covering the Low-End UHF (LEU) RFID band.

In the first part of the experiment, the length of the plate, *Lp* was varied among three values of 16 cm, 20 cm, and 24 cm, while keeping the width, *Wp,* constant at 20 cm. The corresponding read range results, as presented in Figure 5.17(a), showed that

the tag maintained consistent performance across all three plate lengths, with measured read ranges ranging from 8.23 m to 9.24 m. In the second part, the plate width, *Wp* was varied from 16 cm to 24 cm, while keeping the length, *Lp,* constant. As illustrated in Figure 5.17(b) the tag consistently achieved a read range of up to approximately 8.5 m across the entire LEU RFID band.

Overall, these results demonstrate that the tag's performance is only minimally influenced by variations in the size of the underlying metallic surface, confirming the robustness of the antenna design and its suitability for reliable on-metal UHF RFID applications.

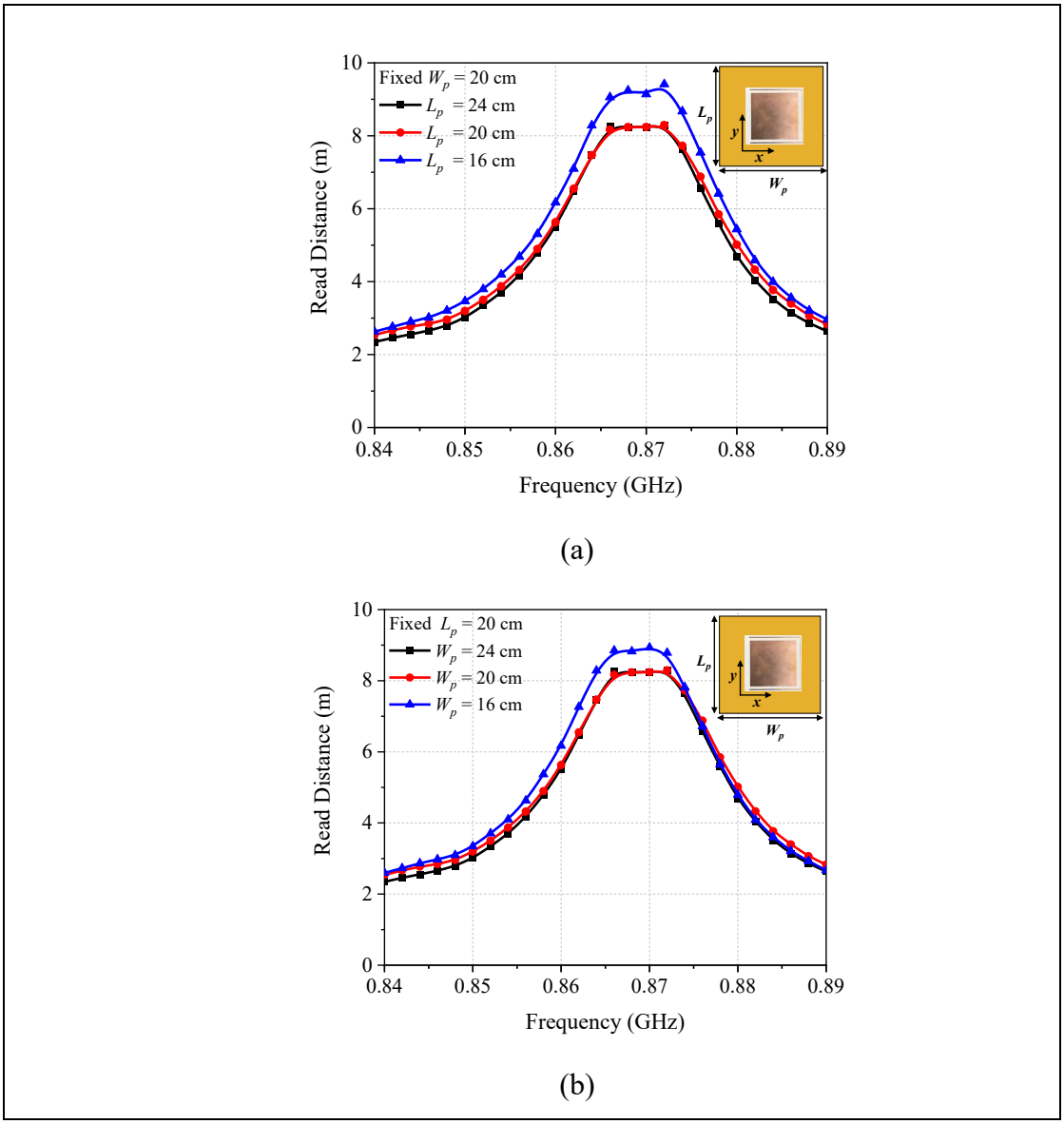
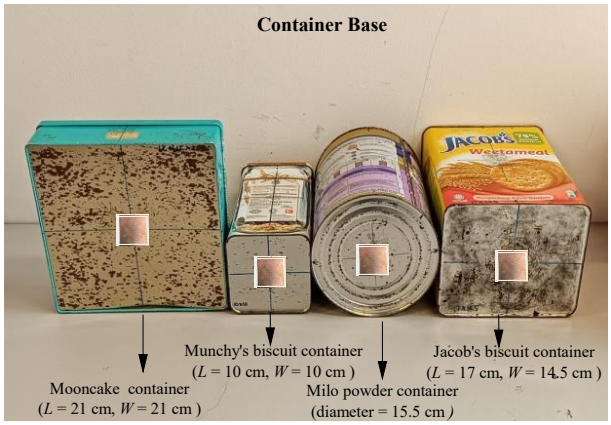


Figure 5.17 Measured Read Range at Different Values of (a) L_p and (b) W_p across the 840–890 MHz Frequency Range.

To further assess the tag's robustness in practical on-metal scenarios, the prototype was mounted on various metallic household items, specifically on both the body and base surfaces, as illustrated in Figure 5.18. The corresponding measured read ranges are presented in Figure 5.19.

When mounted on the base of a mooncake container with an estimated surface area of 4.41 m^2, the tag achieved a maximum read range of approximately 7.3 m. For the Jacob's biscuit container, which has an estimated volume of 57.92 m^3, read ranges of up to 7.7 m were recorded when the tag was attached to both the body and the base surfaces. Similarly, when mounted on a Munchy's biscuit container, the tag exhibited read distances of 8.9 m on the body and 6.9 m on the base. In the case of the Milo powder container, a read range of approximately 7.2 m was achieved when the tag was placed on the base surface.

Overall, the relatively small variation in measured read range indicates that the tag maintains stable and reliable performance across a wide range of metallic objects with differing sizes, shapes, and surface curvatures, demonstrating its suitability for practical on-metal RFID applications.



(a)



(b)

Figure 5.18 Tag Positioning on Various Household Items: (a) Base And (b) Side Body Surfaces.

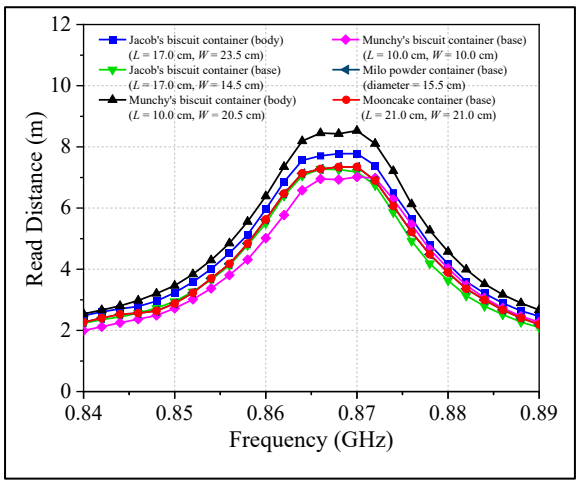


Figure 5.19 Measured Read Range on The Base and Side Surfaces of Various Household Items.

5.5 Summary

This chapter establishes a technical contribution through the design, realization, and validation of a dipolar RFID tag antenna integrated with an embedded Huygens' Meta Element (HME) for on-metal applications. The work directly addresses the fundamental limitations of passive UHF RFID tags operating on metallic surfaces namely impedance detuning, reduced radiation efficiency, and limited read range while preserving a compact and fabrication-friendly structure.

A key contribution of this study is the successful integration of the Huygens' Meta Element (HME) atop a dipolar tag antenna without altering the original antenna footprint. Compared with the conventional dipolar tag antenna without the HME, the

proposed design improves the realized gain from −12.30 dBi to −9.28 dBi, representing a 3.02 dB enhancement through controlled electromagnetic field shaping while maintaining stable impedance matching and the operating frequency. This improvement extends the read range from 6.69 m to 8.23 m, corresponding to a 23.0% increase under a regulated 4 W EIRP condition. Despite its electrically compact size of ($0.1446\lambda \times 0.1446\lambda \times 0.0058\lambda$ mm), the tag demonstrates enhanced radiation performance without increasing the antenna footprint, thereby validating the effectiveness of the HME design for compact on-metal UHF RFID tag applications.

From a practical standpoint, the antenna configuration employs a simple planar configuration that is fully compatible with standard chemical etching processes, enabling low-cost and scalable fabrication. Comprehensive experimental validation including realized gain, read pattern, read range, and robustness tests on metallic plates and real household metal objects confirms close agreement between simulation and measurement, with only minor deviations attributable to fabrication tolerances. This represents a marked improvement over the fabrication-related challenges encountered in Chapter 4.

CHAPTER 6
CONCLUSION

6.1 Conclusion

This research presents the systematic design, analysis, fabrication, and experimental validation of compact passive UHF RFID tag antennas specifically engineered for metallic deployment environments. The growing demand for reliable RFID-based identification systems in logistics, asset tracking, smart manufacturing, and industrial automation requires tag antennas that are compact, platform-tolerant, and capable of maintaining stable radiation performance in the presence of conductive surfaces. However, conventional dipole- and patch-based RFID tags typically suffer from impedance detuning, radiation degradation, and limited read range when mounted on metal.

To address these limitations, this thesis introduced two complementary antenna design strategies. The first involves a folded stacked-patch configuration incorporating embedded inclined slots as a structurally integrated tuning mechanism to achieve compactness and stable impedance matching in metal-mounted conditions. The second strategy integrates Huygens' Meta-Elements (HME) with a dipolar patch radiator to enhance realized gain and radiation directivity without increasing the antenna footprint. Together, these approaches provide a comprehensive solution for improving miniaturization, impedance stability, and radiation performance in passive UHF RFID systems for metallic applications.

6.1.1 Folded Stacked-Patch Tag with Embedded Inductive Slots

The first contribution focuses on antenna miniaturization and impedance tuning through structural integration. A double-layer folded patch configuration was introduced to increase effective capacitance, thereby reducing the electrical size while maintaining resonance within the UHF RFID band. To provide an integrated tuning capability, five inclined slots were embedded within the radiating patch to function as inductive elements.

These slots introduce controlled inductive loading that compensates for the capacitive impedance of passive RFID microchips, improving impedance matching

stability, particularly under metallic mounting conditions. The added inductance lowers the resonant frequency without increasing the physical dimensions of the antenna, enabling compactness while preserving radiation efficiency. Adjustment of the slot parameters allows precise control of operating frequency and input impedance without external lumped matching components.

Parametric investigations confirmed the sensitivity of impedance characteristics to slot geometry, validating the effectiveness of the proposed tuning mechanism. Experimental results further demonstrated stable performance and consistent read range under 4 W EIRP excitation when mounted on metal surfaces, indicating enhanced platform tolerance and structural robustness compared to conventional metal-mountable designs.

6.1.2 Integration of Huygens Meta-Elements for Gain Enhancement

The second major contribution of this thesis is the investigation of Huygens' Meta-Elements (HME) as a gain-enhancement technique for passive UHF RFID tag antennas. To the best of the author's knowledge, the integration of Huygens'-based meta-structures into passive UHF RFID tags has not been previously reported. A dipolar patch configuration was selected as the baseline platform due to its structural simplicity, geometrical symmetry, and predictable impedance characteristics, enabling a systematic evaluation of the electromagnetic effects introduced by HME integration.

The designed Huygens' unit cell demonstrates a wide operational bandwidth, with the −10 dB reflection coefficient spanning from 815 MHz to 952 MHz, thereby covering the targeted UHF RFID band. Within this range, the transmission phase response extends from −179.6° to 179.3°, providing nearly complete phase coverage for effective wavefront manipulation. Additionally, the transmission magnitude remains better than −0.09 dB at 868 MHz, indicating minimal insertion loss and high transmission efficiency.

When the HME array is positioned above the dipolar patch, constructive wavefront shaping is achieved, resulting in enhanced radiation focusing without increasing the radiator's physical dimensions. This Huygens' Meta-Element-assisted configuration improves the realized gain and radiation directivity, which consequently extends the read range performance. Importantly, the integration does not require active components or biasing networks, thereby preserving the fully passive nature of the

RFID system. Overall, the results validate that Huygens'-based electromagnetic wave manipulation provides a practical and compact solution to mitigate the inherent gain limitations of electrically small RFID tag antennas.

6.2 Overall Research Contributions

The research objectives outlined in Chapter 1 have been successfully achieved through comprehensive theoretical analysis, systematic antenna design, full-wave simulation, fabrication, and experimental validation. By critically reviewing previous studies and applying fundamental antenna principles, this research has established clear technical contributions to the development of compact and high-performance passive UHF RFID tag antennas for metallic environments.

In alignment with the proposed objectives, the main contributions of this PhD research are summarized as follows:

a) Miniaturized Folded Antenna Configuration

A compact folded stacked-patch UHF RFID tag antenna was developed to achieve electrical size reduction while maintaining efficient radiation performance. The folded configuration increases effective capacitance, enabling miniaturization without compromising operational stability when mounted on metal surfaces.

b) Structurally Integrated Tuning Mechanism

An embedded inclined slot structure was proposed and integrated into the radiating patch to function as an effective inductive element. This structurally integrated tuning mechanism enables precise control of the resonant frequency and input reactance, thereby facilitating stable impedance matching with highly capacitive RFID microchips, particularly under metallic mounting conditions.

c) Huygens' Meta-Element (HME) Integration for Radiation Enhancement

The impact of Huygens' Meta-Elements on the radiation characteristics of the on-metal RFID tag antenna was systematically analyzed. The integration of HME

demonstrated improved realized gain, enhanced radiation directivity, and extended read range performance without increasing the radiator dimensions.

d) Experimental Validation of Prototype Designs

The proposed RFID tag antennas were fabricated and experimentally characterized to validate simulation accuracy. Measurement results confirmed the reliability of the design methodology and verified the achieved performance improvements under practical operating conditions.

Overall, this research bridges the gap between compact metal-mountable RFID tag antenna design and advanced electromagnetic wave manipulation techniques, establishing a structured design framework for impedance-sensitive passive RFID systems operating in challenging metallic environments.

6.3 Recommendations for Future Work

Although the proposed antenna designs have demonstrated significant improvements in compactness, impedance stability, and radiation performance for metallic environments, several research extensions can be pursued to further enhance system capability and practical deployment.

a) Broadband And Multi-Band RFID Tag Antenna

The proposed Huygens' Meta-Element (HME) is optimized for operation within the targeted UHF RFID band. Future research may investigate broadband and multi-band meta-integrated RFID tag antennas capable of maintaining stable phase and amplitude control across the global UHF RFID spectrum (860–960 MHz) and emerging multi-band IoT applications. Advanced metasurface architectures, including multilayer configurations, stacked resonators, and parasitic elements, could be explored to improve bandwidth, frequency agility, and operational robustness under diverse deployment conditions.

b) Environmental Robustness and Dielectric Mounting Effects

Although laboratory measurements have validated the antenna performance under controlled conditions, long-term reliability in practical deployment environments remains an important consideration. Future work should therefore include comprehensive environmental stress evaluations, such as temperature cycling, humidity exposure, and UV aging tests, to assess durability and performance stability in industrial and outdoor applications. Furthermore, the influence of different mounting platforms should be systematically examined. In addition to metallic surfaces, the antenna performance can be evaluated when attached to dielectric backing materials such as plastics, rubber, and composite substrates. Investigating variations in material permittivity and loss characteristics would provide deeper insight into impedance stability, radiation behaviour, and read range consistency under diverse real-world deployment conditions.

c) Advanced Computational Design and Artificial Intelligence

While the antenna parameters were optimized through systematic parametric analysis, future research may incorporate artificial intelligence (AI)-assisted optimization techniques, including genetic algorithms (GA), particle swarm optimization (PSO), Bayesian optimization, and machine-learning-based surrogate models. These approaches can significantly accelerate the design process, explore larger design spaces, and identify globally optimal antenna configurations with improved impedance matching, gain, efficiency, and read range.

d) Flexible, Conformal, and Sustainable RFID Platforms

Future investigations may focus on ultra-low-profile and flexible tag antenna structures fabricated using flexible substrates, printable conductive inks, or additive manufacturing techniques. Such developments would enable conformal RFID tags for wearable electronics, curved metallic surfaces, aerospace structures, and smart infrastructure. In parallel, environmentally sustainable materials and low-cost manufacturing processes may be explored to facilitate large-scale deployment while reducing production costs and environmental impact.

e) Comprehensive Field Validation

Beyond laboratory validation, future work should include large-scale field trials under realistic industrial environments to evaluate long-term reliability, environmental robustness, and performance consistency under varying temperature, humidity, mechanical stress, and mounting materials.

6.4 Summary

In conclusion, this research establishes a structured and practical design framework for compact, metal-mountable passive UHF RFID tag antennas by integrating structural miniaturization techniques with advanced electromagnetic wave manipulation through Huygens' Meta-Elements. The findings contribute not only to RFID antenna engineering but also to the broader advancement of metastructure-assisted wireless system design.

REFERENCES

A. A. Sharatol Ahmad Shah, N. H. Abd Rahman, M. T. Ali, M. R. Ahmad, S. A. Nordin, N. I. Zaidi, N. H. Abdul Aziz, & Y. Yamada. (2018). Design of Electro-Textile UHF RFID Tag through T-Match Network. *IEEE International RF and Microwave Conference*.

Akram, M. R., He, C., & Zhu, W. (2020). Bi-layer metasurface based on Huygens' principle for high gain antenna applications. *Optics Express*, *28*(11), 15844. https://doi.org/10.1364/oe.393119

Alagiasundaram, S., Lee, K. Y., Lim, E. H., Chee, P. S., & Bong, F. L. (2023). Planar Inverted Antenna With Embedded Patch Excitor for On-Metal Tag Design. *IEEE Journal of Radio Frequency Identification*, *7*, 233–242. https://doi.org/10.1109/JRFID.2023.3286486

Ali, J., Kaemarungsi, K., & Chalermwisutkul, S. (2022). Post-Design Modifications for Impedance Matching of UHF RFID Tag Antenna. *2022 International Conference on Power, Energy and Innovations, ICPEI 2022*. https://doi.org/10.1109/ICPEI55293.2022.9987164

Ali, S., & Ghaffar, F. A. (2026). A Single Element Antenna With Continuous Beam Steering Capabilities Inspired by FPMS. *IEEE Journal of Microwaves*, *6*(4), 1007–1020. https://doi.org/10.1109/JMW.2026.3707763

Bansal, A., Sharma, S., & Khanna, R. (2019). A Spiral Shaped Loop Fed high Read Range Compact Tag Antenna for UHF RFID Applications. *IEEE International Conference on RFID Technology and Applications (RFID-TA)*.

Bansal, A., Sharma, S., & Khanna, R. (2022). RFID Tag Design with high read range Performance for Dual band Applications in UHF Range. *IEEE 12th International Conference on RFID Technology and Applications, RFID-TA 2022*, 82–85. https://doi.org/10.1109/RFID-TA54958.2022.9924081

Bhaskar, S., Barman, B., & Singh, A. K. (2019). Circularly Polarized Meander Line Cross Dipole Antenna for UHF RFID Applications. *URSI AP-RASC 2019*.

Bhaskar, S., & Singh, A. K. (2017). Capacitive Tip Loaded linearly tapered Meander Line Antenna for UHF RFID Tag Applications. *2017 IEEE Applied Electromagnetics Conference (AEMC)*.

Bhaskar, S., & Singh, A. K. (2021). A Compact Meander Line UHF RFID Antenna for Passive Tag Applications. *Progress In Electromagnetics Research*, *99*, 57–67.

Bong, F. L., Lim, E. H., & Lo, F. L. (2017). Miniaturized dipolar patch antenna with narrow meandered slotline for UHF tag. *IEEE Transactions on Antennas and Propagation*, *65*(9), 4435–4442. https://doi.org/10.1109/TAP.2017.2724074

Bong, F.-L., Lim, E.-H., & Lo, F.-L. (2018). Compact Orientation Insensitive Dipolar Patch for Metal-Mountable UHF RFID Tag Design. *IEEE TRANSACTIONS ON ANTENNAS AND PROPAGATION*, *66*(4), 1788–1795.

Calabrese, C., & Marrocco, G. (2008). Meandered-Slot Antennas for Sensor-RFID Tags. *IEEE ANTENNAS AND WIRELESS PROPAGATION LETTERS*, *7*, 15–18.

Casula, G. A., Lestini, F., Chietera, F. P., Muntoni, G., Occhiuzzi, C., Catarinucci, L., Colella, R., Montisci, G., & Marrocco, G. (2024). Design of On-Body Epidermal Antenna on AMC Substrate for UHF RFID in Healthcare. *IEEE Transactions on Antennas and Propagation*, *72*(5), 4023–4035. https://doi.org/10.1109/TAP.2024.3383214

Chen, H. D., Tsai, C. H., Sim, C. Y. D., & Kuo, C. Y. (2013). Circularly polarized loop tag antenna for long reading range RFID applications. *IEEE Antennas and Wireless Propagation Letters*, *12*, 1460–1463. https://doi.org/10.1109/LAWP.2013.2288138

Choudhary, A., Sood, D., & Tripathi, C. C. (2018). Wideband long range, radiation efficient compact UHF RFID Tag. *IEEE Antennas and Wireless Propagation Letters*, *17*(10), 1755–1759. https://doi.org/10.1109/LAWP.2018.2844249

Costa, F., Genovesi, S., Borgese, M., Michel, A., Dicandia, F. A., & Manara, G. (2021). A review of rfid sensors, the new frontier of internet of things. *Sensors*, *21*(9). https://doi.org/10.3390/s21093138

Cui, L., Zhang, Z., Gao, N., Meng, Z., & Li, Z. (2019). Radio frequency identification and sensing techniques and their applications—A review of the state-of-the-art. In *Sensors (Switzerland)* (Vol. 19, Number 18). MDPI AG. https://doi.org/10.3390/s19184012

Eleftheriades, G. V., Kim, M., Ataloglou, V. G., & Dorrah, A. H. (2022). Prospects of Huygens' Metasurfaces for Antenna Applications. *Engineering*, *11*, 21–26. https://doi.org/10.1016/j.eng.2021.05.011

Erman, F., Hanafi, E., Lim, E. H., Mahyiddin, W. A. W. M., Harun, S. W., Umair, H., & Soboh, R. (2020). U-Shaped Inductively Coupled Feed UHF RFID Tag Antenna with DMS for Metal Objects. *IEEE Antennas and Wireless Propagation Letters*, *19*(6), 907–911. https://doi.org/10.1109/LAWP.2020.2981960

Erman, F., & Koziel, S. (2022). Miniaturized Metal-Mountable U-Shaped Inductive-Coupling-Fed UHF RFID Tag Antenna With Defected. *IEEE Access*, *10*, 47301–47308. https://doi.org/10.1109/ACCESS.2022.3171243

Erman, F., Koziel, S., Lim, E. H., Alkaraki, S., Murugesh, M., Soboh, R., & Kouali, M. (2026). Low-Profile Double-Sided Metal-Backed H-Slot Folded-Patch Tag With Resonance Tuning Capability for On-Metal UHF RFID. *IEEE Access*, *14*, 43869–43878. https://doi.org/10.1109/ACCESS.2026.3670961

Farnana, T. D., Hassan, I. H., Hamidon, M. N., Sali, A., & Isa, M. M. (2024). Passive RFID Tag Antenna on Kapton Substrate for IoT Applications. *Proceedings of the 8th International Symposium on Advanced Materials and Nanotechnology 2024, (ISAMN2024)*.

Faudzi, N. M., Rashid, A. N. A., Ibrahim, A., Khyasudeen, M. F., & Ali, M. T. (2016). Microstrip Dipole UHF-RFID Tag Antenna for Metal Object Tagging. *Proceedings - 6th International Conference on Computer and Communication Engineering: Innovative Technologies to Serve Humanity, ICCCE 2016*, 36–41. https://doi.org/10.1109/ICCCE.2016.21

Hien Doan, T. N., Ta, S. X., Van Nguyen, K., Nguyen, K. K., & Dao-Ngoc, C. (2019). Low-Profile, Dual-Band, Unidirectional RFID Tag Antenna Using Metasurface. *Progress In Electromagnetics Research C*, *93*(April), 131–141. https://doi.org/10.2528/PIERC19041505

Hussain, M., Amin, Y., & Lee, K. G. (2020). A compact and flexible UHF RFID tag antenna for massive IoT devices in 5G system. *Sensors (Switzerland)*, *20*(19), 1–21. https://doi.org/10.3390/s20195713

Inserra, D., Wang, Y., Peng, F., Li, Z., & Wen, G. (2026). Metal Mountable UHF RFID Tag Design Requiring Screw Fixing. *IEEE Journal of Radio Frequency Identification*, *10*, 113–121. https://doi.org/10.1109/JRFID.2026.3655933

Islam, M. T., Alam, T., Yahya, I., & Cho, M. (2018). Flexible radio-frequency identification (RFID) tag antenna for sensor applications. *Sensors (Switzerland)*, *18*(12). https://doi.org/10.3390/s18124212

Jialong, W. (2023). A review of RFID Tag based on TFT. *Applied and Computational Engineering*, *25*(1), 292–296. https://doi.org/10.54254/2755-2721/25/20230781

Khan, H., Nasir, A., Bin Mumtaz, U., Ullah, S., Ali Shah, S. A., Fawad Khan, M., & Ali, U. (2016). Design and Analysis of a Wearable Monopole Antenna on Jeans Substrate for RFID Applications. *International Journal of Wireless and Microwave Technologies*, *6*(6), 24–35. https://doi.org/10.5815/ijwmt.2016.06.03

Kim, D., Yeo, J., & Abstract, A. (2009). Low-Profile RFID Tag Antenna Using Compact AMC Substrate for Metallic Objects. *IEEE ANTENNAS AND WIRELESS PROPAGATION LETTERS*, *7*, 718–720.

Korfiati, T., Vazouras, C. N., Bolakis, C., Stavrinidis, A., Stavrinidis, G., & Arapogianni, A. (2024). Design, Fabrication and Testing of a Multifrequency Microstrip RFID Tag Antenna on Si. *Computation*, *12*(6). https://doi.org/10.3390/computation12060122

Lee, S., Lim, E., Bong, F., & Chung, B. (2020). High-Efficient Compact Folded-Patch Antenna Fed UHF RFID Tag Design. *IEEE Transactions on Antennas and Propagation*, *68*(1), 152–160. https://doi.org/10.1109/TAP.2019.2938794

Lee, S. R., Lim, E. H., & Rahim, S. K. A. (2022a). Small Wideband Antenna for On-Metal UHF RFID Tag Design. *IEEE Journal of Radio Frequency Identification*, *6*, 121–127. https://doi.org/10.1109/JRFID.2021.3134492

Lee, S. R., Lim, E. H., & Rahim, S. K. A. (2022b). Small Wideband Antenna for On-Metal UHF RFID Tag Design. *IEEE Journal of Radio Frequency Identification*, *6*, 121–127. https://doi.org/10.1109/JRFID.2021.3134492

Lee, Y. H., Moh, C. W., Lim, E. H., Bong, F. L., & Chung, B. K. (2020). Miniature Folded Patch with Differential Coplanar Feedline for Metal Mountable UHF RFID Tag. *IEEE Journal of Radio Frequency Identification*, *4*(2), 93–100. https://doi.org/10.1109/JRFID.2019.2957011

Lin, Y., Xu, Y., Chen, S., & Ma, L. (2019). *Design of a Meander Line Dipole RFID Tag Antenna for Temperature Sensor*.

Liu, Q., Zhong, S., Yu, Y., Zhao, W. S., & Wang, G. (2022). Platform-Tolerant Nested-Slot RFID Tag Antenna Based on Jigsaw-Shaped Metasurface. *IEEE Antennas and Wireless Propagation Letters*, *21*(5), 943–947. https://doi.org/10.1109/LAWP.2022.3152621

Liu, Y., Quan, L., Duan, F., Li, B., & Xie, K. (2026). A Low-Profile and Broadband Circularly Polarized Folded Transmitarray Antenna Using Metasurfaces. *IEEE Antennas and Wireless Propagation Letters*, 1–5. https://doi.org/10.1109/LAWP.2026.3716693

Lo, C. C., & Chen, Y. S. (2025). Miniature Dual-Band Tag Antennas via Stacked Integration of a Folded Dipole and Dual-Patch for Antimetal RFID. *IEEE Antennas and Wireless Propagation Letters*, *24*(8), 2652–2656. https://doi.org/10.1109/LAWP.2025.3570778

López-Soriano, S., & Parrón, J. (2015). Small Size and Low Cost UHF RFID Tag Antenna Mountable on Metallic Objects. *International Journal of Antennas and Propagation*, *2015*. https://doi.org/10.1155/2015/870478

Lubna, L., Hameed, H., Ansari, S., Zahid, A., Sharif, A., Abbas, H. T., Alqahtani, F., Mufti, N., Ullah, S., Imran, M. A., & Abbasi, Q. H. (2022). Radio frequency sensing and its innovative applications in diverse sectors: A comprehensive study. In *Frontiers in Communications and Networks* (Vol. 3). Frontiers Media SA. https://doi.org/10.3389/frcmn.2022.1010228

Luo, W., & Wang, P. (2023). A Compact UHF-RFID Tag Antenna With Embedded AMC for Metallic Objects. *IEEE Antennas and Wireless Propagation Letters*, *22*(4), 873–877. https://doi.org/10.1109/LAWP.2022.3227232

Ma, S., Ukkonen, L., Sydanheimo, L., & Bjorninen, T. (2020). Inductively Coupled Split Ring Resonator as Small RFID Pressure Sensor for Biomedical Applications. *2020 IEEE International Symposium on Antennas and Propagation and North*

American Radio Science Meeting, IEEECONF 2020 - Proceedings, 1655–1656. https://doi.org/10.1109/IEEECONF35879.2020.9329731

MCMC. (2020). *Short Range Devices - Specifications*. (May).

Miswadi, N. F., Abd Rahman, N. H., Subahir, S., Aris, M. A., Awang, R. A., & Lim, E. H. (2022). Design of a Flexible T-Matched Feed UHF RFID Tag Antenna. *Journal of Physics: Conference Series*, *2250*(1). https://doi.org/10.1088/1742-6596/2250/1/012015

Miswadi, N., Rahman, N. H. A., Lim, E. H., Subahir, S. B., Aris, M. A., & Murugesh, M. (2024). Embedded Inductance Folded-Patch Antenna with Inclined Slots for On-Metal Tag Design. *IEEE Journal of Radio Frequency Identification*, *8*, 685–694. https://doi.org/10.1109/JRFID.2024.3431198

Miswadi, NF., Abd Rahman, N., Subahir, S., Aris, M. A., Awang, R., & Lim, E. H. (2022). Design of a Flexible T-Matched Feed UHF RFID Tag Antenna. *Journal of Physics: Conference Series*, *2250*(1), 012015. https://doi.org/10.1088/1742-6596/2250/1/012015

Mo, L., & Li, C. (2019). Double loop inductive feed patch antenna design for antimetal UHF RFID tag. *International Journal of Antennas and Propagation*, *2019*. https://doi.org/10.1155/2019/2917619

Murugesh, M., & Akbar, M. F. (2025). Frequency Tunable Folded-Patch UHF RFID Tag Antenna for Metal Surfaces. *IEEE Journal of Radio Frequency Identification*, *9*, 976–987. https://doi.org/10.1109/JRFID.2025.3641924

Murugesh, M., Akbar, M. F., & Ghazali, N. A. (2026). Miniature anti-metal UHF RFID tag antenna loaded with embedded open stubs for enhanced bandwidth. *Scientific Reports*, *16*(1). https://doi.org/10.1038/s41598-026-51170-1

Murugesh, M., Akbar, M. F., Ghazali, N. A., & Alagiasundaram, S. (2026). A Compact On-Metal UHF RFID Tag Antenna Incorporating Multiple T-Shaped Tuning Slots. *IEEE Access*. https://doi.org/10.1109/ACCESS.2026.3710176

Murugesh, M., Lee, Y. H., Chee, P. S., & Lim, E. H. (2020). Flexible Folded-Patch Antenna with Tapered Edges for Metal-Mountable UHF RFID Tag Design. *2020 IEEE International RF and Microwave Conference, RFM 2020 - Proceeding*, 16–18. https://doi.org/10.1109/RFM50841.2020.9344760

Murugesh, M., Lim, E. H., Chee, P. S., & Bong, F. L. (2022). Complementarily Coupled C-Shaped Microstrip Patches With Wide-Range Frequency Tuning Capability for Metal-Applicable UHF RFID Tag Design. *IEEE Transactions on Antennas and Propagation*, *70*(12), 11548–11558. https://doi.org/10.1109/TAP.2022.3209733

Muthukannan Murugesh, Eng-Hock Lim, Pei-Song Chee, & Fwee-Leong Bong. (2023). On-Metal UHF Tag Antenna Design using Concentric Step-Impedance Rings. *IEEE Journal of Radio Frequency Identification*, *7*, 621–629.

Ng, G. J., Lim, E. H., Chee, P. S., & Murugesh, M. (2025). Design of Dual-Band UHF RFID Tag Antenna Using Even and Odd Modes of Asymmetric Split Ring for Anti-Metal Applications. *IEEE Transactions on Antennas and Propagation*, *73*(1), 64–73. https://doi.org/10.1109/TAP.2024.3495220

Nguyen, M. T., Chen, H. M., Pham, D. S., Chen, C. H., & Lin, Y. F. (2023). Low Profile Planar Inverted-L Antenna (PILA) for UHF RFID on Metal-Tag. *Asia-Pacific Microwave Conference Proceedings, APMC*, 476–478. https://doi.org/10.1109/APMC57107.2023.10439843

N.M.Faudzi, M. T. A. I. I. H. J. N. H. M. S. (2014). Metal Mountable UHF-RFID Tag Antenna with Meander Feed Line and Double T-Match. *International Symposium on Technology Management and Emerging Technologies (ISTMET 2014)*.

NXP Semiconductors. (2021). *SL3S1205, UCODE 8/8m*. 38. https://www.nxp.com/docs/en/data-sheet/SL3S1205-15-DS.pdf

NXP Semiconductors. (2025). *SL3S1206, UCODE 9*.

Ooi, S. Y., Chee, P. S., Lim, E. H., Lee, Y. H., & Bong, F. L. (2022). Stacked Planar Inverted-L Antenna with Enhanced Capacitance for Compact Tag Design. *IEEE Transactions on Antennas and Propagation*, *70*(3), 1816–1823. https://doi.org/10.1109/TAP.2021.3118822

Ooi, S. Y., Chee, P. S., Lim, E. H., Low, J. H., & Bong, F. L. (2023). A Zeroth-Order Slot-Loaded Cap-Shaped Patch Antenna with Omnidirectional Radiation Characteristic for UHF RFID Tag Design. *IEEE Transactions on Antennas and Propagation*, *71*(1), 131–139. https://doi.org/10.1109/TAP.2022.3221032

P. Wongsiritorn, Phongcharoenpanich, C., Torrungrueng, D., & Krairiksh, M. (2009). Meander-Line UHF RFID Tag Antenna with Semi-Circular Structure. *International Symposium on Antennas and Propagation (ISAP 2009)*.

Paramasivam, D., Dewan, R., You Kok Yeow, & Faishal Adilah Suryanata. (2024). A Review on Strategies to Enhance the On-Body Read Range of Passive UHF RFID Tag. *ELEKTRIKA- Journal of Electrical Engineering*, *23*(3), 101–107. https://doi.org/10.11113/elektrika.v23n3.605

Peng, Q., Akram, M. R., Rukhlenko, I. D., & Zhu, W. (2020). Highly transmissive bilayer Huygens' metasurface with over 315° phase coverage. *AEU - International Journal of Electronics and Communications*, *124*, 153330. https://doi.org/10.1016/j.aeue.2020.153330

Pourgholamhossein, Z., Jazi, M. N., & Denidni, T. A. (2022). Broadband Flat-Lens Antenna Design Using Ultrathin Huygens Metasurface for Millimeter-Wave Applications. *IEEE Transactions on Antennas and Propagation*, *PP*(1), 1. https://doi.org/10.1109/TAP.2022.3184515

Radiocommunication Sector of ITU. (2012). *Technical characteristics, standards, and frequency bands of operation for radio-frequency identification (RFID) and potential harmonization opportunities* (Vol. 0). https://www.itu.int/dms_pub/itu-r/opb/rep/R-REP-SM.2255-2012-PDF-E.pdf

Räsänen, M., Holopainen, J., Bergman, J., Kuosmanen, M., & Viikari, V. (2024). Small On-Metal Passive UHF RFID Transponders With Long Read Ranges. *18th European Conference on Antennas and Propagation, EuCAP 2024*, 1–4. https://doi.org/10.23919/EuCAP60739.2024.10501750

Ripin, N., Lim, E. H., Bong, F. L., & Chung, B. K. (2020). Miniature Folded Dipolar Patch with Embedded AMC for Metal Mountable Tag Design. *IEEE Transactions on Antennas and Propagation*, *68*(5), 3525–3533. https://doi.org/10.1109/TAP.2020.2969814

Rizkalla, S., Prestros, R., & Mecklenbräuker, C. F. (2018). Metallic inductive coupling frame-based HF RFID cards. *IET Microwaves, Antennas and Propagation*, *12*(5), 692–698. https://doi.org/10.1049/iet-map.2017.0573

Sakurai, S., Rahmeier, J. G. N., Tomura, T., Hirokawa, J., & Gupta, S. (2021). Millimeter-Wave Huygens' Transmit Arrays Based on Coupled Metallic Resonators. *IEEE Transactions on Antennas and Propagation*, *69*(5), 2686–2696. https://doi.org/10.1109/TAP.2020.3030972

Salman, K. N., Ismail, A., Abdullah, R. S. A. R., & Saeedi, T. (2017). Coplanar UHF RFID tag antenna with Ushaped inductively coupled feed for metallic applications. *PLoS ONE*, *12*(6). https://doi.org/10.1371/journal.pone.0178388

Sarkar, S., & Gupta, B. (2025). A Triple-Band Slotted Patch Antenna With Metasurface Loading for UHF-RFID, Satellite Communication, and 5G Applications. *IEEE Access*, *13*, 80–89. https://doi.org/10.1109/ACCESS.2024.3522916

Shreya U. Naik, Steffie Tom, & Dr. H. G. Virani. (2020). Design of a Tag Dipole Antenna for the RFID Applications. *Proceedings of the International Conference on Electronics and Sustainable Communication Systems (ICESC 2020)*.

Solanki, R., Lee, C. W. L., Tan, P. K., & Gan, T. H. (2026). Comprehensive Analysis of Highly Efficient, High Gain, Modular and Scalable, Dual-Linear-Polarized Metalens Antenna for SatCom Applications. *IEEE Journal on Miniaturization for Air and Space Systems*, 1–1. https://doi.org/10.1109/JMASS.2026.3715681

Su, D., Zhang, H., Xiao, H., Song, W., Xiong, H., Xiao, D., & Wang, X. (2023). Construction of 3-D Microwave Helical Beams Using Huygens' Metasurface. *IEEE Transactions on Antennas and Propagation*, *71*(11), 8907–8916. https://doi.org/10.1109/TAP.2023.3306459

Sun, H., Tao, B., & Ramahi, O. M. (2017). Offset-Fed Folded Dipole and Its Application As RFID Tag Antenna. *IEEE JOURNAL OF RADIO FREQUENCY IDENTIFICATION*, *1*(2), 109–114.

Tan, N. M., Chen, H. M., Sim, C. Y. D., & Chen, C. H. (2020). An Inverted-F Antenna for RFID Tag Mounted on a Full Container of Liquid. *2020 IEEE International Symposium on Antennas and Propagation and North American Radio Science Meeting, IEEECONF 2020 - Proceedings*, 1523–1524. https://doi.org/10.1109/IEEECONF35879.2020.9330496

Thirappa, K., Member, S., Lim, E., & Member, S. (2019). Compact Folded-Patch With Orthogonal Tuning Slots for On-Metal Tag Design. *IEEE Transactions on Antennas and Propagation*, *67*(9), 5833–5842. https://doi.org/10.1109/TAP.2019.2920324

Toaha, A., Islam, M. T., & Misr, N. (2011). RFID Technology: Perspectives and Technical Considerations of Microstrip Antennas for Multi-Band RFID Reader Operation. *Current Trends and Challenges in RFID*, (May 2014). https://doi.org/10.5772/16913

Turitsyna, E. G., & Webb, S. (2005). Design of RFID tag antennas using an inductively coupled feed. *Electronics Letters*, *41*(2), 40–41. https://doi.org/10.1049/el

Vellucci, S., Monti, A., Barbuto, M., Wakatsuchi, H., Toscano, A., & Bilotti, F. (2026). Pulse-Driven Reconfigurable Transmissive Huygens' Metasurface for Beam-Steering. *IEEE Journal of Selected Topics in Electromagnetics, Antennas and Propagation*, *2*, 362–371. https://doi.org/10.1109/JSTEAP.2026.3714389

Warren L. Stutzman, G. A. T. (2012). *Antenna Theory and Design* (THIRD). John Wiley & Sons.

Wickramasinghe, S., Jayasinghe, J., & Senadeera, M. (2021). Design of a Passive RFID Tag Antenna with a Modified T-match Structure. *IEEE 16th International Conference on Industrial and Information Systems, ICIIS 2021*, 46–51. https://doi.org/10.1109/ICIIS53135.2021.9660727

Wyld, D. C. (2010). 24-KARAT PROTECTION: RFID AND RETAIL JEWELRY MARKETING. In *International Journal of UbiComp (IJU)* (Vol. 1, Number 1). http://www.jcssoft.com/

Xue, C., Lou, Q., & Chen, Z. N. (2020). Broadband Double-Layered Huygens' Metasurface Lens Antenna for 5G Millimeter-Wave Systems. *IEEE Transactions on Antennas and Propagation*, *68*(3), 1468–1476. https://doi.org/10.1109/TAP.2019.2943440

Xue, C., Sun, J., Gao, X., Chen, F., Pang, Z., Lou, Q., & Chen, Z. N. (2022). An Ultrathin, Low-Profile and High-Efficiency Metalens Antenna Based on Chain

Huygens' Metasurface. *IEEE Transactions on Antennas and Propagation*, *70*(12), 11442–11453. https://doi.org/10.1109/TAP.2022.3209283

Zhang, Y. J., Wang, D., & Tong, M. S. (2017). An Adjustable Quarter-Wavelength Meandered Dipole Antenna With Slotted Ground for Metallically and Airily Mounted RFID Tag. *IEEE Transactions on Antennas and Propagation*, *65*(6), 2890–2898. https://doi.org/10.1109/TAP.2017.2690535

Zhao, L., Ma, Y., Meng, W., Peng, K., & Liu, K. (2023). Bendable Folded-Patch Antenna With Resonant Ring Manufactured Based on Foam Support and PET Substrate for On-Metal UHF RFID. *IEEE Journal of Radio Frequency Identification*, *7*, 591–600. https://doi.org/10.1109/JRFID.2023.3327939

Zohre Pourgholamhossein, T. A. D. (2017). Experimental_Characterization_of_a_New_Active_Huygens_Metasurface-based_Element_for_Beam_Steerable_Lens_at_Ka-Band. *IEEE ACCESS*.

APPENDICES

APPENDIX 1

NXP Semiconductors UCODE 8/8m Datasheet

11 Characteristics

11.1 UCODE 8/8m bare die characteristics

Table 15. UCODE 8/8m RF interface characteristics (RF1, RF2)

Symbol	Parameter	Conditions		Min	Typ	Max	Unit
f_i	input frequency			840	-	960	MHz
$P_{i(min)}$	minimum input power	READ sensitivity	[1] [2] [3]	-	- 22.9	-	dBm
		reduced operating range	[4]	-	+ 1	-	dBm
$P_{i(min)}$	minimum input power	WRITE sensitivity	[4]	-	-17.8	-	dBm
t 16bit	encoding speed	16-bit	[5]	-	0.7	-	ms
		32-bit (block write)	[5]	-	1.2	-	ms
C_i	chip input capacitance, Large Pads	parallel	[2] [6] [7]	-	0.69	-	pF
Z	chip impedance, Large Pads	866 MHz	[2] [6] [7]	-	15-j265	-	Ω
		915 MHz	[2] [6] [7]	-	14-j252	-	Ω
		953 MHz	[2] [6] [7]	-	13-j242	-	Ω
Z	typical assembled impedance, Large Pads (see Figure 8)	915 MHz	[8] [9] [7]	-	19-j234		Ω
Z	typical assembled impedance in case of single-slit antenna assembly, Large Pads (see Figure 9)	915 MHz	[8] [10] [7]		13-j191	-	Ω

[1] Power to process a QUERY command
[2] Measured with a 50 Ω source impedance directly on the chip
[3] Results in approximately -23 dBm tag sensitivity with a 2.15 dBi gain antenna
[4] Tag sensitivity on a 2.15 dBi gain antenna
[5] When the memory content is "0000...".
[6] At minimum operating power
[7] at center capacitor of Self Adjust
[8] The antenna shall be matched to this impedance
[9] Assuming 50fF additional assembly capacitance
[10] Assuming 220fF additional assembly+test pad capacitance

Table 16. UCODE 8/8m memory characteristics

Symbol	Parameter	Conditions		Min	Typ	Max	Unit
EEPROM characteristics							
t_{ret}	retention time	$T_{amb} \leq 55$ °C		20	-	-	year
$N_{endu(W)}$	write endurance			100k	-	-	cycle

All information provided in this document is subject to legal disclaimers.

© NXP B.V. 2021. All rights reserved.

APPENDIX 2

NXP Semiconductors UCODE 9 Datasheet

11 Characteristics

11.1 UCODE 9 bare die characteristics

Table 11. UCODE 9 RF interface characteristics (RF1, RF2)

Symbol	Parameter	Conditions		Min	Typ	Max	Unit
f_i	input frequency			840	-	960	MHz
$P_{i(min)}$	minimum input power	READ sensitivity	[1]	-	- 24	-	dBm
$P_{i(min)}$	minimum input power	WRITE sensitivity	[1]	-	-22	-	dBm
t	encoding speed	16-bit	[2]	-	0.6	-	ms
		32-bit (block write)	[2]	-	1	-	ms
C_i	chip input capacitance	parallel, blade diced	[3] [4] [5]	-	0.715	-	pF
C_i	chip input capacitance	parallel, plasma diced	[3] [4] [5]	-	0.700	-	pF
R_P	chip resistance	parallel	[4]	-	3.6	-	kΩ
Z	chip impedance	915 MHz, blade diced	[3] [4] [5]	-	9-j243	-	Ω
Z	chip impedance	915 MHz, plasma diced	[3] [4] [5]	-	10-j248	-	Ω
Z	typical assembled impedance[6]	915 MHz, blade diced	[7] [8] [9]	-	15-j231	-	Ω
Z	typical assembled impedance[6]	915 MHz, plasma diced	[7] [8] [9]	-	16-j237	-	Ω
Z	typical assembled impedance in case of single-slit antenna assembly[10]	915 MHz	[7] [11] [9]	-	10-j191	-	Ω

[1] Tag sensitivity on a 2.15 dBi gain antenna
[2] When the memory content is "0000...".
[3] Measured with a 50 Ω source impedance directly on the chip
[4] At minimum operating power
[5] at center capacitor of Self-Adjust
[6] see Figure 7
[7] The antenna shall be matched to this impedance
[8] Assuming 35 fF additional assembly capacitance
[9] At center capacitor of Self-Adjust
[10] see Figure 8
[11] Assuming 195 fF (Blade)/210fF (Plasma) additional assembly+test pad capacitance

Table 12. UCODE 9 memory characteristics

Symbol	Parameter	Conditions		Min	Typ	Max	Unit
EEPROM characteristics							
t_{ret}	retention time	$T_{amb} \leq 55$ °C		20	-	-	year
		$T_{amb} \leq 85$ °C		10	-	-	year
		$T_{amb} \leq 125$ °C		1	-	-	year
$N_{endu(W)}$	write endurance			100k	-	-	cycle

All information provided in this document is subject to legal disclaimers.

© 2025 NXP B.V. All rights reserved.

AUTHOR'S PROFILE



Nurfarahin binti Miswadi was born in Johor, Malaysia. She obtained her Bachelor of Engineering (Hons.) in Electronics (Communication) from Universiti Teknologi MARA (UiTM) in 2013. In 2019, she received her Master of Science in Electrical Engineering from the same university. She successfully completed her master's degree with a thesis entitled "Design of Compact Reconfigurable Microstrip UWB Filtenna Structure with WiMAX and WLAN Band Rejection." She is currently pursuing her Doctor of Philosophy (PhD) in Electrical Engineering at the Faculty of Electrical Engineering, Universiti Teknologi MARA (UiTM), Shah Alam, Selangor. Her research interests include UHF RFID tag antennas, reconfigurable antennas, low-profile antennas, ultra-wideband (UWB) antennas, and multifunctional antenna systems.

LIST OF PUBLICATIONS

Miswadi, N., Rahman, N. H. A., Lim, E. H., Subahir, S. B., Aris, M. A., & Murugesh, M. (2024). Embedded Inductance Folded-Patch Antenna with Inclined Slots for On-Metal Tag Design. *IEEE Journal of Radio Frequency Identification*, *8*, 685–694. https://doi.org/10.1109/JRFID.2024.3431198

Miswadi, N., Rahman, N. H. A., Subahir, S., Lim, E. H., Redzwan, F. N. M., & Ja'afar, H. (2024). A Low Profile and High Read Range Slotted Antenna for Dual-Band Anti-Metal UHF RFID Tag Antenna. *IEEE Asia-Pacific Conference on Applied Electromagnetics, APACE 2024*, 239–241. https://doi.org/10.1109/APACE62360.2024.10877401

Miswadi, N., Rahman, N. H. A., Subahir, S., Lim, E. H., Aris, M. A., & Mun, C. K. (2022). Flexible Low-Profile On-Metal Tag Antenna for Asset Tracking and Identification. *2022 International Symposium on Antennas and Propagation, ISAP 2022*, 399–400. https://doi.org/10.1109/ISAP53582.2022.9998868

Miswadi, NF., Abd Rahman, N., Subahir, S., Aris, M. A., Awang, R., & Lim, E. H. (2022). Design of a Flexible T-Matched Feed UHF RFID Tag Antenna. *Journal of Physics: Conference Series*, *2250*(1), 012015. https://doi.org/10.1088/1742-6596/2250/1/012015